UNIVERSITY OF OKLAHOMA

GRADUATE COLLEGE

SUPPRESSION OF ALIASING ARTIFACTS ON 3D LAND DATA VIA CONSTRAINED LEAST-SQUARES MIGRATION

A THESIS

SUBMITTED TO THE GRADUATE FACULTY

in partial fulfillment of the requirements for the

Degree of

MASTER OF SCIENCE

By

ALEJANDRO CABRALES VARGAS
Norman, Oklahoma
2011

SUPPRESSION OF ALIASING ARTIFACTS ON 3D LAND DATA VIA CONSTRAINED LEAST-SQUARES MIGRATION

A THESIS APPROVED FOR THE
CONOCO PHILLIPS SCHOOL OF GEOLOGY AND GEOPHYSICS

BY

Dr. Kurt J. Marfurt, Chair

Dr. G. Randy Keller

Dr. John T. Kwiatkowski

ACKNOWLEDGEMENTS

I would like to thank Dr. Kurt Marfurt for the support during this project, and mainly for having helped me to stretch my technical capabilities to the limit, encouraging me to challenge myself in the difficult task accomplished in this thesis. It has been my pleasure and honor to have worked with him.

Thanks to Dr. Randy Keller and Dr. John T. Kwiatkowski for having accepted to play the role of "Executioners" (I mean, Committee Members) in this humble work.

Especial thanks to Tim (one of the most brilliant minds I have ever known!), for the important advices in programming and geophysics.

Thanks to all of you, my friends, who helped me since I came alone the first time. I would not like to forget mentioning anyone, so no names here, you know who you are!

Very special thanks to my Mexican "fanclub" in Oklahoma, to the "Olympia Academy", for the unforgettable moments of joy and life reflection.

Thanks to Petróleos Mexicanos for the economical support in my studies and for the privilege of being chosen to study abroad.

Special thanks to uncle Sergio (Chávez), who prepared me to take the difficult road of the petroleum industry, and oriented me in the difficult decision of choosing university and advisor.

And finally but extraordinarily important, a thousand thanks to the loves of my life, Paty, Zaira, and our families, to whom I dedicate this effort.

TABLE OF CONTENTS

LIST OF FIGURES

migration domain. Although this example shows the behavior using ten iterations, a more efficient algorithm would stop iterating after the change in |**δd**| falls below a threshold (the convergence slows down). In contrast, the residue and the gradient tend to converge faster because the constraint function constitutes a preconditioning factor.

Figure B14. Representative common shot gathers from the decimated two layer model corresponding to Figure B2.

Figure B15. Predicted (modeled) common shot gathers, **d**, from the conventionally migrated vector, **m**. Note that data gaps in **d** persist.

Figure B16. Predicted (modeled) common shot gathers, **d**, from the unconstrained LSM migrated vector, **m**. Note that data gaps in **d** persist.

Figure B17. Predicted (modeled) common shot gathers, **d**, from the constrained LSM migrated vector, **m**. Note that most gaps in **d** are now healed.

Figure B18.- Common offset gather, **m**, at h = 150 m computed from the decimated dataset for the two-layer model using conventional migration. Compare to Figure B6.

Figure B19. Common offset section gather, m, at h = 150 m computed from the decimated dataset for the two-layer model using unconstrained LSM. Compare to Figure B7.

Figure B20. Common offset gather, **m**, at h = 150 m computer from the decimated dataset for the two-layer model using constrained LSM. Note that most of the holes in the image have been properly predicted and that the migration smiles are attenuated compared to Figure B19. Compare to Figure B8.

Figure B21. Common reflection point gathers, **m**, at x = 3750 m computed from the decimated dataset using (a) Conventional migration, (b) Unconstrained LSM, and (c) Constrained LSM .

Figure B22. Stacked image of **m** over all offsets for the two-layer model computed from the decimated dataset using conventional migration.

Figure B23. Stacked image of **m** over all offsets for the two-layer model computed from the decimated dataset using unconstrained LSM.

Figure B24. Staked image of **m** over all offsets for the two-layer model computed from the decimated dataset using constrained LSM.

Figure B25. Behavior of the residual, the gradient, the model difference and the data difference with unconstrained and constrained LSM computed from the decimated dataset of the two-layer model. As with the undecimated (full) dataset, the unconstrained migration more closely fits the surface data, $\mathbf{d_0}$, as evidenced by the smaller value of |**δd**|. To do so, the unconstrained model makes use of aliases in the migration domain. In contrast, the residue and the gradient tend to converge faster because the constraint function constitutes a preconditioning factor.

Figure C1. Marmousi velocity depth model.

Figure C2. Representative shot gathers, $\mathbf{d_0}$, generated for the Marmousi model.

Figure D10. Stacked image of $\mathbf{m}$ over all offsets for the Hess salt model using conventional migration.

Figure D11. Stacked image of $\mathbf{m}$ over all offsets for the Hess salt model using unconstrained LSM. Note the attenuation of multiples inside the salt body and some background noise.

Figure D12. Stacked image of $\mathbf{m}$ over all offsets for the Hess salt model using constrained LSM. Note the low to medium background noise introduced by spurious flat events in the common reflection point gathers (Figure D9c).

Figure D13. Behavior of the residual, the gradient, the model difference and the data difference with unconstrained and constrained LSM for the Hess salt model. Note that the residual and the gradient converge just slightly faster in this case using constrained LSM. It is interesting to observe that the behavior of the gradient and the model difference of first block departs from the main trend of the other blocks, perhaps because it still includes traces of the numerical problem that prevented the convergence of the near offset. Data difference just slightly reduces after the major change from the zero iteration (not plotted) and the first iteration.

Figure D14. Representative common shot gathers from the decimated Hess salt model corresponding to Figure D2.

Figure D15. Predicted (modeled) common shot gathers, $\mathbf{d}$, from the conventionally migrated vector, $\mathbf{m}$. Note the anomalous reflector indicated by the black arrow, as in the undecimated case.

Figure D16. Hess VTI dataset, decimated: Predicted data after unconstrained LSM. The anomalous reflector was attenuated and the frequencies redistributed, but the gaps persist.

Figure D17. Hess VTI dataset, decimated: Predicted data after constrained LSM. The gaps have been almost completely filled. Note the artifacts created by the border effects of the constraint function in the blocks of traces.

Figure D18. Common offset gather, $\mathbf{m}$, at $h = 4000$ ft computed from the decimated dataset for the Hess salt model using conventional migration. Compare to Figure D6.

Figure D19. Common offset gather, $\mathbf{m}$, at $h = 4000$ ft computed from the decimated dataset for the Hess salt model using unconstrained LSM. Compare to Figure D7.

Figure D20. Common offset gather, $\mathbf{m}$, at $h = 4000$ ft computed from the decimated dataset for the Hess salt model using unconstrained LSM. Compare to Figure D8. Note how the target zone reflectors can be interpreted even better than in the full stack sections because of the higher frequency content, normally lost during the stacking process.

Figure D21. Common reflection point gathers, $\mathbf{m}$, at $x = 30000$ ft computed from the decimated dataset using (a) Conventional migration, (b) Unconstrained LSM, and (c) Constrained LSM.

Figure D22. Stacked image of $\mathbf{m}$ over all offsets for the Hess salt model computed from the decimated dataset using conventional migration.

Figure D23. Stacked image of $\mathbf{m}$ over all offsets for the Hess salt model computed from the decimated dataset using unconstrained LSM.

ABSTRACT

Kirchhoff migration has the ability to handle irregularly acquired seismic data without previous trace interpolation, in contrast with wave-equation continuation and finite-difference migration. However, aliased noise such as acquisition footprint frequently affects the migrated gathers making difficult or even impossible the application of AVO and elastic inversion, hence limiting our ability to extract valuable information about lithology and fluid content. On the other hand, irregular acquisition affects the completeness of the data due to the missing traces, which negatively impacts vital processes such as thorough velocity analysis required by depth migration.

Constrained least-squares migration allows us both to reduce the aliasing related artifacts and the prediction of the missing traces. This is implemented by iteratively minimizing the difference between the input data and the modeled data from the proposed reflectivity, initially approximated by conventionally migrated data. Modeling is implemented through demigration. The minimization is achieved by the conjugate gradient method to solve the resulting overdetermined system of equations, which requires an iterative implementation of a demigration-migration pair. With an appropriate choice of a penalty function, we restrict the reconstruction of the data to geological constraints (e.g., smooth variation in the offset domain).

In the present work, I utilize a simple median filter in the 2D models presented in the Appendix to penalize non-flat events in common-reflection point gathers. For the 3D numerical examples I utilized a structure-oriented filter applied to the common-offset gathers.

A by-product of this process is the option to interpolate missing traces or generate regularly sampled traces from irregularly acquired datasets, which may then be used as input to wave-equation migration methods. The flexibility in the choice of the constraint function allows us to select the most appropriate filter to solve our specific problem. The main disadvantage of CLSM is the considerable increase in computing time.

MOTIVATION

Most of Mexico's 3D seismic surveys are acquired on land or in shallow marine environments, both of which are characterized by "obstacles" to acquisition, with the corresponding degradation of the seismic data quality. For instance, in the Mexico's largest producing field, Cantarell, producing platforms form holes in the seismic surveys. On land, the obstacles can take the form of steep slopes, swamps, environmental preserves, human habitations, and archeological sites, as occurred in the Chiapas-Tabasco basin. The current seismic imaging methodology used in these surveys is 3D prestack time migration.

The goal of my thesis is to prototype an improved time-migration algorithm and develop a workflow that can provide not only superior stacked images, but superior gathers amenable to AVO and elastic inversion analysis, as well as the possibility to better predict datasets suitable for depth migration.

INTRODUCTION

When considering migration of irregularly sampled 3D data, Kirchhoff migration is not only more computationally efficient, but avoids the interpolation of data traces, which is mandatory for wave-equation migration methods (Ronen and Liner, 2000). Nevertheless, as we find with most processing methods, Kirchhoff migration exhibits important flaws. Migration artifacts, cause mainly by operator and data aliasing, constitute the main drawback of the Kirchhoff algorithm. In the shallow parts of the final migrated volume these artifacts are closely related to the acquisition geometry, giving rise to acquisition footprint. This leaked noise and migration artifacts seriously interfere with the ability of the interpreter to identify geological features of interest, frequently masking or even obliterating them, leading to erroneous interpretation and either missed opportunities or dry holes.

The inaccuracy of the migration operator applied to sparse surface measurements to approximate the inverse of the forward modeling operator is a function of the acquisition geometry (Nemeth, 1996). In other words, the Hessian matrix that relates the true reflectivity to the migrated image is not diagonal dominant (Ren et al., 2011), but constitutes a blurring operator that smears the energy of the point scatterers that constitute the seismic events (e.g. Hu et al., 2001; Yu et al., 2006; Aoki and Schuster, 2009). Cable feathering in marine acquisition and obstacles in land acquisition further complicate the problem (Ronen and Liner, 2000). Irregularly sampled data makes velocity analysis ambiguous and prone to errors. Data aliasing and acquisition footprint are other important consequences of these irregularities. One of the more promising solutions to these aliasing and footprint problems is the application of least-squares migration. Least-squares migration has been investigated by Nemeth (1996), Nemeth et al. (1999), Schuster (1997), and many others, with the objective of attenuating acquisition footprint and data aliasing while minimizing the loss of geological signal that can occur using more conventional filtering methods. Kühl and Sacchi (2003) found that unconstrained least-squares migration often yields the same results as conventional migration. Specifically, they show that the least-squares migrated stacked section is not always superior to the conventionally migrated stacked section, due to the “healing effect of stacking” (Kühl and Sacchi, 2003). Duquet et al. (2000) generated superior results by applying similarity constraints across the common-reflection point gathers. More recently, Wang and Sacchi (2009) applied dip-oriented and prediction error constraints in the migrated common offset domain. Both of these approaches improved the quality of the final stacked result as well as the input gathers. On the other hand, Kühl and Sacchi (2001; 2003) proposed the use of the wave-equation operators in their implementation of least-squares migration.

Given the size of the data input, all present-day least-squares migration algorithms solve the system of matrix equations iteratively, with the cost of the computation directly proportional to the number of iterations. For this reason, significant effort has applied to preconditioning the data and/or the matrices to reduce the number of iterations, and therefore, the cost of the procedure. For instance, Aoki and Schuster (2009) proposed the use of a deblurring filter, similar to the migration-deconvolution operator, to precondition the data, whereas Wang et al. (2005) implemented preconditioning by using a first-derivative operator and a low-pass filter to play the role of its inverse.

Constrained Least-Squares Migration (CLSM) consists of minimizing the residual error (in a least-squares sense) between the data and the remodeled data obtained by "demigrating" the filtered (or otherwise constrained) migrated gathers, which constitute our approximation to the Earth's reflectivity. After the computation of the residual error, the modeled reflectivity (migrated gathers) is updated and the process is repeated until the minimum criterion is met or the desired number of iterations is reached. It is important to exclude the dead or otherwise missing traces from the calculations to prevent their prediction.

The advantages of CLSM when compared with conventional prestack time Kirchhoff migration include: better estimation of the reflectivity of the subsurface in a least-squares sense (Duquet et al., 2000); the reduction of aliasing artifacts, acquisition footprint, ground-roll and other coherent noise; the improvement of the signal-to-noise ratio on common-reflection point gathers. These constitute vital factors in the prestack analysis as AVO (Yi and Hu, 2003) and elastic inversion.

In this thesis, I develop and calibrate a constrained least-squares time migration algorithm amenable to application to irregularly sampled data.

In Chapter I, I discuss some relevant aspects about Kirchhoff migration, Kirchhoff demigration and their implementation together in the CLSM method using the conjugate gradient method. I place the mathematical details in the Appendix, and use rather a simple 2D model to more clearly present the methodology.

In Chapter II, I introduce the CLSM method, showing how it can be used to predict full, regularly sampled acquisition from decimated gathers generated over a synthetic salt model. I also show the improvement of the prestack common-offset and common-reflection point gathers.

In Chapter III, I present numerical results of the application of CLSM in a 3D dataset to illustrate the ability of the method to attenuate acquisition footprint. I include the calculations of some seismic attributes to better illustrate this result.

In Chapter IV, I discuss the overall results of this thesis, and summarize my conclusions.

Finally, in the Appendix I present the details of the mathematical background of the conjugate-gradient implementation of the CLSM method, illustrating each step with simple 2D models.

CHAPTER I

KIRCHHOFF MIGRATION AND DEMIGRATION

I.1 Practical implementation of Kirchhoff migration

Prestack 3D Kirchhoff migration can be implemented using the formula (Bleistein, 2001; Zhang et al., 2002; Biondi, 2006)

$$\mathbf{m}(\tau, \mathbf{r}, \mathbf{x_h}) = \iiint_{\Omega} A_m \, \partial_t [\mathbf{d}(t, \mathbf{x_m}, \mathbf{x_h})] \mathrm{d}\mathbf{x_m}, \qquad \text{(I.1)}$$

where $\mathbf{d}(\mathbf{x_m},\mathbf{x_h},t)$ constitute the 3D seismic data sorted in common-shot gathers, $\mathbf{m}(\mathbf{r},\mathbf{x_h},\tau)$ are the migrated common-reflection point gathers, A_m are the migration coefficients, $\mathbf{x_m}$ and $\mathbf{x_h}$ are the midpoint and offset position vectors respectively, $\mathbf{r} = (x,y)$ is the horizontal projection of the image-coordinates vector (Biondi, 2006), t is the two-way traveltime, τ is the migration vertical time, and ∂_t constitutes the time derivative applied to the common-shot gathers. Ω represents the migration aperture (Jäger, 2001).

Traveltimes in time migration are calculated analytically (Biondi, 2006) using the double square root formula

$$t = \left[\tau^2 + \frac{|\mathbf{r}-\mathbf{x_s}|^2}{V_{rms}^2(\tau)}\right]^{\frac{1}{2}} + \left[\tau^2 + \frac{|\mathbf{r}-\mathbf{x_g}|^2}{V_{rms}^2(\tau)}\right]^{\frac{1}{2}}, \qquad \text{(I.2)}$$

where V_{rms} is the root mean-square velocity, and $\mathbf{x_s}$ and $\mathbf{x_g}$ are the source and receiver group position vectors respectively, which relate to midpoint and offset through the well-known relations

$$\mathbf{x}_{\boldsymbol{m}} = \frac{\mathbf{x_g}+\mathbf{x_s}}{2}, \qquad \text{(I.3a)}$$

and

$$\mathbf{x}_{\boldsymbol{h}} = \frac{\mathbf{x_g}-\mathbf{x_s}}{2}. \qquad \text{(I.3b)}$$

The implementation of the equation I.1 is shown in the following pseudo-code, where h_{min} and h_{max} are the minimum and maximum offset to be migrated, and t_s and t_g are the traveltimes from image point to source and image point to receiver group, respectively:

```
loop all data traces $j_{traces}$ = 1, $n_{traces}$
!  precompute $\partial_t d$
   d_deriv = derivative(d)
   sx = sx($j_{traces}$); gx = gx($j_{traces}$)
   sy = sy($j_{traces}$); gy = gy($j_{traces}$)
   hx = |gx-sx|/2; hy = |gy-sy|/2
!  calculate traveltimes $t_s$ and $t_g$
   if  $h_{min} \le h \le h_{max}$
      loop all $j_\tau = 1, n_\tau$
         $\tau = (j_\tau - 1)*\Delta\tau$
         loop all $j_x = 1, n_x$
            $x = (j_x - 1)*\Delta x$
            loop all $j_y = 1, n_y$
               $y = (j_y - 1)*\Delta y$
               $t = t_s(j_\tau, j_x, j_y) + t_g(j_\tau, j_x, j_y)$
               $j_t$ = NINT(t/$\Delta$t)
               if  $j_t <= n_t$
                  $m(j_\tau, j_x, j_y, j_{hx}, j_{hy}) = m(j_\tau, j_x, j_y, j_{hx}, j_{hy})$ +
                                    $A(j_t, j_{sx}, j_{gx}, j_{sy}, j_{gy})$* d_deriv($j_t, j_{sx}, j_{gx}, j_{sy}, j_{gy}$)
               end if
            end loop y
         end loop x
      end loop $\tau$
    end if
end loop  $j_{traces}$
```

We observe that the input data consist of a five-dimensional array recorded in time, with shot and group domains deployed over typically different two-dimensional surfaces. After prestack time migration, the output data map onto a five-dimensional array, varying vertically in pseudo-depth or vertical two-way travel time, two lateral dimensions for each timeslice and two additional dimensions in the offset domain (most commonly offset magnitude and azimuth). Summing (stacking) over these last two dimensions, we obtain the final migrated image (volume) $\mathbf{m}(\tau,x,y)$.

I.2 Practical implementation of Kirchhoff demigration

Kirchhoff migration can be regarded as the adjoint operator of Kirchhoff modeling (Nemeth et al., 1999), as it constitutes the first approximation in the estimation of the seismic reflectivity. To perform least-squares migration we use demigration to approximate the modeling operation. Following Bleistein (2001), Zhang et al. (2002), and Biondi (2006), the 3D demigration formula is given as

$$\mathbf{d}(t,\mathbf{x_s},\mathbf{x_g}) = \iiint_{\Psi} A_d\, \partial_\tau [\mathbf{m}(\tau,\mathbf{r_1},\mathbf{r_2})]\mathrm{d}\mathbf{r_1}\mathrm{d}\mathbf{r_2}, \qquad \text{(I.4)}$$

where $\mathbf{d}(\mathbf{x_m},\mathbf{x_h},t)$ constitutes the 3D modeled common-shot gathers, $\mathbf{m}(\mathbf{r},\mathbf{x_h},\tau)$ are the corresponding 3D migrated common-reflection point gathers, A_d are the demigration coefficients, and typically ∂_τ constitutes the vertical derivative applied to the common-reflection point gathers. Ψ represents the demigration aperture (Jäger, 2001).

One important step in the Kirchhoff demigration process is to determine the isochrones that rule the summation in equation I.1. In time demigration, they are implicitly given by the equation I.2, such that in the 2D case it appears that we may be able to solve explicitly for τ:

$$\tau = \sqrt{t^2 - \frac{(x-x_s)^2+(x-x_g)^2}{V_{rms}^2(\tau)}}. \qquad \text{(I.5)}$$

Unfortunately, V_{rms} is also a function of vertical time τ, such that we cannot use equation I.5 directly to obtain a sample index

$$j_\tau = \text{NINT}(\frac{\tau}{\Delta\tau}), \qquad \text{(I.6)}$$

as we do in equation I.2 for the traveltimes during migration. $\Delta\tau$ is the sampling interval in the vertical migration time domain, and the Fortran function NINT rounds to the nearest integer number. As expected, this difficulty occurs in the 3D case too.

For this reason, one can proceed in a similar manner as in migration, modeling the seismic data **d**(j_t,x_s,x_g) according to the pseudo-code shown below:

```
loop all data traces $j_{traces} = 1, n_{traces}$
  sx = sx($j_{traces}$); gx = gx($j_{traces}$)
  sy = sy($j_{traces}$); gy = gy($j_{traces}$)
  hx = |gx-sx|/2; hy = |gy-sy|/2
  ! calculate traveltimes $t_s$ and $t_g$
  if  hmin ≤ h ≤ hmax
  !  precompute $\partial_t$m
    m_deriv = derivative(m)
    loop all $j_\tau = 1, n_\tau$
      $\tau = (j_\tau - 1)*\Delta\tau$
      loop all $j_x = 1, n_x$
        $x = (j_x - 1)*\Delta x$
        loop all $j_y = 1, n_y$
          $y = (j_y - 1)*\Delta y$
          $t = t_s(j_\tau, j_x, j_y) + t_g(j_\tau, j_x, j_y)$
          $j_t$ = NINT(t/$\Delta$t)
          if  $j_t <= n_t$
            d($j_t$, $j_{sx}$, $j_{gx}$, $j_{sy}$, $j_{gy}$) = d($j_t$, $j_{sx}$, $j_{gx}$, $j_{sy}$, $j_{gy}$)  +
                                A($j_t$, $j_{sx}$, $j_{gx}$, $j_{sy}$, $j_{gy}$)* m_deriv($j_\tau$, $j_x$, $j_y$, $j_{hx}$, $j_{hy}$)
```

```
          end if
        end loop y
      end loop x
    end loop $\tau$
  end if
end loop $j_{traces}$
```

The demigration pseudo-code shown above has about the same time performance as the migration pseudo-code in the previous section, since we have simply interchanged the roles played by the arrays **d** and **m**. However, the resulting isochrones *τ(t)* do not present uniform time sampling, which can easily produce missing or repeated values at particular output samples, negatively affecting the final amplitudes as isochrones surfaces only partially contribute to the construction of the modeled image. A much better, although far more time-consuming alternative is to uniformly interpolate the traveltimes, as shown in the following pseudo-code:

```
loop all $j_t = 1, n_t$
    $t_{int} = (j_t - 1)*\Delta t$
    loop all $j_\tau = 1, n_\tau$
        $t_{left} = t(j_\tau - 1)$
        $t_{right} = t(j_\tau)$
        if $t_{left} \leq t_{int} \leq t_{right}$
            $\tau_{left} = (j_\tau - 1)* \Delta\tau$
            $\tau_{int}(j_t) = \tau_{left} + \Delta\tau *(t_{int} - t_{left}) /(t_{right} - t_{left})$
        end if
    end loop $\tau$
end loop t
```

With this interpolation of the traveltimes we generate a single isochrone that falls on each sample thereby providing a good approximation to modeling using demigration, which is vital to adequately implement CLSM.

CHAPTER II

CONSTRAINED LEAST-SQUARES MIGRATION

In the previous chapter, I described the implementation of Kirchhoff prestack migration and demigration as a forward-adjoint operator pair. Here I put together the elements that constitute the basics of the CLSM method. The mathematical details are explained in the Appendix.

We can represent equations I.1 and I.4 in matrix notation as follows:

$$\mathbf{d} = \mathbf{Gm}, \qquad \text{(II.1)}$$

$$\mathbf{m'} = \mathbf{G}^{\mathrm{T}}\mathbf{d}, \qquad \text{(II.2)}$$

where **G** constitutes the forward modeling operator, **m** is the regularly sampled model (Chemingui and Biondi, 2002) that represent the Earth's reflectivity, $\mathbf{G}^{\mathrm{T}}$ is the adjoint operator and **m**' is the estimate of the true Earth's reflectivity **m** using such an operator. Kirchhoff demigration represents the forward modeling operator and Kirchhoff migration represents the adjoint operator.

Substituting equation II.1 into equation II.2 gives

$$\mathbf{m'} = \mathbf{G}^{\mathrm{T}}\mathbf{Gm}. \qquad \text{(II.3)}$$

From this relation observe that the estimated reflectivity, **m'**, relates to the true Earth's reflectivity, **m**, through the Hessian matrix $\mathbf{G}^{\mathrm{T}}\mathbf{G}$. Note that if the migration operator accurately approximates the inverse of the modeling process, $\mathbf{G}^{\mathrm{T}}\mathbf{G}$ tends to the identity matrix, **I**, and the estimated reflectivity **m**' tends to the true reflectivity **m**. Nemeth (1996) observes that the elements of the matrix $\mathbf{G}^{\mathrm{T}}\mathbf{G}$ depend on the geometrical arrangement of the sources and receivers. Such a dependency directly impacts the fidelity of the estimated reflectivity **m**', which often exhibits a pattern correlated to the surface acquisition geometry, giving rise to acquisition footprint. In the case of a dense acquisition geometry, the off-diagonal elements of $\mathbf{G}^T\mathbf{G}$ become negligible, giving rise to a diagonally dominant matrix. In such ideal case the migration operator can accurately reconstruct the Earth's reflectivity.

For reasons of cost and equipment limitations, 3D seismic data is rarely, if ever acquired uniformly in all five dimensions (Ronen and Liner, 2000). Further complications are obstacles and permit limitations in land, transition zone and shallow water acquisition and cable feathering in offshore acquisition, which introduce additional irregularities in the geometry (Ronen and Liner, 2000). For these reasons 3D seismic data frequently exhibit gaps that generate aliasing artifacts in the migrated images and limit the accuracy of the velocity analysis (Duquet et al., 2000). Finally, the adjoint operator of migration can fail in approximating the forward modeling process and can be unable to represent every single recorded event. However, by preparing a demigration operator based on the migration code, one can ensure that only those events properly handled by the migration algorithm are going to be modeled (Duquet et al., 2000).

Aliasing artifacts in seismic migration constitute the product of imperfect constructive and destructive interference of single impulse responses (smiles) of the migration operator, which is the result of a coarse acquisition geometry that does not honor the Nyquist criterion in the space domain. To illustrate this problem, I use the synthetic dataset based on the E.T. salt velocity model (Figure II.1a), which represents a salt diapir that pierces the overlain beds, consisting of high velocity carbonates (in red) and low velocity siliciclastics (in blue) with velocities that increase with depth, a typical scenario in the Salina del Istmo Basin, Mexico. A representative sector of the corresponding shot gathers is shown in Figure II.1b. To illustrate the impact of sparse acquisition, I randomly zeroed out (killed) two thirds of the seismic traces of the original shot gathers (Figures II.2a and II.2b) to simulate a severe irregular acquisition problem. In Figure II.3a observe how smile-shaped aliasing artifacts affect the common-offset gathers, whereas in Figure II.3b the same artifacts give a checkerboard appearance in the common-reflection point gathers. These effects correspond to the incompleteness of the decimated data. While stacking is a powerful filter that can attenuate most of the aliasing in the final stacked section (Figure II.4), the unstacked migrated gathers are too contaminated by aliased for AVO or elastic inversion.

Acquisition footprint constitutes a particular case of spatial aliasing in 3D data that is tightly coupled to the acquisition geometry. The effect of the dense receivers and sources along shot and receiver lines (or alternatively along some other regular stencil such as bricks) results in patterns of either stronger or weaker amplitudes as well as stronger or weaker coherent noise rejection on the subsurface image. Due to stretch mute (or migration emergence angle limitations) shallower times slices exhibit stronger footprint than deeper time slices. Stacking generally is not enough to attenuate acquisition footprint in the final 3D volume. As the fold increases, footprint becomes less severe, so it normally diminishes with depth. In the presence of complex structures (strong dips) or strong lateral velocity variations, acquisition footprint appears less organized, but still contaminates the resulting image. I will show synthetic examples of footprint and address footprint suppression using 3D CLSM in Chapter III.

In addition to these problems, the unmigrated data by itself might have not sufficient density to provide detailed velocity analysis. In this case CLSM can interpolate the surface traces so that conventional velocity analysis algorithms perform well.

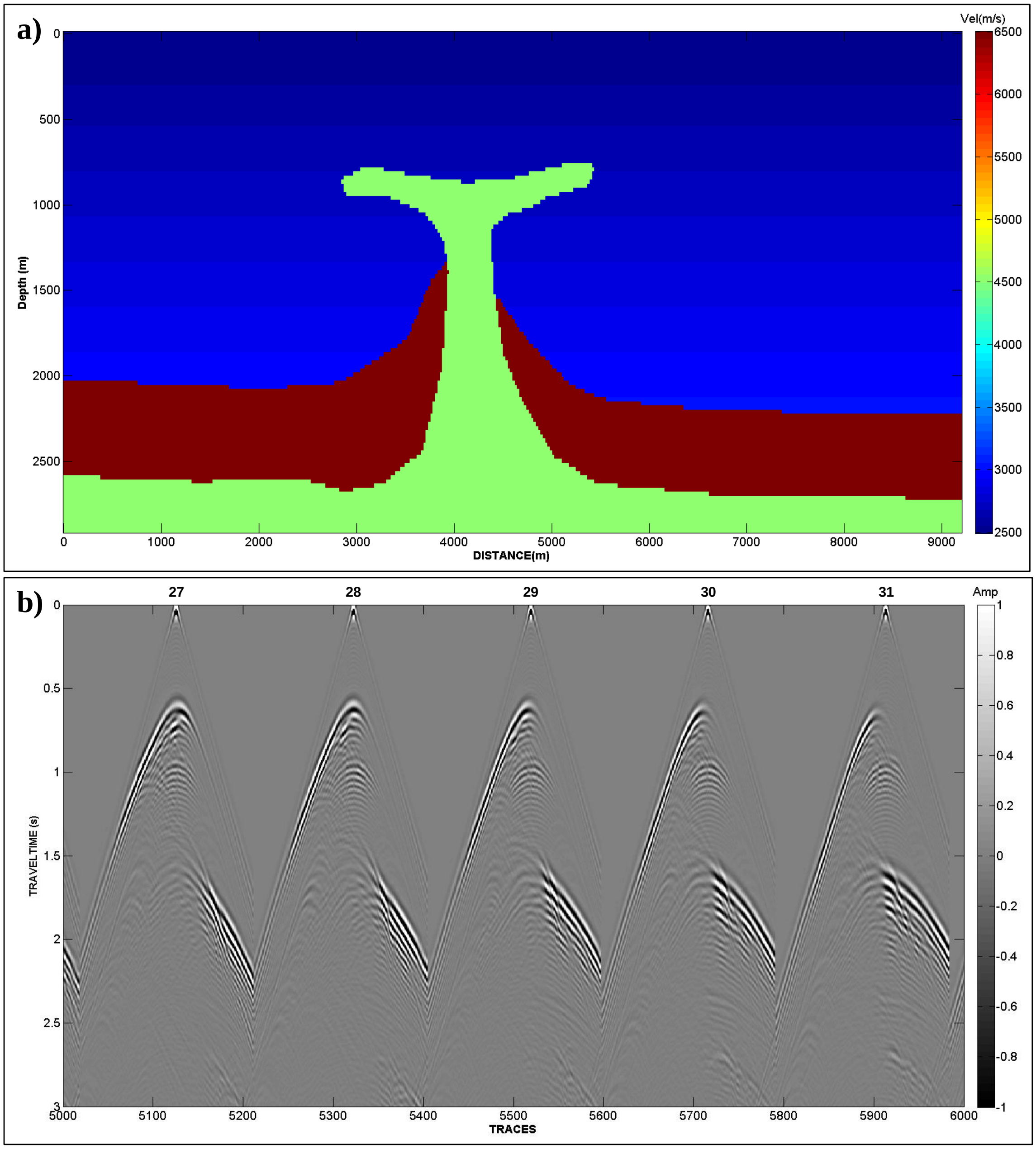

Figure II.1.- (a) Velocity depth model of the ET salt structure. (b) Representative common-shot gathers generated using a finite difference solution of the scalar wave equation. Note dispersion in the waveforms due to insufficient spatial sampling of the model.

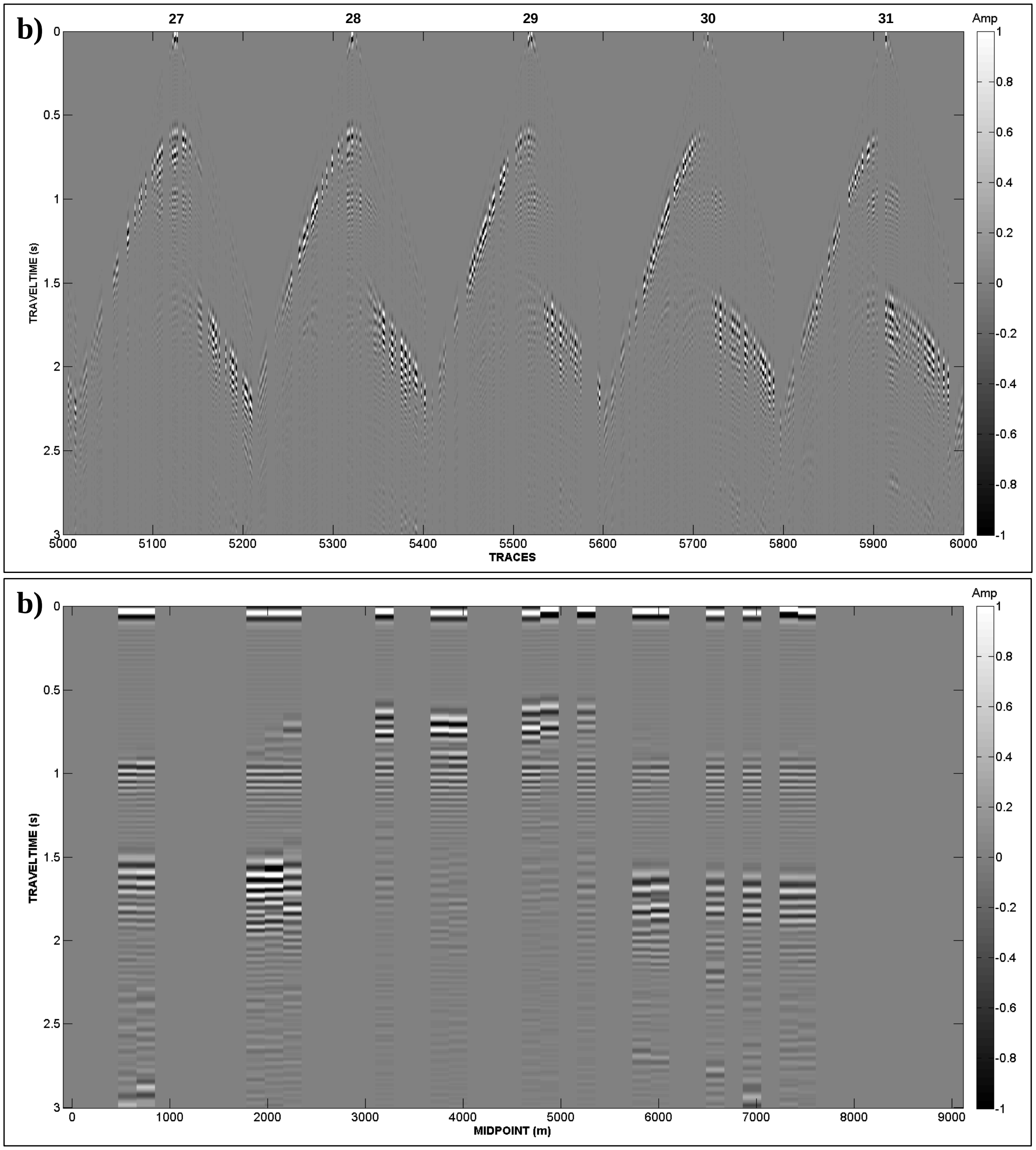

Figure II.2.- (a) Common-shot gathers shown in Figure II.1b, after decimation, killing two thirds of the traces. (b) Unmigrated near-offset section (*h* = 150 m), which shows the severe effect of the decimation of the data.

The CLSM method can handle these limitations, helping to attenuate aliasing and acquisition footprint by minimizing (in the least-squares sense) the error between the original data and the remodeled data that results from the assumption that the migrated gathers represent the Earth's reflectivity (Duquet et al., 2000). I use demigration to perform the modeling. After computing the error I update the migrated gathers, remodel, recalculate the error, and repeat the process until either the error falls below the desired value or the maximum number of iterations is reached. I use the conjugate gradient method to perform the minimization. Appendix I summarizes the basic theoretical aspects of the conjugate gradient method as well as details of how I introduced constraints into the optimization.

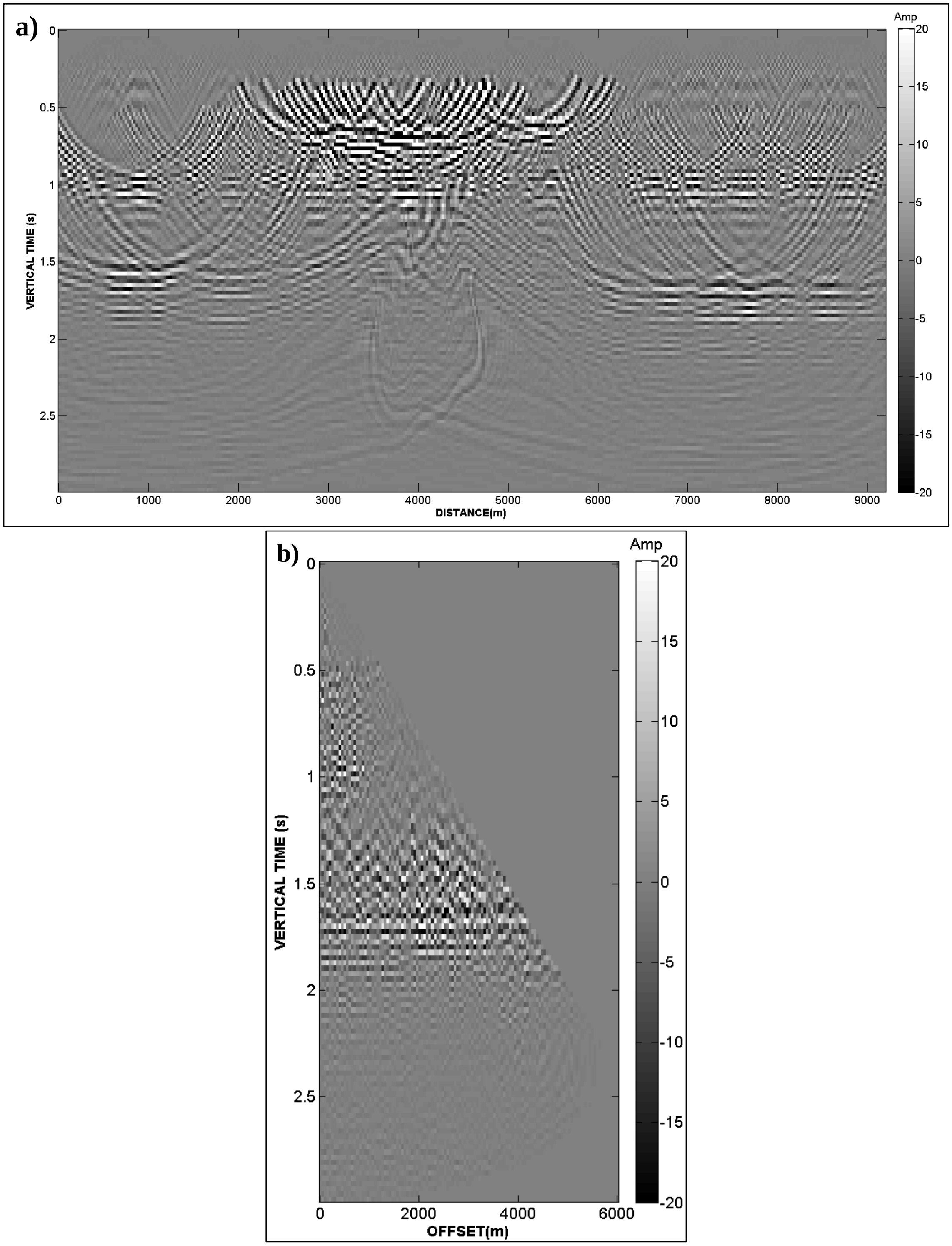

Figure II.3.- (a) Migrated near-offset section (h = 150 m) computed from the decimated data displayed in Figure II.2b, showing the aliased artifacts that prevent any interpretation of the data. (b) Common reflection point gather at location x = 7176 m, showing the aliased artifacts that contaminate the otherwise flat events.

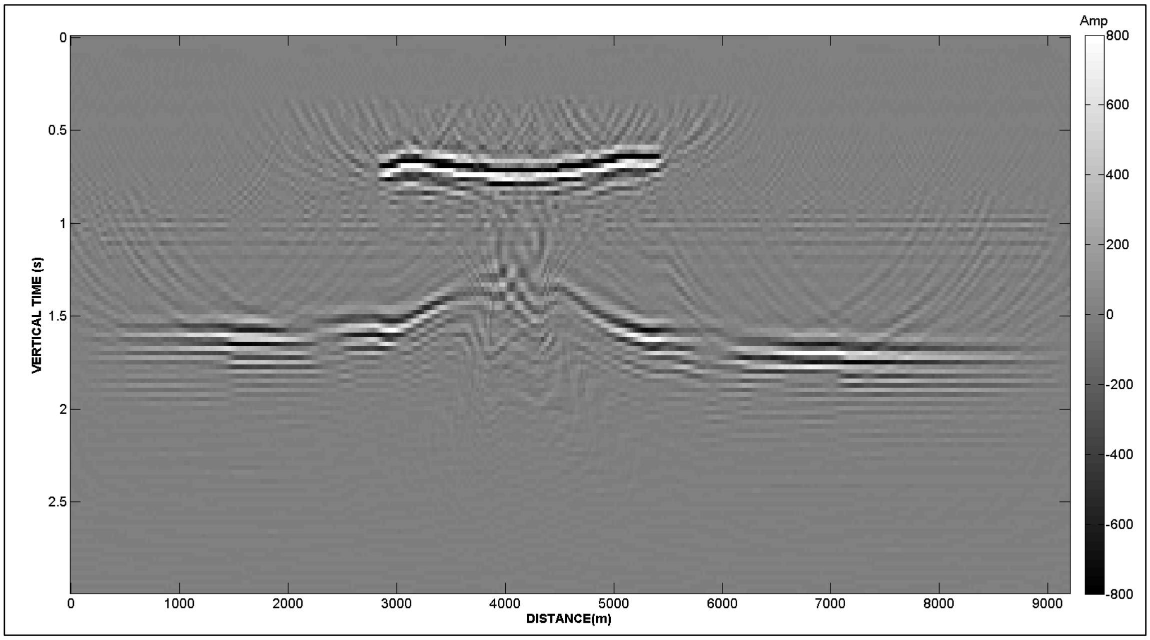

Figure II.4.- Final stacked section of the decimated data using the conventional migration algorithm described by equation I.1. Most aliasing artifacts have been attenuated by the stacking process.

In the case of the missing traces in the input or "data" space, CLSM allows the prediction of the missing data over a regular geometry, which constitutes a model driven trace interpolation (Ronen and Liner, 2000). This prediction occurs because the gaps in the data domain correspond to the aliased artifacts in the migration domain. Attenuating such artifacts in the migration domain facilitates the interpolation in the data domain. For this reason, one important aspect of the CLSM method is the selection of the constraint function which modifies the migrated gathers, selecting which seismic events should be kept and which should be rejected. In this study we assume that each common offset section illuminates the same geology, such that the resulting migrated images should vary smoothly between adjacent common-offset gathers. This assumption is almost always true for prestack time migration. In contrast, for prestack depth migration, ray kinking and shadow effects can give rise to offset-to-offset discontinuities. This assumption is equivalent to restricting the common-reflection point gathers to contain nearly flat events (or moderate smiles and frowns for incorrect migration velocities), since rapid changes across offset are unlikely to constitute valid AVO variations (Duquet et al., 2000). I implement those smoothness constraints through the use of a simple median filter in 2D calculations, and a structure-oriented filter in the 3D calculations.

Only the live traces are migrated and fit using least-squares. However, after the final iteration the final migrated image was used to model (or demigrate) the both live and dead traces thereby generating an "interpolation" (Figure II-5). Note that since direct wave events are not predicted by Kirchhoff modeling, the data was preconditioned by using an appropriate muting function to filter out those events.

Figure II-6a shows the common-offset section at h = 150 m, where the aliasing artifacts that contaminated the conventionally migrated gathers have been strongly attenuated, allowing the interpretation of the salt image, which was impossible in the conventionally migrated section. Figure II-6b shows the common-reflection point gather, where most non-flat artifacts have been attenuated. Note that one could use such results for prestack processes like elastic inversion; in contrast, the conventionally migrated gathers are very noisy. On the other hand, the CLSM stacked section (Figure II.7) is not significantly different than the conventionally migrated image.

Figure II.8 shows a plot of the residual, the magnitude of the gradient (or simply the gradient) and the model difference (see Appendix) that allow us to control the convergence of the method. The residual is the difference between the observed and the modeled data; note that it decreases monotonically with each iteration as our estimation of the reflectivity improves. The gradient is a vector which is oriented to seek the path to the minimum error; its magnitude also decreases monotonically with each iteration. Finally, the model difference is used to monitor how the migrated gathers change with increasing iteration.

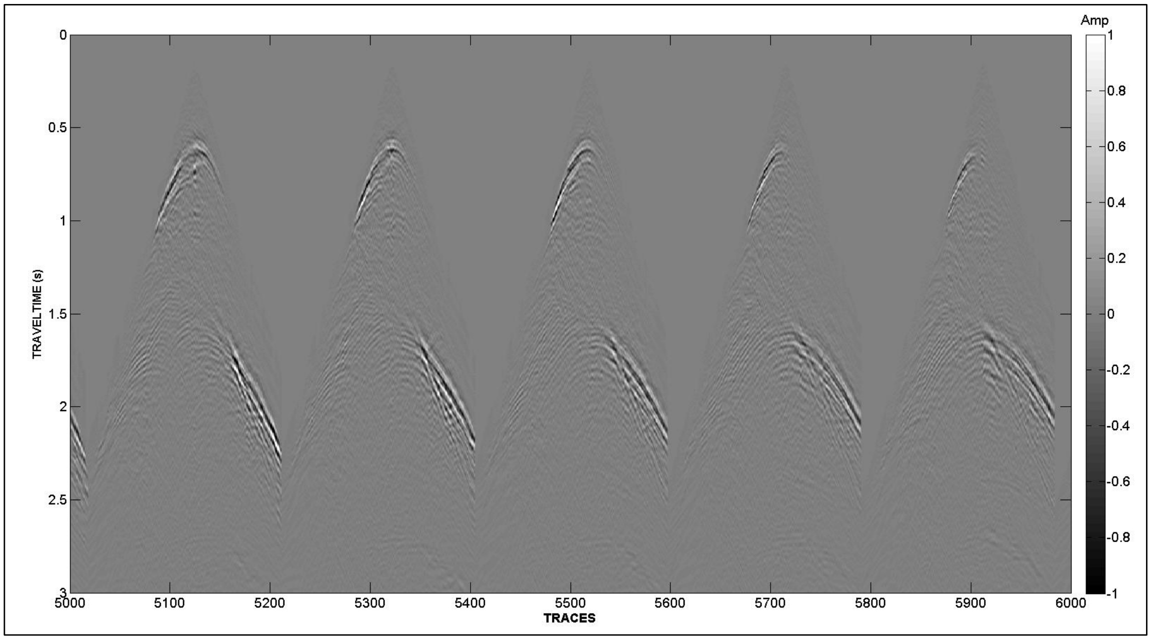

Figure II.5.- Detail of the reconstructed common-shot gathers using the reflectivity model obtained after CLSM. When compared with Figure II.1, note that the direct waves are not predicted since they are not modeled by the Kirchhoff algorithm.

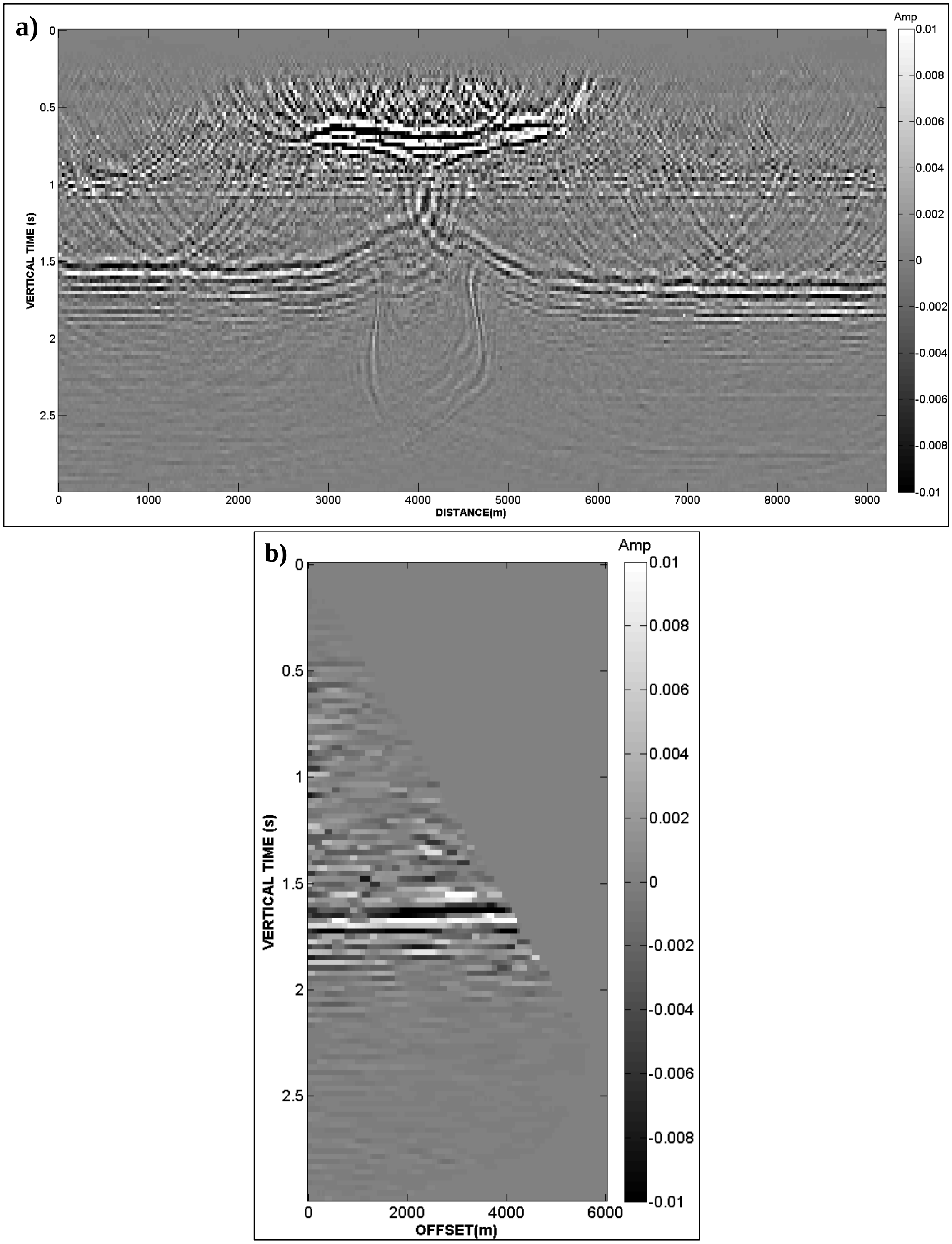

Figure II.6.- (a) CLSM migration of the near common-offset gather at *h* = 150 m, corresponding to the image shown in Figure II.3a. Note the attenuation of the aliasing artifacts after CLSM such that we can see the underlying geology. (b) Common-reflection point gather at *x* = 7176 m, showing retention of flat signal and suppression of the steeply dipping noise seen in Figure II.3b.

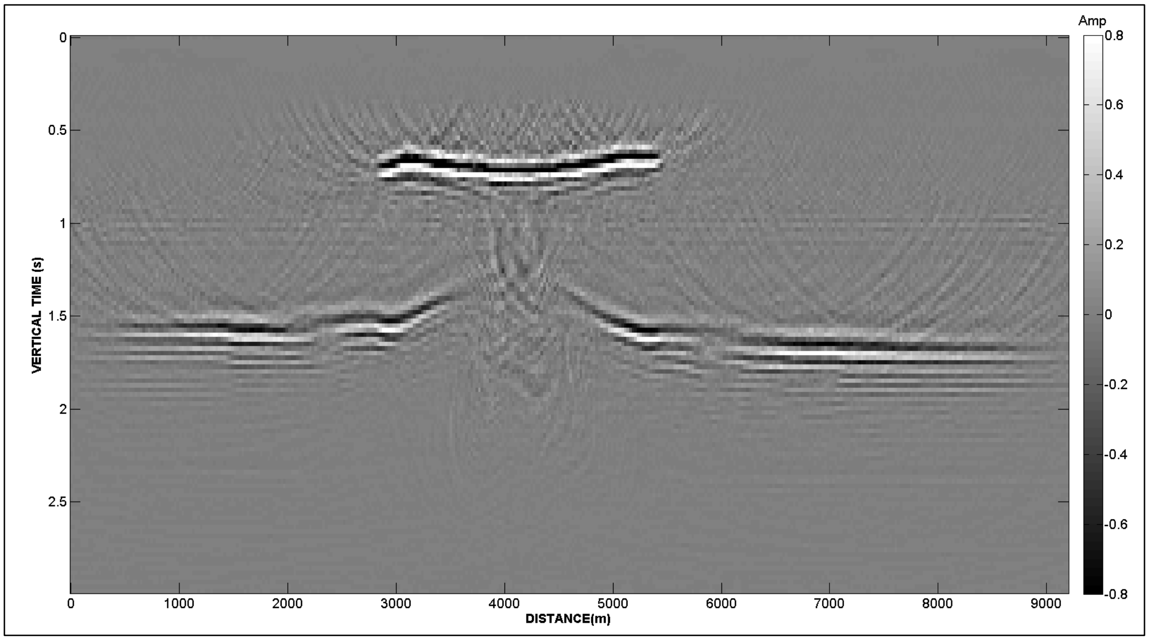

Figure II.7.- Salt model: Final stacked section of the CLSM gathers. There is not further improvement when compared with the conventional migration full stack section (Figure II.3).

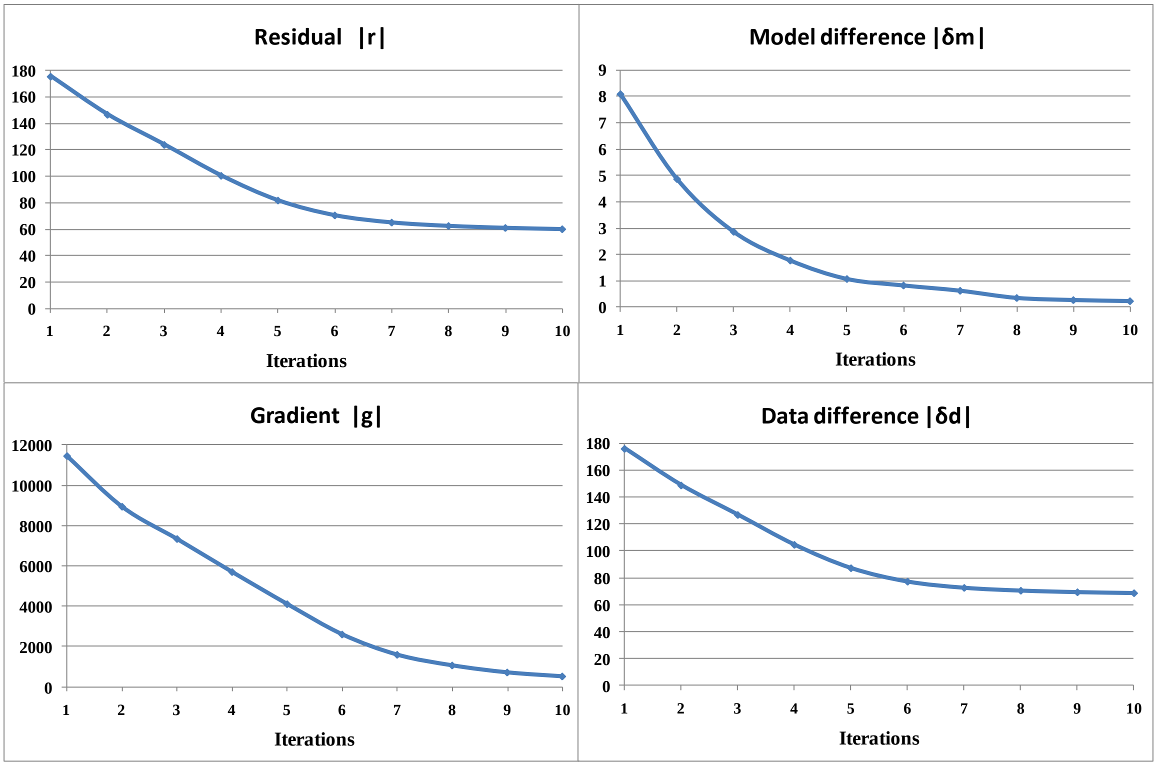

Figure II.8.- Behavior of (a) the residual, $\|\mathbf{r}\|$, (b) the gradient, $\|\mathbf{g}\|$, (c) the model difference $\|\boldsymbol{\delta}\mathbf{m}\|$ and (d) the data difference, $\|\boldsymbol{\delta}\mathbf{d}\|$, defined by equations A11, A12, A17 and A18 in the Appendix A.

CHAPTER III

3D CLSM: NUMERICAL EXAMPLES

In this section I test the CLSM algorithm on the 3D Dickman survey, acquired by Grand Mesa Operating Company in Ness County, west Kansas. I compare the performance of CLSM using 3 iterations versus conventional migration, evaluating the attenuation of migration artifacts in the migrated gathers, the improvement of the corresponding predicted datasets compared to the original data, and the attenuation of acquisition footprint in the stacked migrated volume.

Algorithm description

I wrote the software in Fortran 95/2003 utilizing a C++ GUI that interacts with a bash script shell to define the input the parameters. The software runs on distributed nodes using the public domain message passing interface (MPI). An overview of the software modules is provided in Appendix E.

The 3D CSLM software consists of seven main programs and three auxiliary programs that interact together in the script using a loop over the iteration number. This arrangement allows a better memory usage than a single program consisting of subroutines, and provides the flexibility to choose a constraint function program, such as median filters across common-reflection point gathers and structure-oriented filtering across common-offset gathers (as used here), or Radon transforms and other common filters used in AVO data conditioning.

The main programs are:

a) First migration. This step constitutes the zeroth iteration or the conventional migration, and performs the operation $\mathbf{G}^{\mathbf{T}}\mathbf{d}_{\mathbf{0}}$ described by equation A9 in the Appendix to obtain the initial gradient. If the CLSM option is not indicated, the software performs conventional Kirchhoff migration using only this program.

b) Demigration. This program performs the operation $\mathbf{Gh}_i$ that is required by equation A13. The results of this demigration are used to update the model and the residual as indicated by equations A10 and A11.

c) Second migration. This is the migration step that alternates with demigration in the conjugate gradient method, described by equation A12, thereby updating the gradient, and the next search direction $\mathbf{h}_i$.

d) Constraint function. In the 3D code I utilize a structure-oriented filter over the migrated gathers (AASPI program sof4d), instead of the simple median filter used in the previous two-dimensional examples (equation A15). This algorithm is similar to the poststack SOF filter described by Davogustto-Cataldo (2011), but operates on migrated common-offset gathers rather than on the stacked data volume. One can choose between mean, median and principal component filters (Chopra and Marfurt, 2007). For the numerical examples shown here, I chose the median filter. The input are the common reflection point gathers that constitute the updated reflectivity model $\mathbf{m}_i$.

e) Dip computation. AASPI program dip3d determines the inline and crossline apparent dips (Chopra and Marfurt, 2007) using a stacked volume calculated from the updated model, which are additional input for the sof4d program.

f) Stacking. The updated model $\mathbf{m}_i$ is stacked to determine the inline and crossline dip components just mentioned above. AASPI program stack was used.

g) Update of search direction. I found that it is convenient to execute this step in a separate program. It solves equation A16 isolating the search direction $\mathbf{h}_i$. This update is required only if the constraint function is used.

Auxiliary programs sort the data from common-offset gathers to common reflection point gathers and vice versa, as required, and apply a mute that suppresses any numerical artifact that could arise from the sof4d filter.

A simplified flowchart of the 3D CLSM algorithm is shown in Figure III.1. A more detailed flowchart is provided in the Appendix.

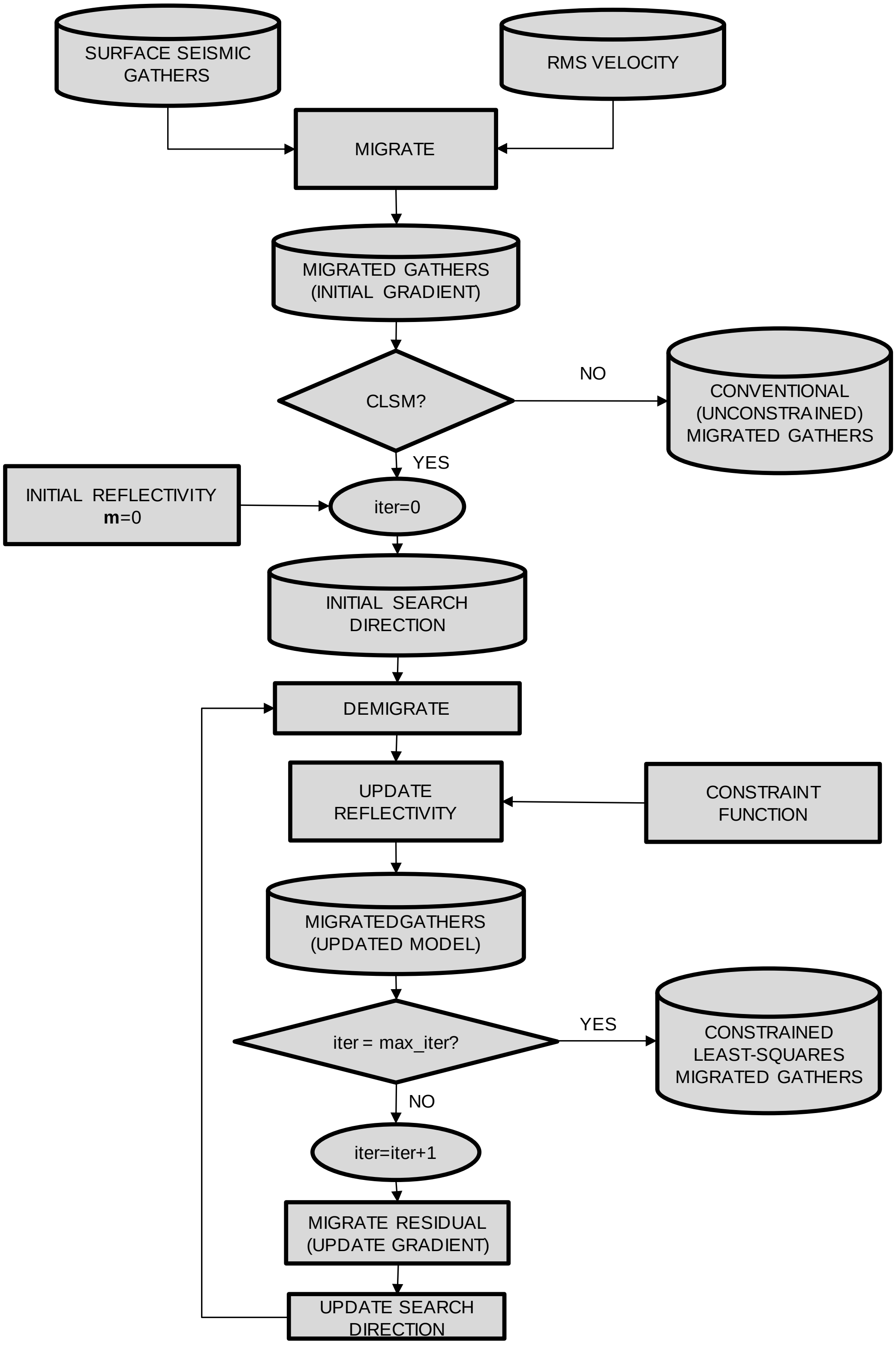

Figure III.1.- Flowchart of the 3D CLSM algorithm.

Data space, model space, null space and weights

Nemeth (1996) considers least-squares migration to be a generalized Radon transform, where the linear or parabolic moveout routinely used in processing CMP gathers is replaced by the Green's function **G**. This analogy helps us understand not only the limitations and pitfalls of least-squares migration, but also provides insight into how to remedy the situation by proper preconditioning.

Reviewing these concepts, note that undersampling the data spatially gives rise to holes in the data space. Similar holes arise due to geology, where certain areas of the subsurface are unilluminated due to overlying high velocity lenses or anomalously strong attenuation. Holes in the model space occur when we properly record shear waves, converted waves, Rayleigh waves, head waves, and multiples, but do not include them in our Green's function, **G**, that approximates only simple reflection and diffraction PP events.

If we wish to image our data with PP Kirchhoff prestack time migration, we should preprocess our data to reduce the shear wave, converted wave, Rayleigh wave, head wave and multiple events prior to migration. If Rayleigh waves are properly sampled, they will fall into the null space of our migration operator. If they are improperly sampled, they will appear to be longer wavelength and migrated as real events. The velocity of PP multiples is close to that of PP reflectors and will almost always be migrated as if they were real, deeper primary reflectors.

Ideally, one should first precondition the seismic data to eliminate these "unmodeled" events. If not, the weight function, **W**, and constraints, **C**, can also help. For instance, a constraint against multiples can be a conventional parabolic Radon transform applied to the migrated CRP gathers (Crider et al., 2008). If the head waves occur at shallow, farther offsets, we can simply minimize their impact by setting the weight of the misfit function, **W**, to be zero, stating that we cannot model this component of the data.

For the 2D synthetic examples discussed earlier, there was no need to work about attenuation other than the $1/\sqrt{R}$ geometric spreading in the Green's function. For the 3D real data, we have not only the $1/R$ spreading incorporated in Kirchhoff migration and modeling but also energy losses due to scattering and intrinsic attenuation (Q) that are not properly modeled. To address this issue we do the following: (1) Choose a value, α, that visually balances the common-shot gathers $\mathbf{d}(t)$ when multiplied by t^{α} (i.e., the early and late arrivals have similar amplitude), (2) remove the geometric spreading term, $1/R \sim 1/t = t^{-1}$, that is included in the Kirchhoff migration and modeling operators. Thus, the data input to the process will be $\mathbf{d}(t)t^{\alpha-1}$. Finally, we may wish to better fit the lower amplitude, deeper reflections, as well as the stronger amplitude, shallower reflections. If this is the case, we may wish to modify our weight function to be

$$\mathbf{W}(t,h) = \mathbf{M}(t,h)t,$$

where $\mathbf{M}(t,h)$ are our mutes and extra term t balances the data for geometric spreading.

Calibration

To calibrate the ability of CLSM to attenuate aliasing artifacts both from insufficient sampling and irregular coverage, in the Appendix I included three two-dimensional models from which I obtained the corresponding migrated gathers and show them as common-offset and common-reflection point gathers. I predict the data by demigrating such migrated gathers, and compare to the original datasets. Finally, I stack the migrated gathers to obtain the migrated sections. Then I compare the results from unconstrained and constrained least-squares migration with conventional migration. The overall results demonstrate that unconstrained least-squares migration restores the seismic amplitudes with only small attenuation (if any) of the aliasing artifacts, whereas the use of the constraint function, characterized in this case by a simple median filter, attenuates and in one case virtually eliminates those artifacts both from the migrated gathers and the predicted data.

The experience provided by the two-dimensional experiments shown in the Appendix allowed a much better algorithm development of the three-dimensional software, therefore improving the corresponding results.

Application

Figure III.2 shows a representative detail of the common-reflection point gathers after conventional migration. I applied a mute function with constant slope of 0.00015 s/ft to suppress the stretched zone. Some flat reflection events are visible around 420, 700, 800, and 900 ms. Other flat events are obscured by the aliasing artifacts that contaminate the gathers. Figure III.3 shows the same detail after one iteration of CLSM.

The continuity of the flat events previously identified is improved, and other formerly faint reflections can be identified after the attenuation of steeply dipping aliased artifacts. Figures III.4 and III.5 show how after two and three iterations respectively, aliased artifacts are further suppressed and the seismic reflectors improve in continuity. Such results benefit prestack interpretation including residual velocity analysis, AVO, elastic impedance inversion, and anisotropy analysis.

Figure III.6 shows a detail of the original (or input) common-shot gathers. Noise obscures and sometimes almost completely obliterates the reflectors. In addition to traffic and wind noise, ground roll, head waves, shear waves and converted waves contaminate the desired PP reflectors and diffractions of interest. Figure III.7 shows the same detail after the reconstruction achieved by demigrating the conventionally migrated gathers. The use of the mute function took its toll preventing the reconstruction of the shallow section in the farther offsets. The prediction yields only a small improvement in the visibility of the seismic events. Worse yet, the order of magnitude is completely different. Figures III.8 - III.10 show the progressive reconstruction after the demigration of the CLSM migrated gathers after one, two, and three iterations respectively. It is evident that the progressive attenuation of the random and coherent noise in the migrated gathers corresponds to the improvement in the continuity and definition of the previously hidden reflectors, and the order of magnitude of these data much better approximates the order of magnitude of the original shot gathers. The result either of the second or the third iteration (Figures III.9 and III.10) can be used both to perform a better velocity analysis and depth migration. Reconstruction of the far offsets would require retention of the stretched zone in the migrated gathers.

Figure III.11 shows the seismic volume resulted after stacking the conventionally migrated gathers (Figure III.2). The stacking process eliminates some of the aliased artifacts. However, the wavy artifacts observed in the background and in some reflectors indicate the presence of acquisition footprint, which additionally obscures the shallow thin beds above 400 ms. Figures III.12 to III.14 show the stacked volumes after one, two, and three iterations respectively, corresponding to the migrated gathers in Figures III.3 to III.5. In a similar manner to the corresponding migrated gathers, there is a progressive reduction of acquisition footprint as successive iterations are applied. Even after only the first iteration (Figure III.3) the shallow thin beds greatly improve their continuity. The second iteration (Figure III.4) further attenuates most of the remaining artifacts that still affect the volume. The third iteration (Figure III.5) marginally removes more residual noise, but it begins to over-smooth some stratigraphic features.

Figure III.15 shows a timeslice at 850 ms through a possible channel feature in the conventionally migrated volume. There is a probable crevasse splay indicated by the yellow arrow and a feature that could be interpreted as a flood plain, indicated by the green arrow However, acquisition footprint severely affects the seismic data and prevents a thorough interpretation. Figure III.16 shows the same timeslice after one iteration of CLSM. The acquisition footprint is highly attenuated. The hypothetical flood plain becomes more discernible, and can be distinguished from the narrowest part of the channel. Some residual acquisition footprint is still visible in the gray areas. The second iteration (Figure III.17) eliminates this residual footprint and improves the contrast of the channel with the surrounding background geology. After the third iteration (Figure III.18) only small variations are observed, with some smoothing of the geologic features. The constraint function tends to smooth the geology, this is a side effect of the aliasing attenuation, but the least-squares migration process tends to deblur the migration impulse response, as observed by Hu et al. (1999) in migration deconvolution, which can be regarded as a simplification of least-squares migration. These opposite effects should be in equilibrium. In contrast, if the chosen constraint function is too "aggressive", it can surpass the deblurring effect of least-squares migration.

To better appreciate the effects of CLSM in the attenuation of acquisition footprint and the improvement of geologic detail, in the following figures I show the results from the computations of commonly used seismic attributes.

Figure III.19 shows a timeslice at 750 ms from a short-wavelength most-positive curvature volume corresponding to the conventionally migrated stacked volume. The acquisition footprint pattern is easily recognized, and it prevents any interpretation of subtle geological features. Here and henceforth, the highest absolute values of curvature correspond to the northwest area, where the fold is minimum. Figures III.20 to III.22 show the corresponding timeslice from the CLSM volumes after one, two, and three iterations respectively. After the first iteration (Figure III.20) the footprint pattern is notably attenuated, and it is progressively reduced until only residual long wavelength acquisition footprint still persists after the third iteration (Figure III.22). In contrast, geology-related lineaments become interpretable, even subtle features like the ones indicated by the yellow arrows, which can correspond to or a system of faults (Nissen et al., 2009) or braided channels.

Figure III.23 shows the same timeslice as the previous figures from a variance volume calculated from the conventionally migrated stacked volume. There can be inferred some geologic features, but the data is strongly contaminated by acquisition footprint. Figures III.24 to III.26 show the same timeslice from the CLSM volumes after one, two, and three iterations respectively. Now some carbonate-related collapse and/or dissolution features (Nissen et al., 2009) can be interpreted. The first iteration (Figure III.24) shows a dramatic attenuation of the acquisition footprint and other noise that formerly obscured the carbonate features, some of them indicated by the yellow arrows. The second iteration (Figure III.25) virtually removes the remaining checkerboard appearance and better differentiates some features. In contrast, the third iteration (Figure III.26), while further attenuates remaining artifacts, has the undesirable effect of over-smoothing some subtle geologic features.

Figure III.27 shows the timeslice at 850 ms of variance co-rendered with amplitude envelope calculated from the conventionally migrated volume. I made transparent the variance as indicated in the opacity scale. The channel observed in Figures III.15 to III.18 is delineated by the variance, including the interpreted crevasse splay and the flood plain (yellow and green arrows respectively), but other geologic features are not clearly defined. The high values of variance observed in the northwest lower fold area indicates the presence of noise. Acquisition footprint pattern is clearly visible in the amplitude. On the other hand, amplitude variations barely correlate to contrasts in variance, where we would expect collapse/dissolution features. In the first iteration of CLSM (Figure III.28) the variance becomes much cleaner, and the acquisition footprint is almost completely attenuated in the amplitude. Nevertheless, more important is the fact that some small low-amplitude anomalies now correlate to round and sub-round features in variance, as indicated by the red arrows. The aspect of the channel is cleaner too, and it is now evident the correlation of local amplitude minima with the presence of the channel. In the second iteration (Figure III.29) this correlation improves, and the remaining acquisition footprint is virtually eliminated. Variance becomes even cleaner, and the round features are still preserved. Finally, the third iteration (Figure III.30) shows better definition of the channel both in variance and amplitude, but at the cost of losing some round features in variance. In all the CLSM figures, the low-amplitude anomalies show good correlation to these rounded features in variance, which further supports their interpretation as collapse/dissolution features.

Figure III.31 shows the same timeslice with the variance co-rendered with short-wavelength most-negative curvature. To improve the display, in the opacity curve I made small values of variance completely transparent. Similar to the case of the amplitude envelope, there is small relation of the curvature with variance, mainly because the acquisition footprint pattern almost obliterates the geologic features in curvature, although the area inside the channel seems to be slightly cleaner than the neighborhood. With CLSM (Figures III.32 to III.34) it can be observed a progressive reduction of the footprint. It becomes clear that the channel constitutes a negative-curvature feature. There are other features that resemble smaller channels and fractures not detected by the variance, some of them indicated by the orange arrows. In this case, the third iteration (Figure III.34) seems to provide the best visualization of geologic features in the curvature, in spite of losing some detail in variance.

Finally, to illustrate the rejection of the aliased artifacts due to the use of the constraint function, I produced near-offset and medium-offset volumes with unconstrained and constrained LSM after one iteration, and computed the difference.

Near-offset volumes are shown in Figures III.35 to III.37. The unconstrained LSM volume (Figure III.35) contains a plethora of aliased artifacts, some of them more clearly identified in the shallow part of the left section. After using the constraint function (Figure III.36) large number of such artifacts are rejected, making possible the interpretation of some reflectors. Figure III.37 shows the rejected part, which demonstrates that the sof4d median filter adequately removes aliased artifacts, rejecting only some portions of coherent signal as observed in the right section between 200 and 700 ms. Medium-offset results (Figures III.38 to III.40) show even better results, retaining more signal. This can be explained by the higher signal to noise ratio of the medium-offset volume compared to the near-offset volume.

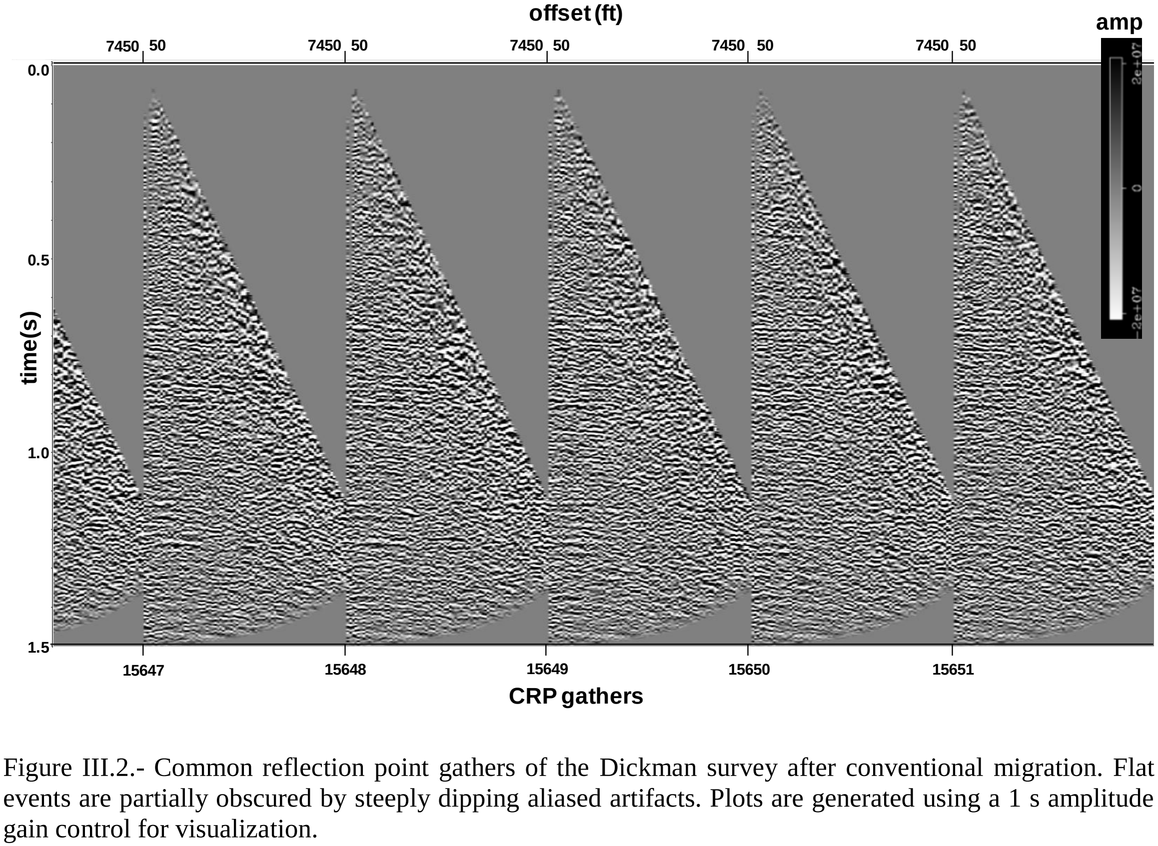

Figure III.2.- Common reflection point gathers of the Dickman survey after conventional migration. Flat events are partially obscured by steeply dipping aliased artifacts. Plots are generated using a 1 s amplitude gain control for visualization.

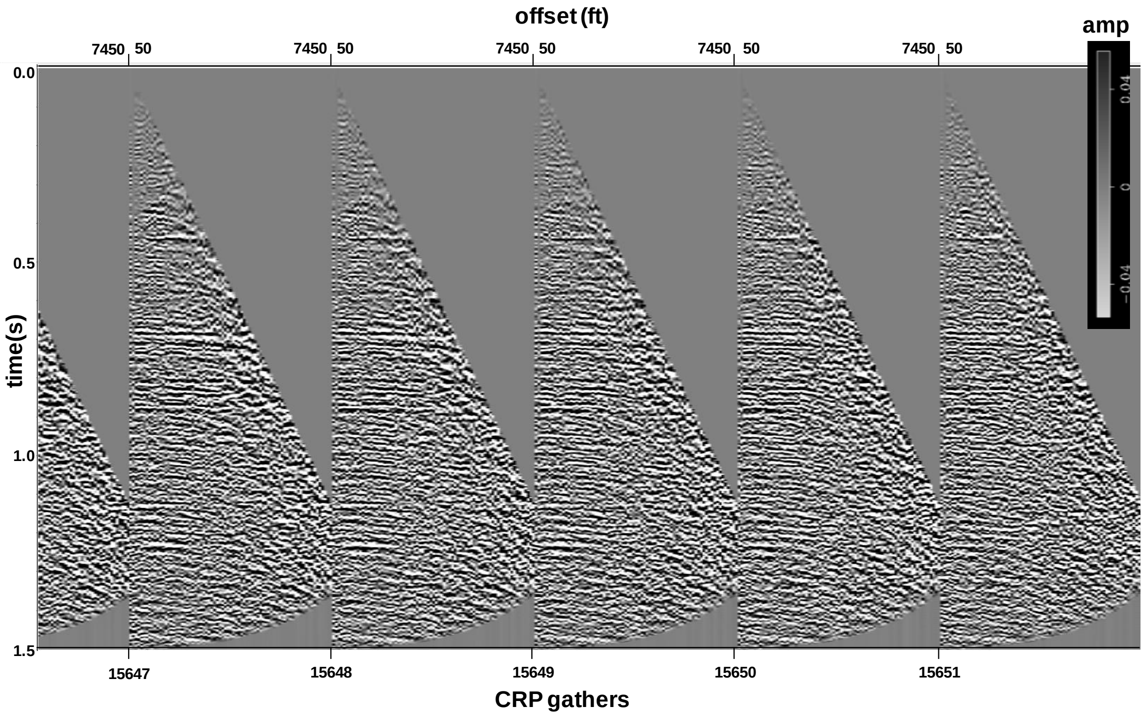

Figure III.3.- Common reflection point gathers of the Dickman survey after one iteration of CLSM. The observed reflectors improve in continuity and more subtle events become more discernible as steeply dipping artifacts are attenuated.

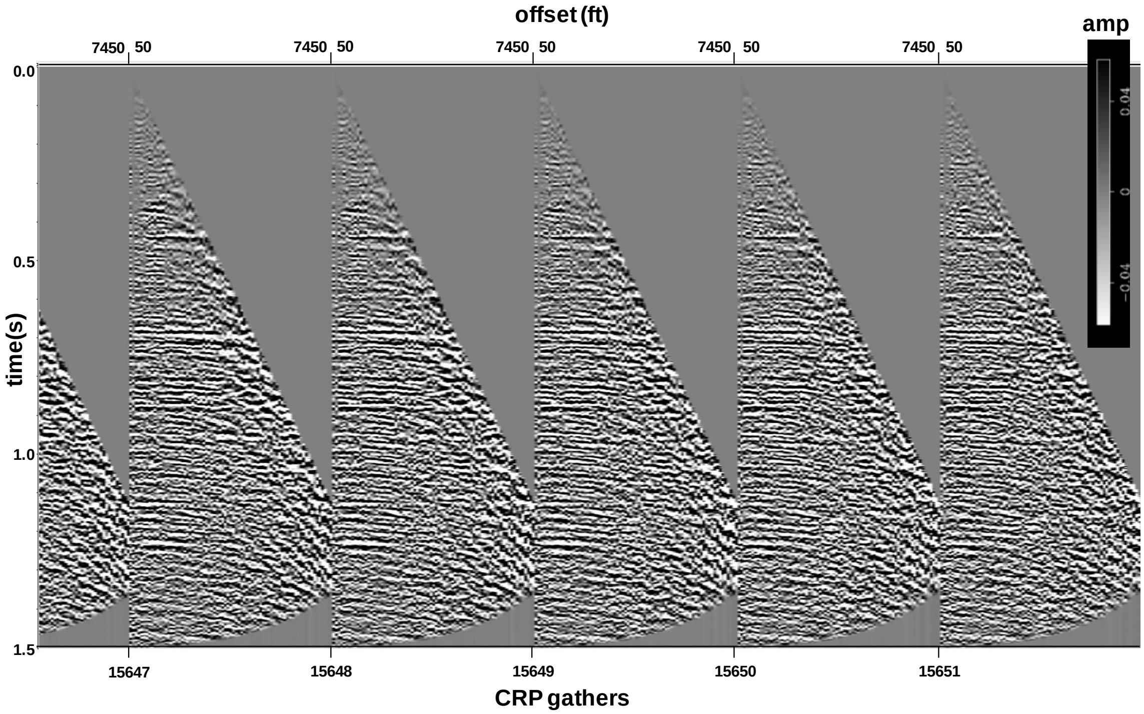

Figure III.4.- Common reflection point gathers of the Dickman survey after two iterations of CLSM. Better continuity is achieved and more artifacts are attenuated.

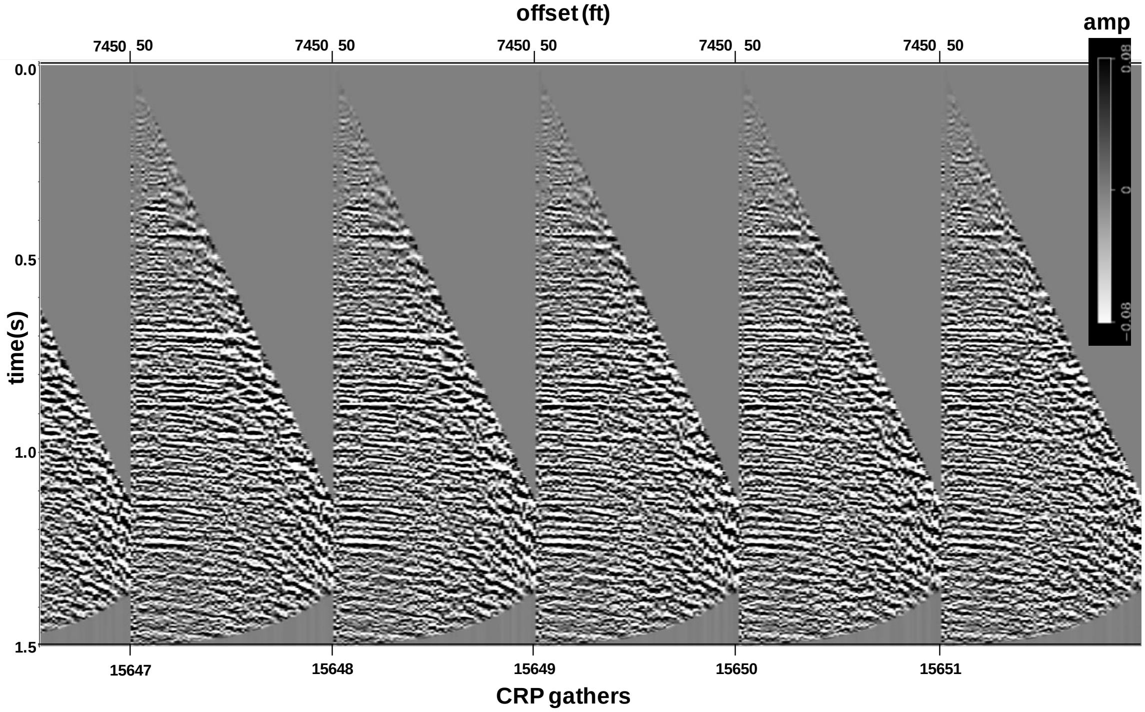

Figure III.5.- Common reflection point gathers of the Dickman survey after three iterations of CLSM. There is small improvement compared to the result obtained with two iterations.

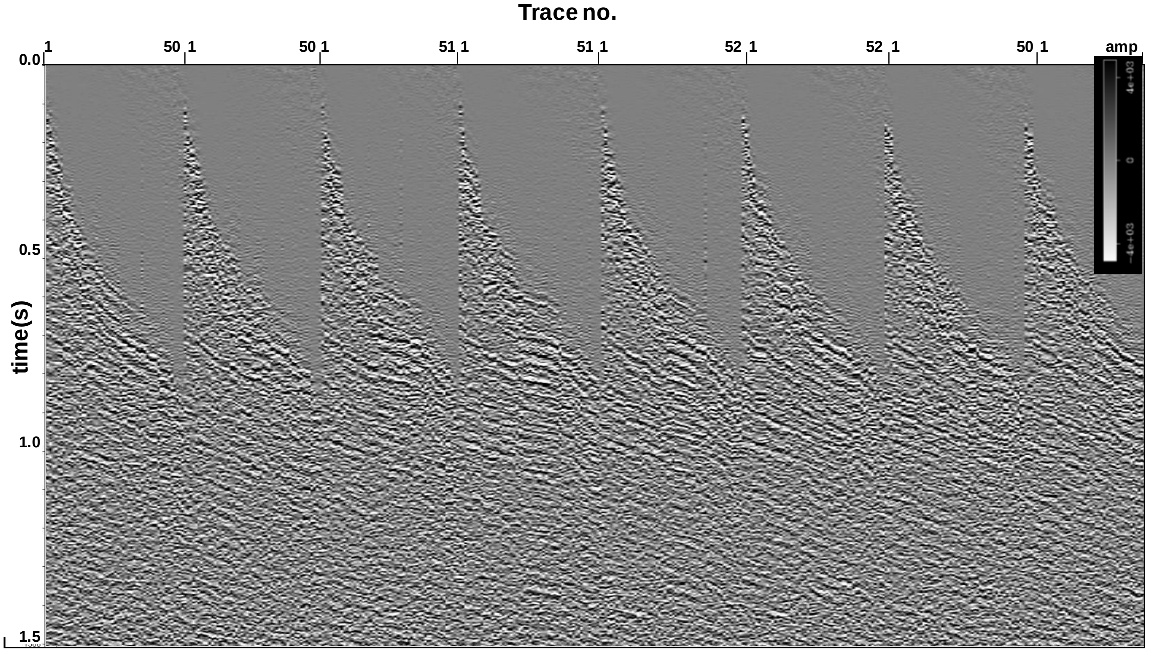

Figure III.6.- Representative input shot gathers for the Dickman survey. The number of traces varies with each shot gather across the survey. Traces are sorted by source-receiver offset with a maximum source-receiver offset is 4200 ft.

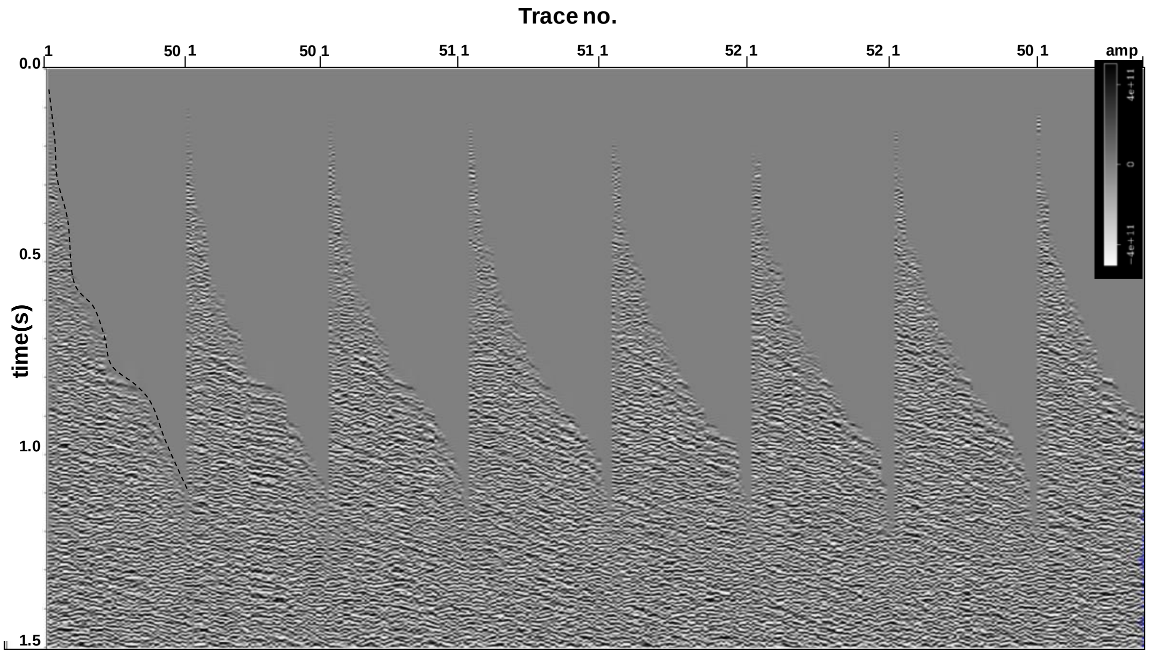

Figure III.7.- Dickman predicted dataset obtained by demigrating the conventionally migrated gathers. Dashed line indicates the mute t=h/v applied to the 3D gather.

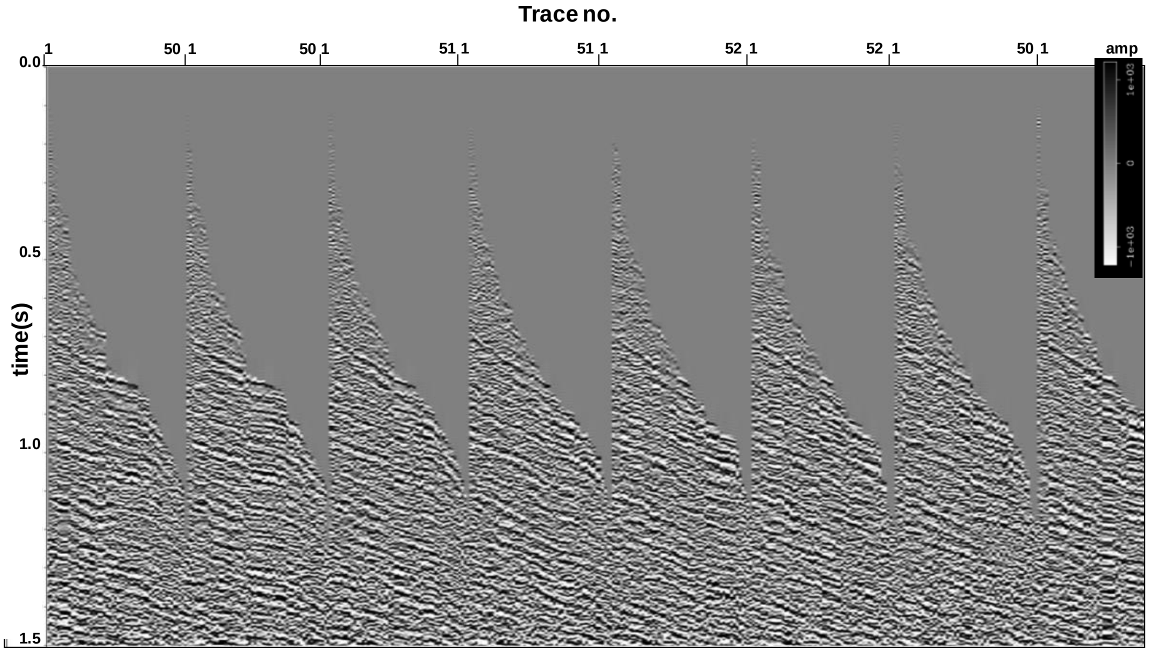

Figure III.8.- Dickman predicted dataset obtained by demigrating the CLSM gathers after one iteration.

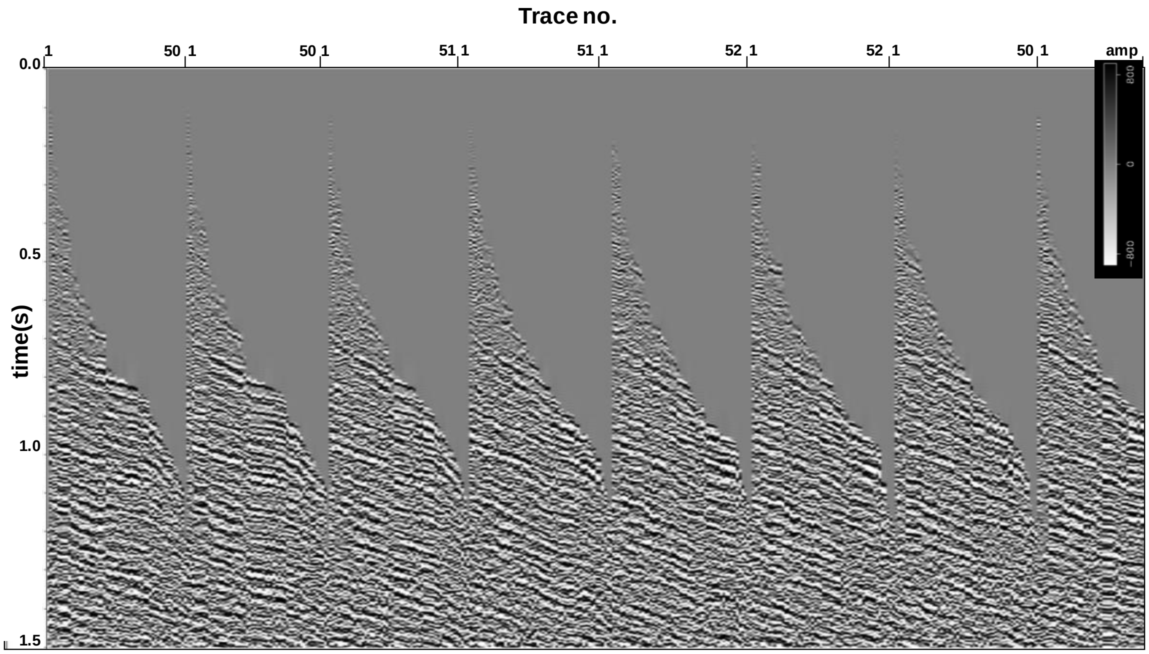

Figure III.9.- Dickman predicted dataset obtained by demigrating the CLSM gathers after two iterations.

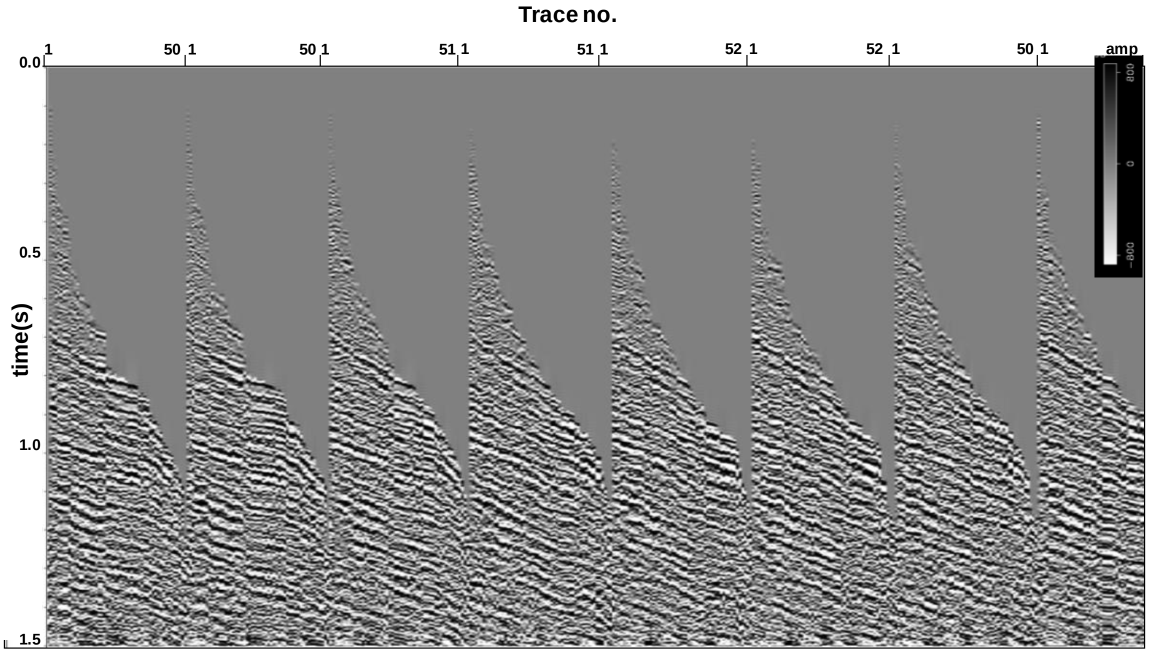

Figure III.10.- Dickman predicted dataset obtained by demigrating the CLSM gathers after three iterations.

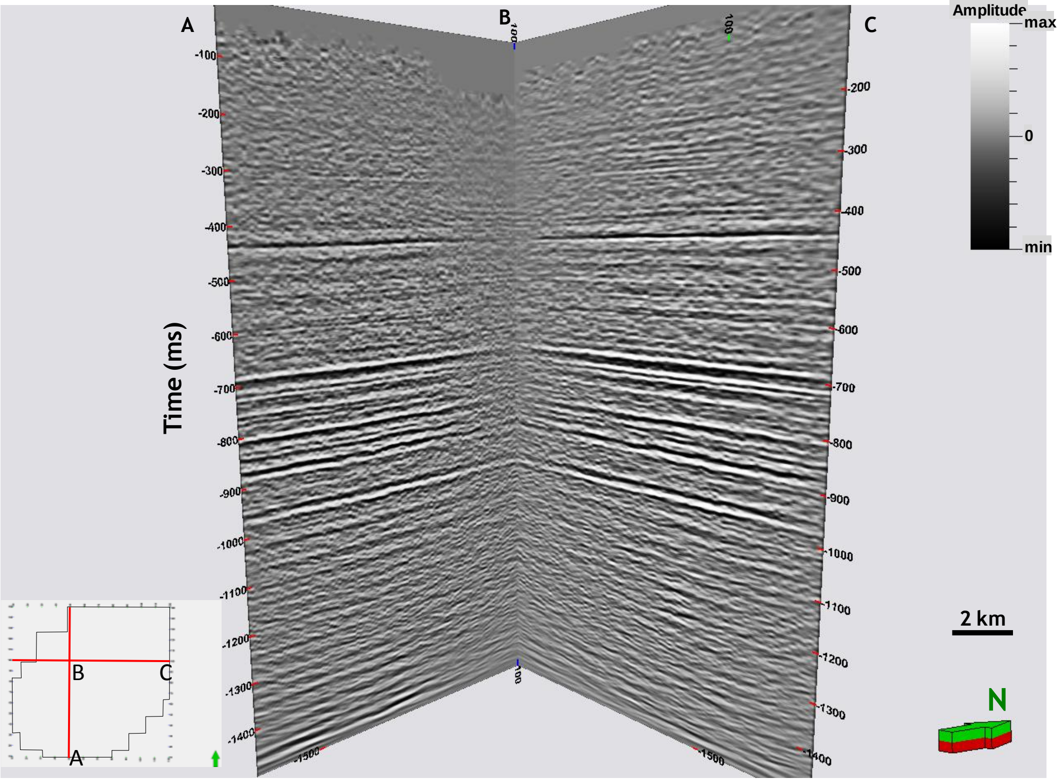

Figure III.11.- Dickman stacked volume after conventional migration.

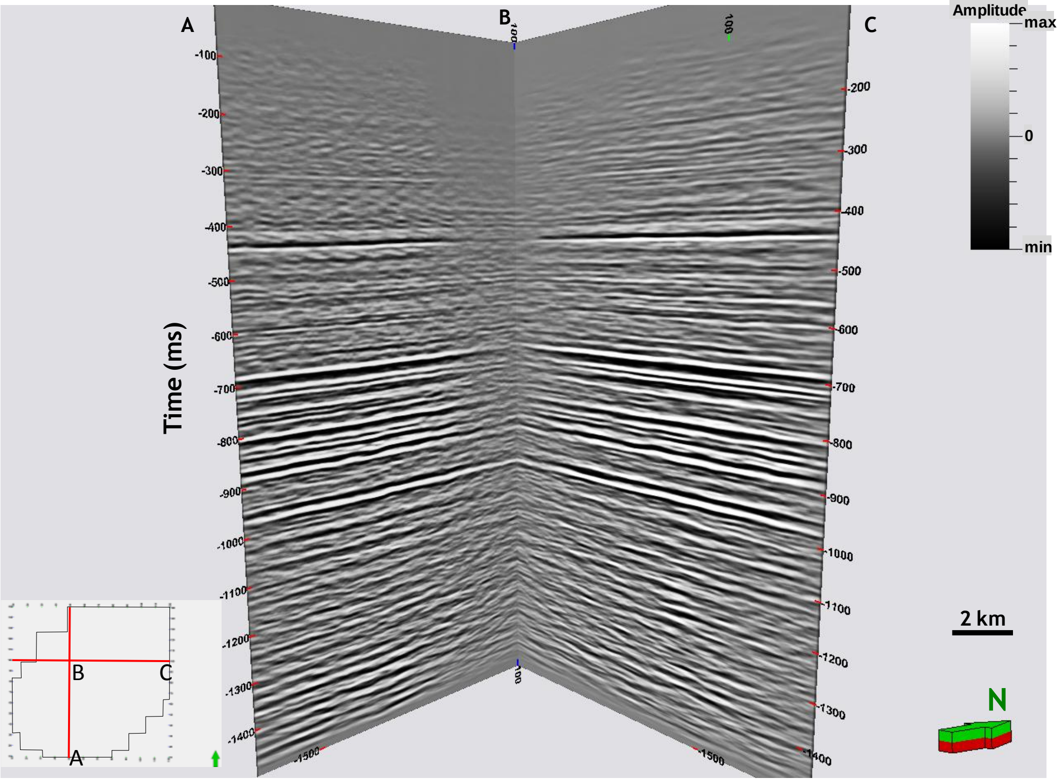

Figure III.12.- Dickman stacked volume after CLSM with one iteration.

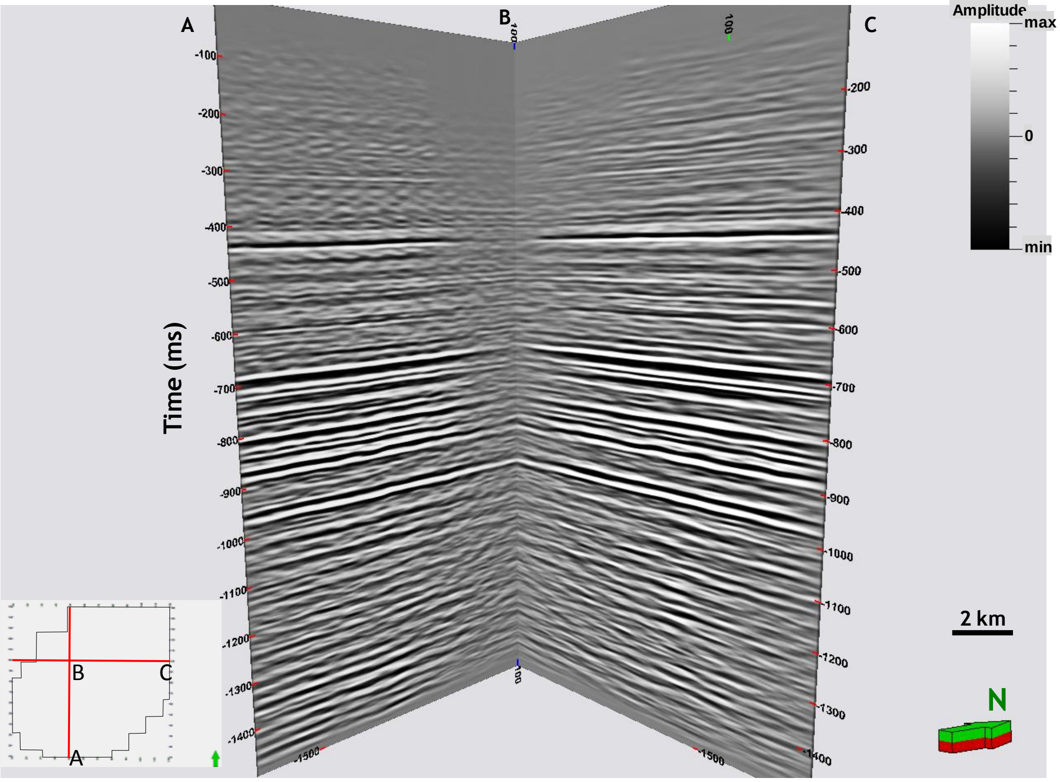

Figure III.13.- Dickman stacked volume after CLSM with two iterations.

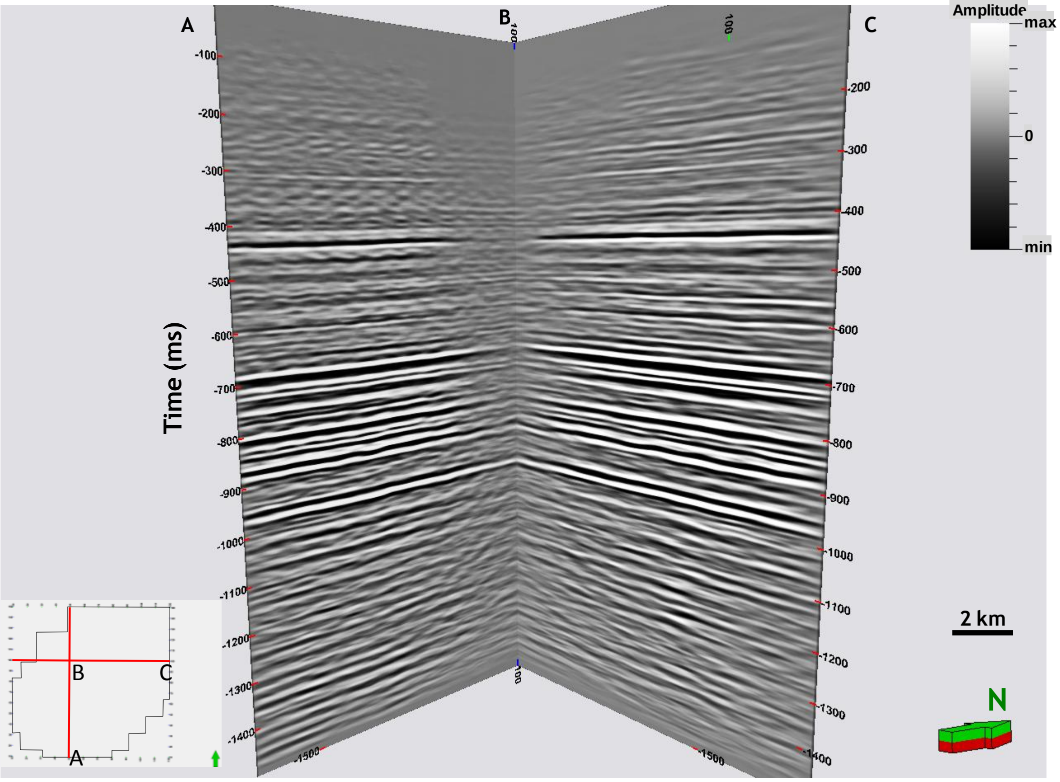

Figure III.14.- Dickman stacked volume after CLSM with three iterations.

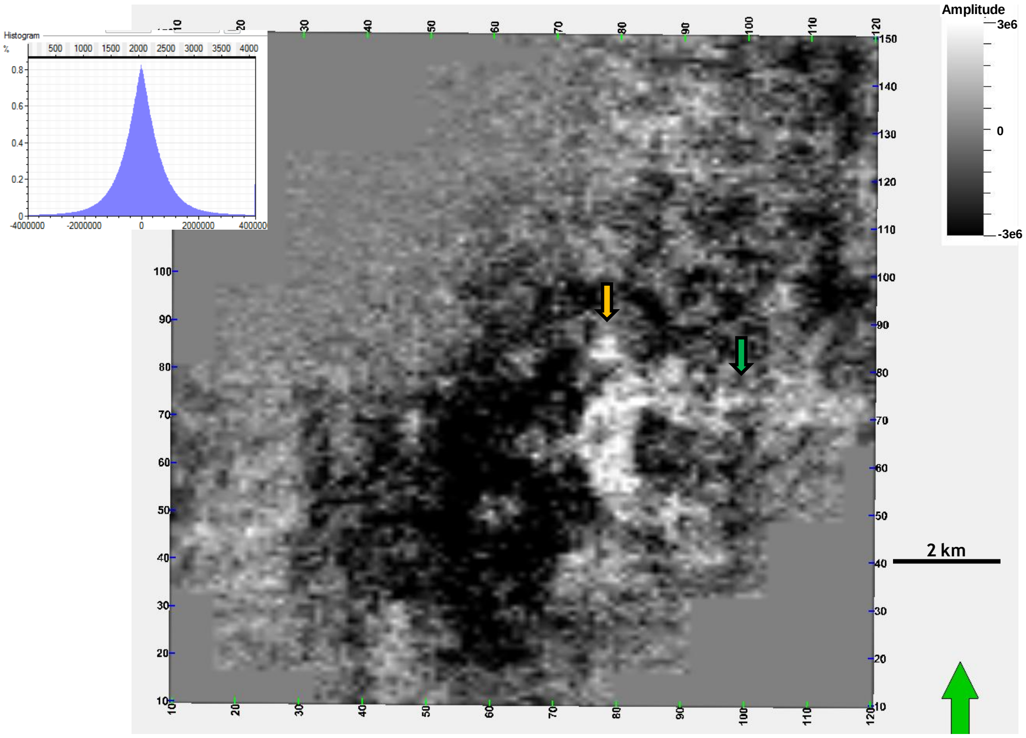

Figure III.15.- Timeslice at 850 ms of the Dickman stacked volume after conventional migration, showing the channel. Yellow and green arrows indicate a hypothetical crevasse splay and a flood plain, respectively.

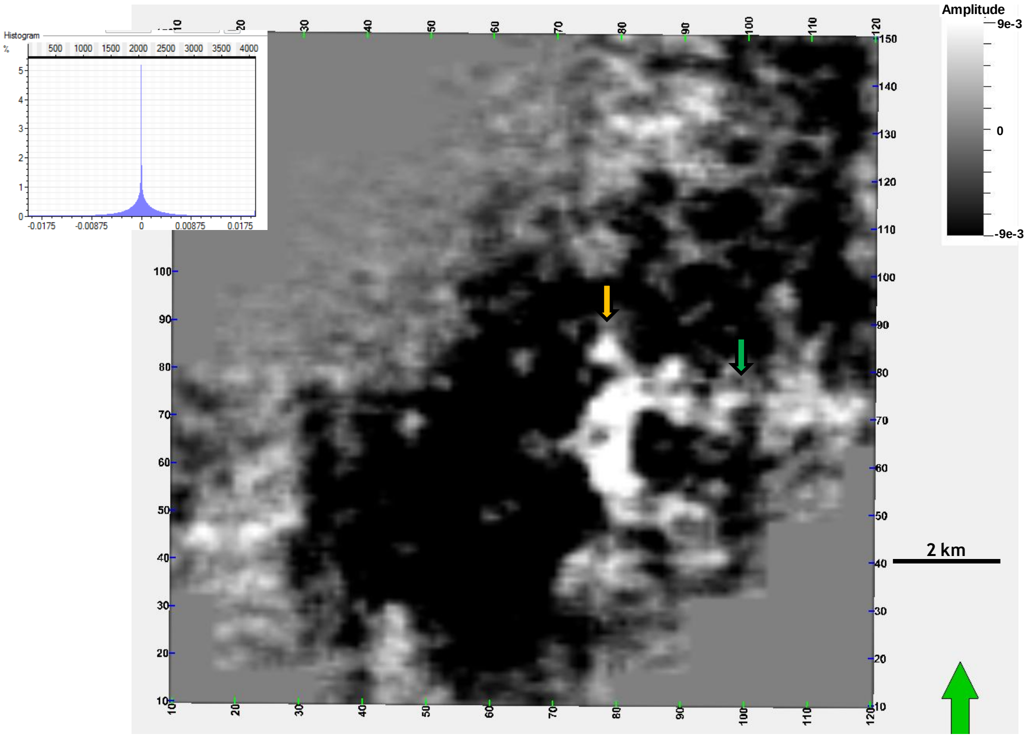

Figure III.16.- Timeslice at 850 ms of the Dickman stacked volume after one iteration of CLSM. Yellow and green arrows indicate a hypothetical crevasse splay and a flood plain, respectively.

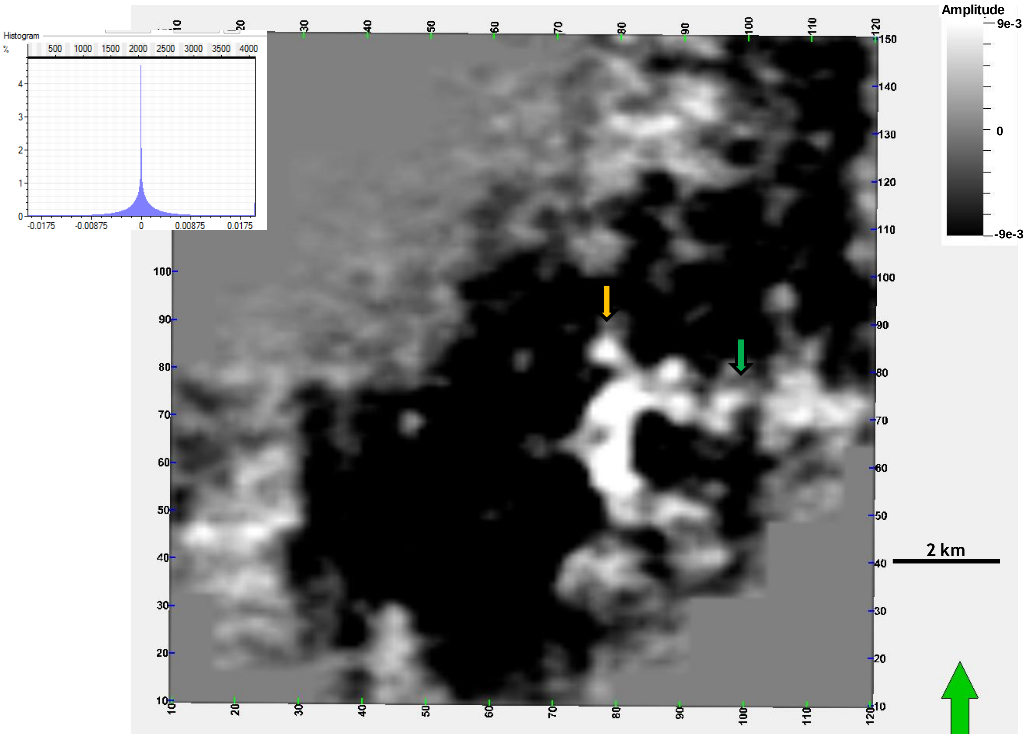

Figure III.17.- Timeslice at 850 ms of the Dickman stacked volume after two iterations of CLSM. Yellow and green arrows indicate a hypothetical crevasse splay and a flood plain, respectively.

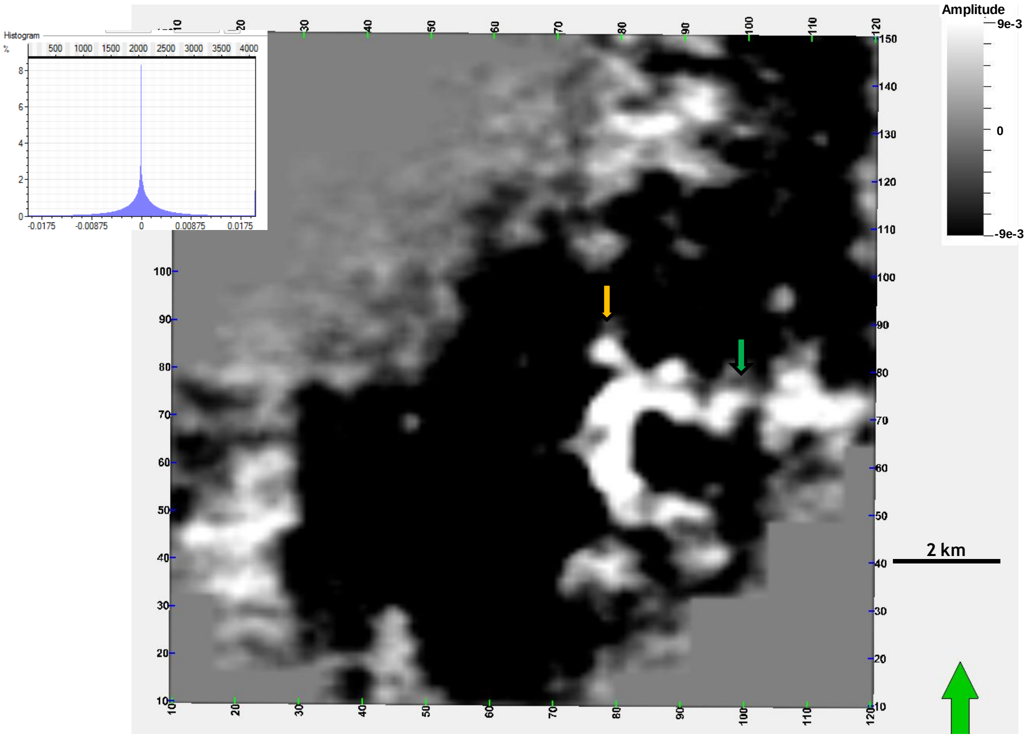

Figure III.18.- Timeslice at 850 ms of the Dickman stacked volume after three iterations of CLSM. Yellow and green arrows indicate a hypothetical crevasse splay and a flood plain, respectively.

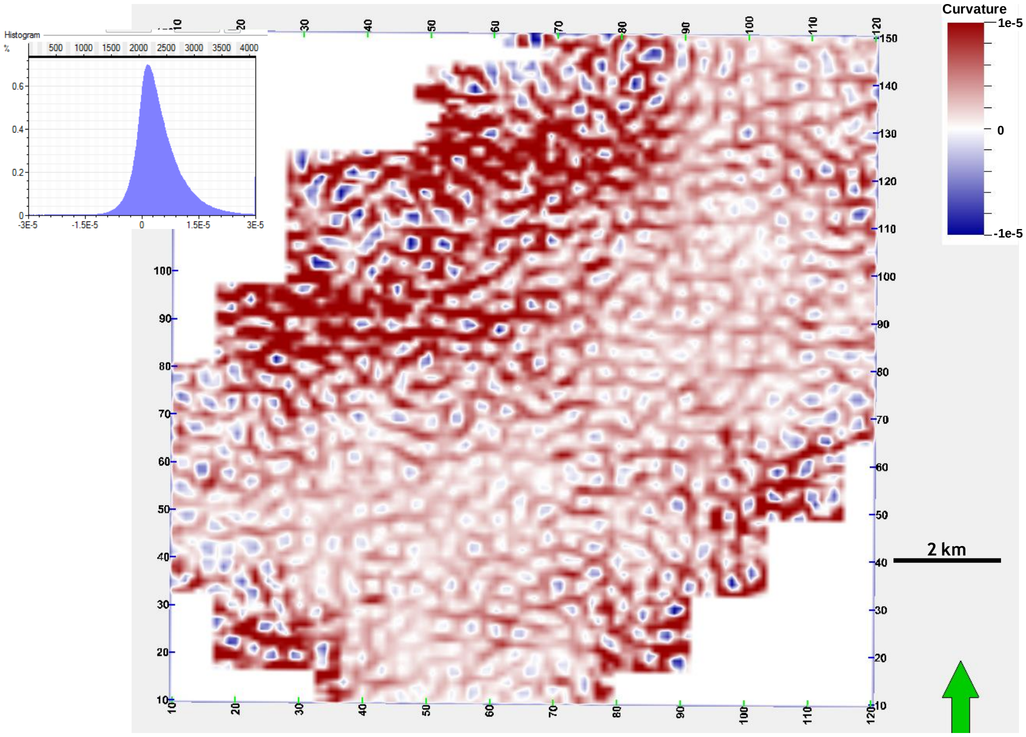

Figure III.19.- Timeslice at 750 ms showing most-positive curvature from the Dickman stacked volume after conventional migration.

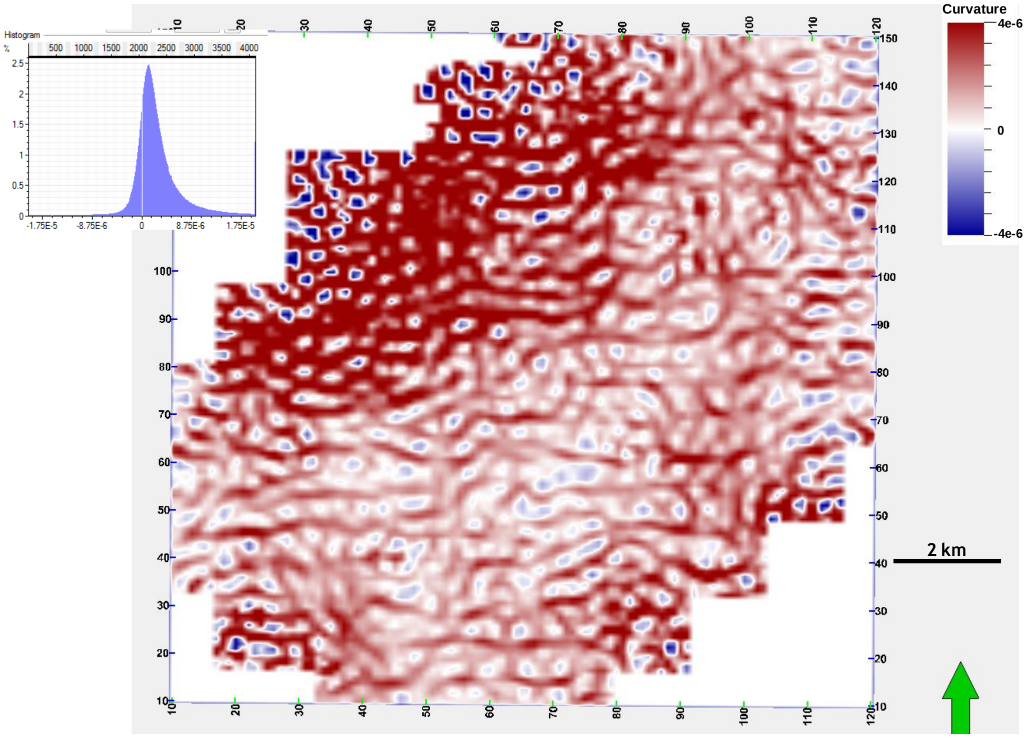

Figure III.20.- Timeslice at 750 ms showing most-positive curvature from the Dickman stacked volume after one iteration of CLSM.

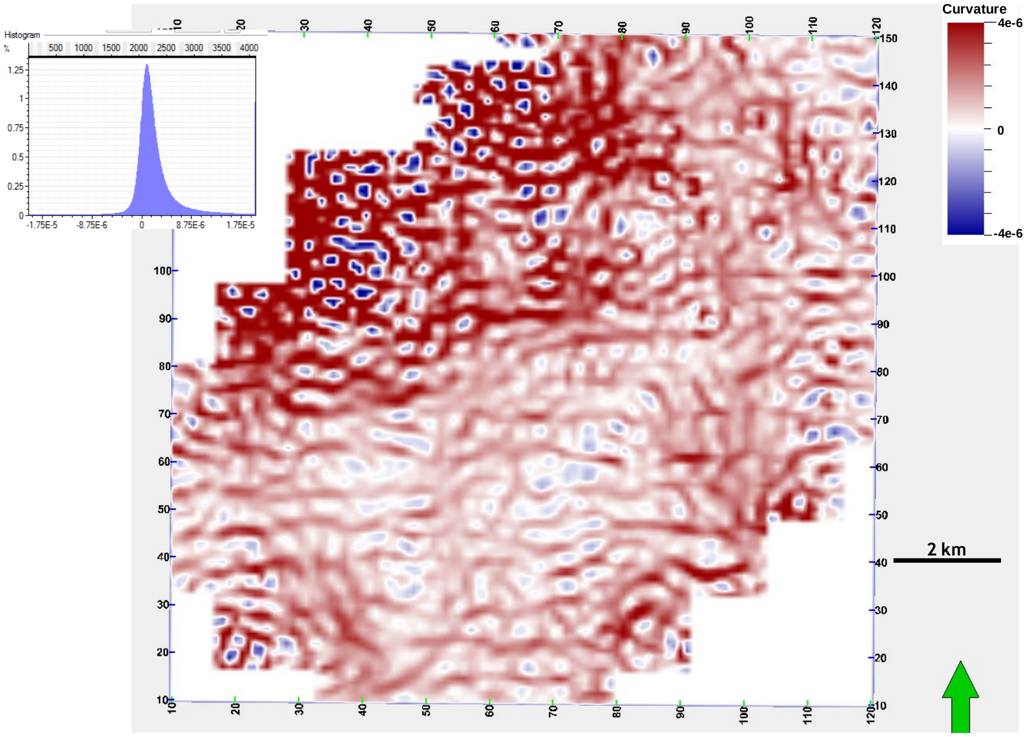

Figure III.21.- Timeslice at 750 ms showing most-positive curvature from the Dickman stacked volume after two iterations of CLSM.

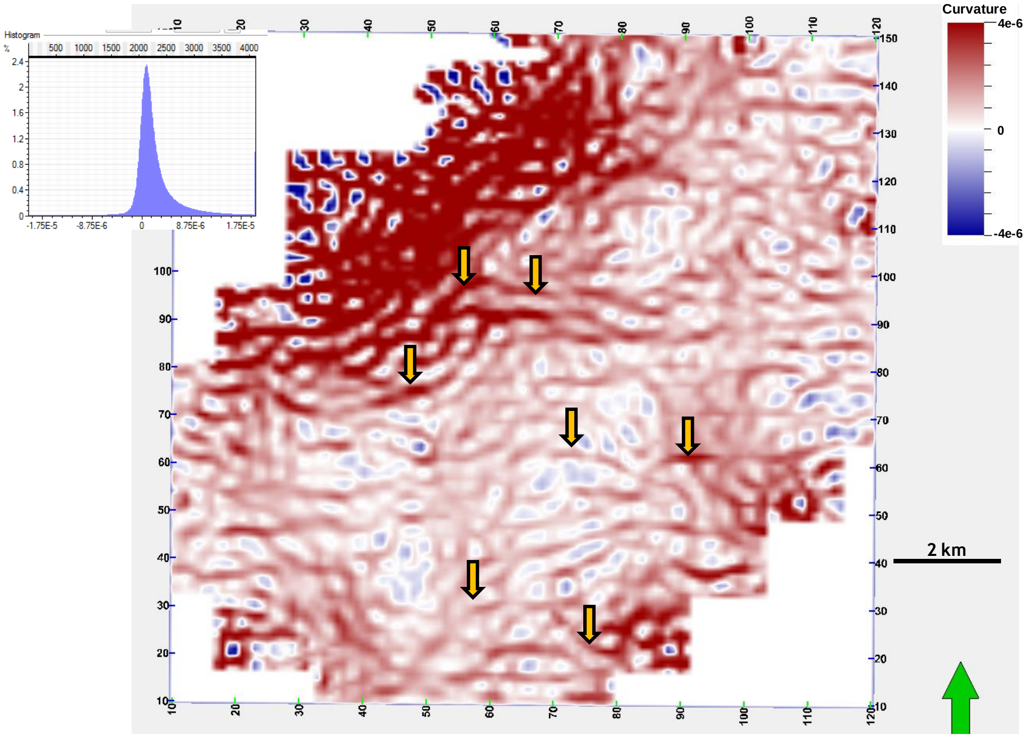

Figure III.22.- Timeslice at 750 ms showing most-positive curvature from the Dickman stacked volume after three iterations of CLSM. Yellow arrows indicate alignments that can constitute channels or faults.

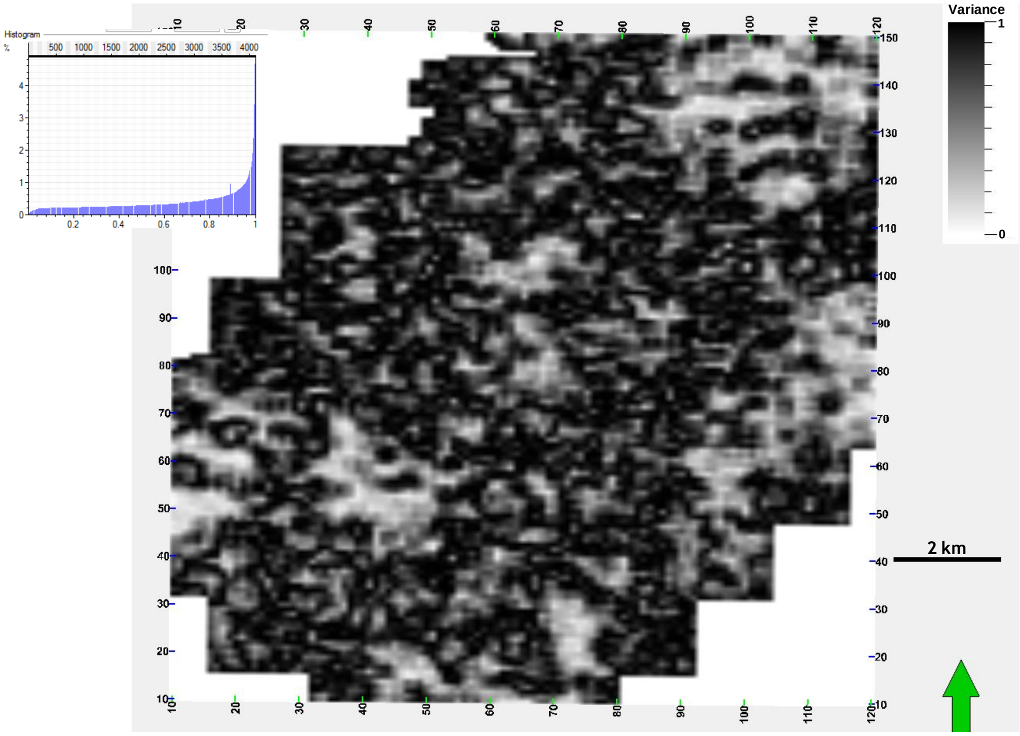

Figure III.23.- Timeslice at 750 ms of variance from the Dickman stacked volume after conventional migration.

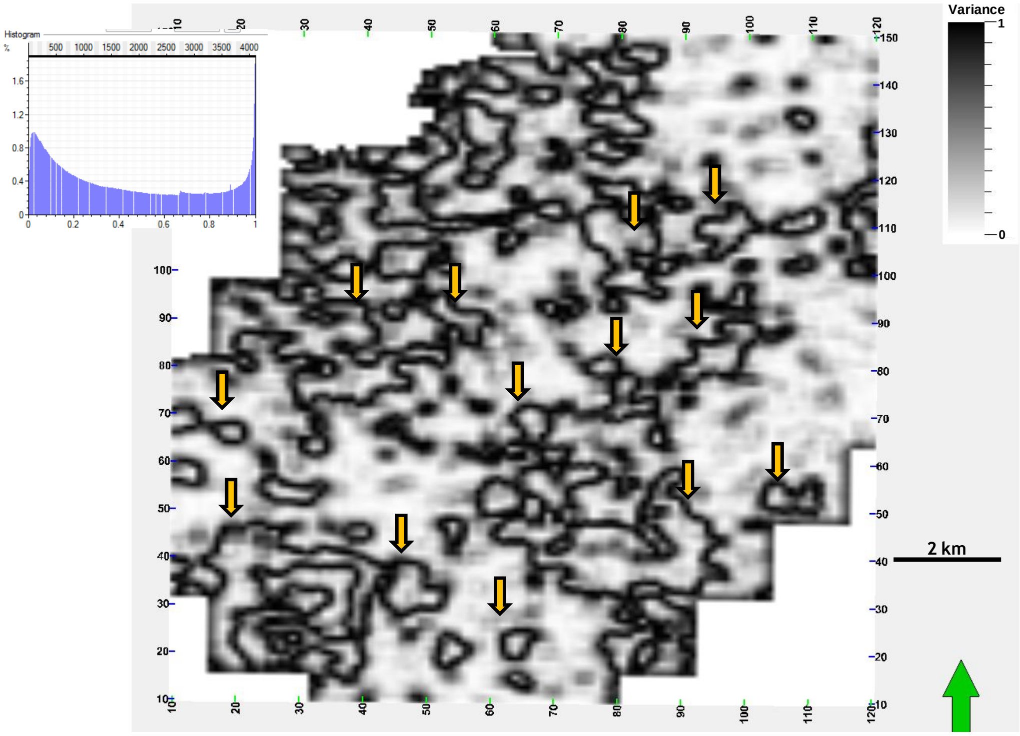

Figure III.24.- Timeslice at 750 ms of variance from the Dickman stacked volume after one iteration of CLSM. Yellow arrows indicate possible collapse/dissolution features.

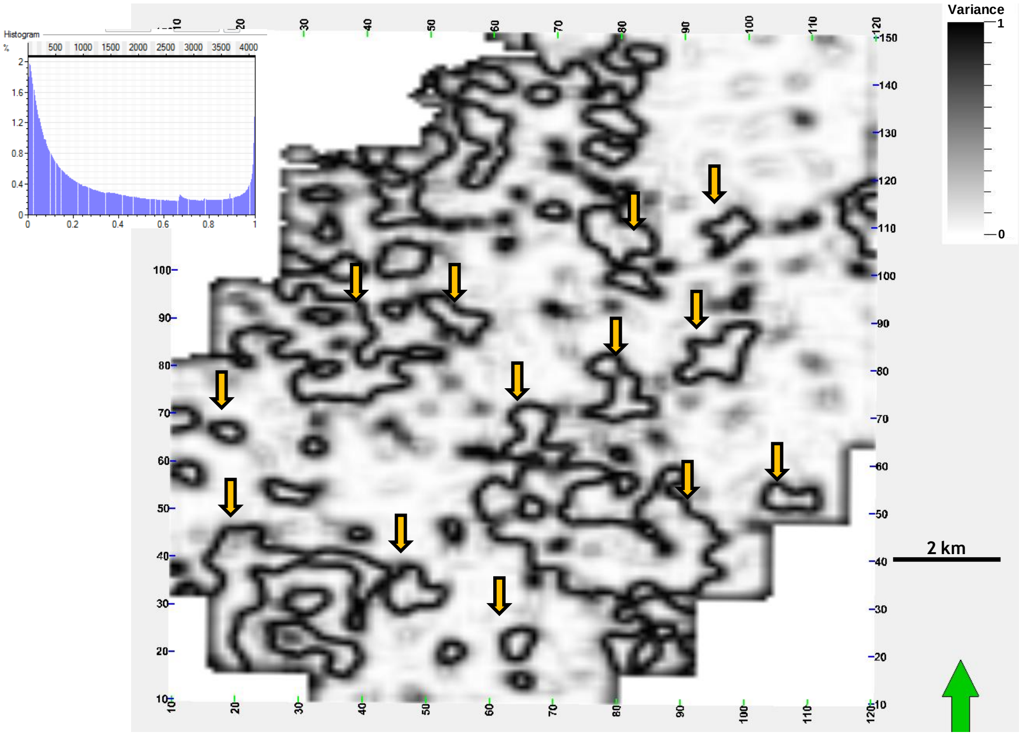

Figure III.25.- Timeslice at 750 ms of variance from the Dickman stacked volume after two iterations of CLSM. Yellow arrows indicate possible collapse/dissolution features.

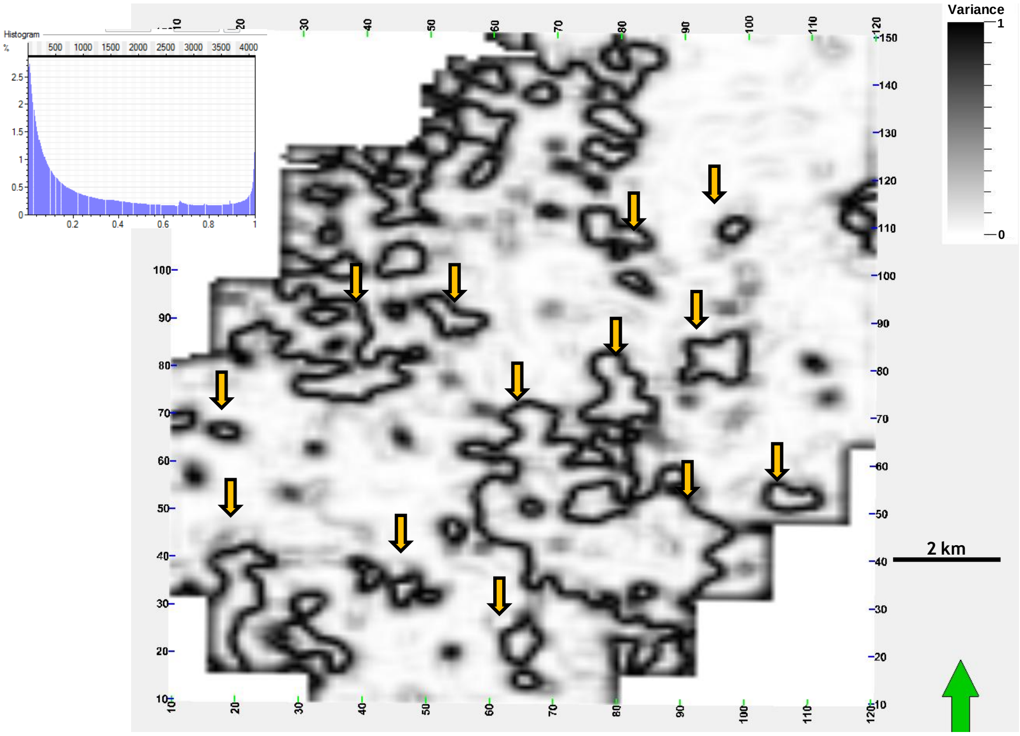

Figure III.26.- Timeslice at 750 ms of variance from the Dickman stacked volume after three iterations of CLSM. Yellow arrows indicate possible collapse/dissolution features.

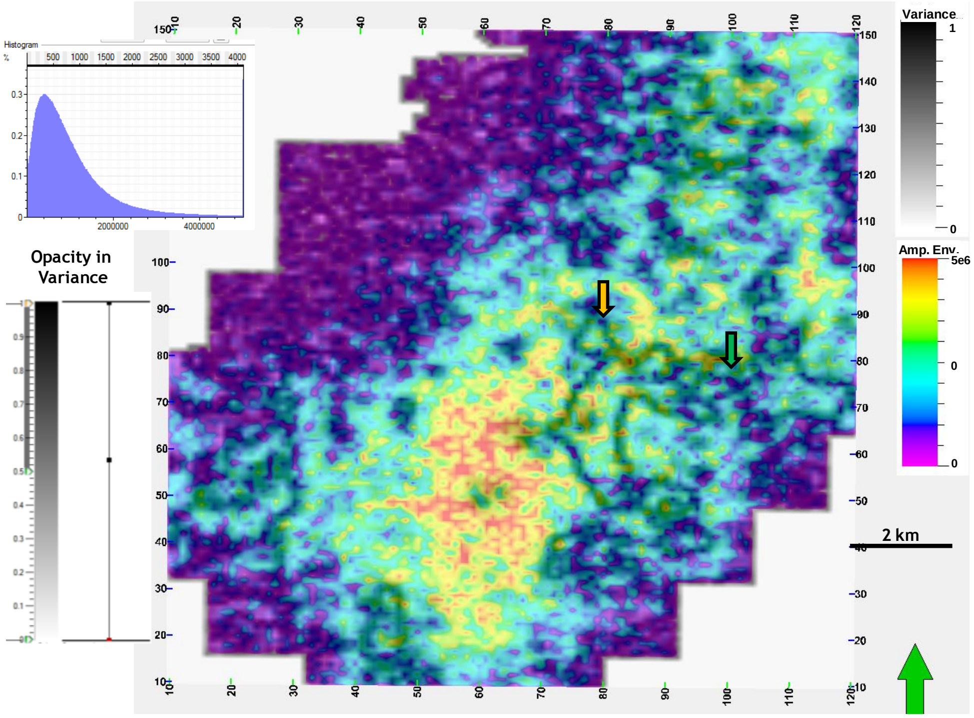

Figure III.27.- Timeslice at 850 ms of variance co-rendered with amplitude envelope from the Dickman volume after conventional migration. Yellow and green arrows indicate a hypothetical crevasse splay and a flood plain, respectively.

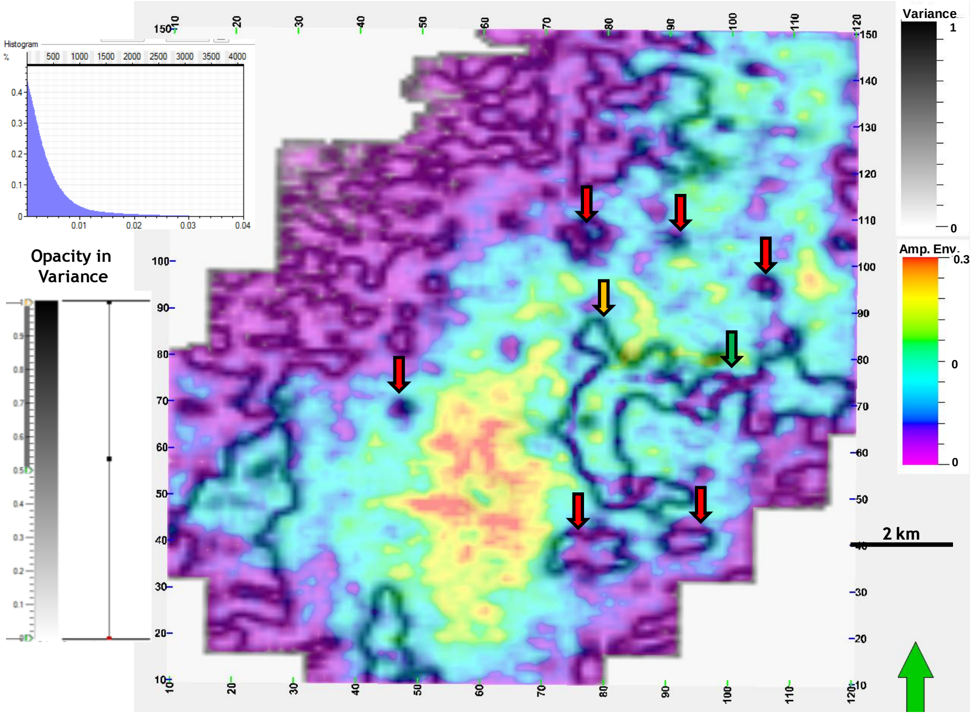

Figure III.28.- Timeslice at 850 ms of variance co-rendered with amplitude envelope from the Dickman volume after one iteration of CLSM. The yellow and the green arrows indicate a hypothetical crevasse splay and a flood plain, respectively. Red arrows indicate collapse/dissolution features.

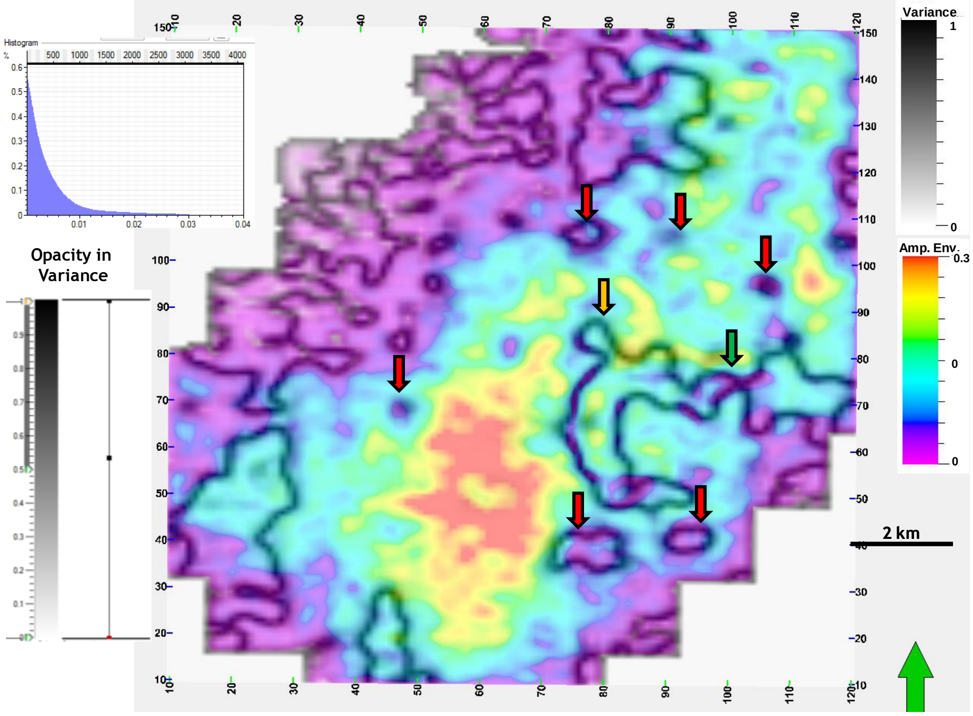

Figure III.29.- Timeslice at 850 ms of variance co-rendered with amplitude envelope from the Dickman volume after two iterations of CLSM. The yellow and the green arrows indicate a hypothetical crevasse splay and a flood plain, respectively. Red arrows indicate collapse/dissolution features.

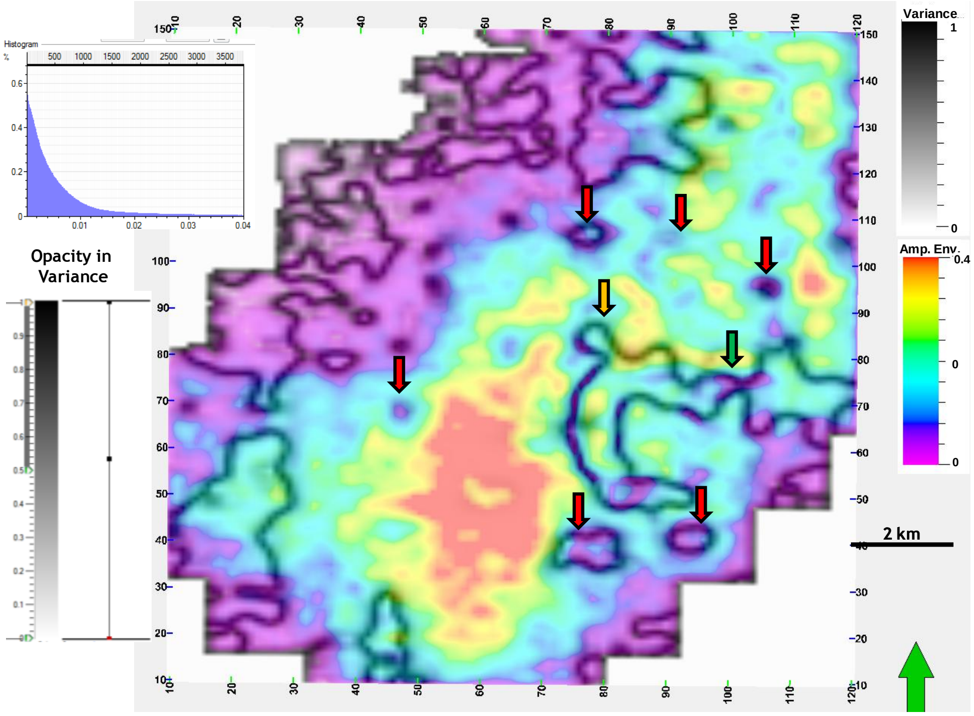

Figure III.30.- Timeslice at 850 ms of variance co-rendered with amplitude envelope from the Dickman volume after three iterations of CLSM. Yellow and green arrows indicate the crevasse splay and a flood plain, respectively. Red arrows indicate collapse/dissolution features.

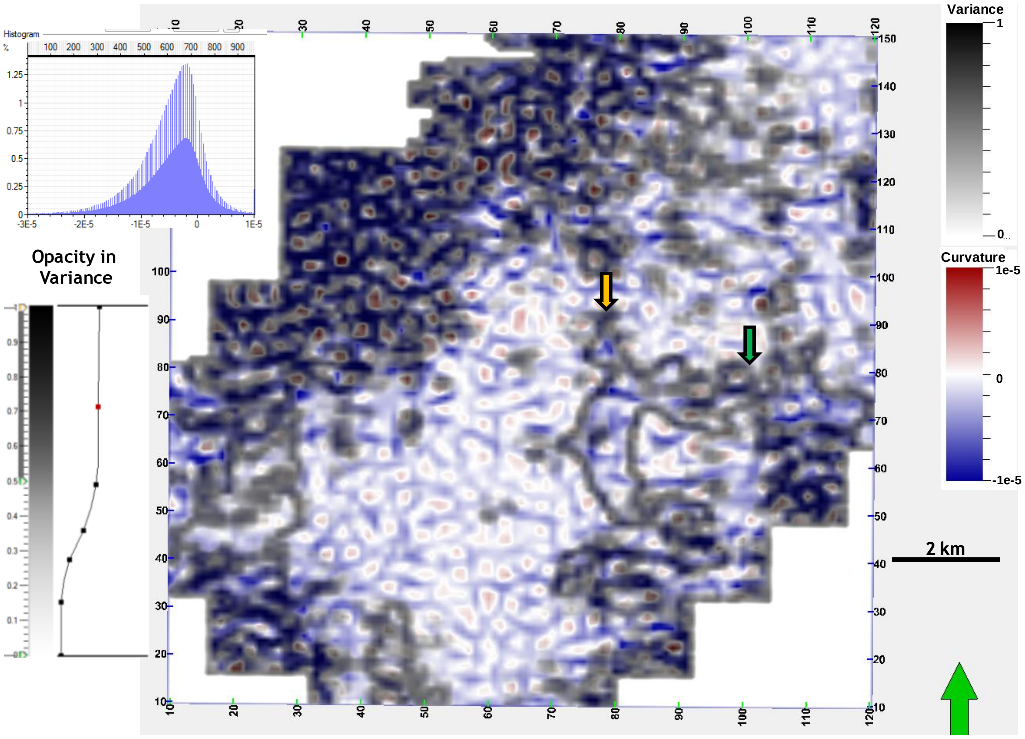

Figure III.31.- Timeslice at 850 ms of variance co-rendered with most-negative curvature from the Dickman stacked volume after conventional migration. Yellow and green arrows indicate the crevasse splay and a flood plain, respectively.

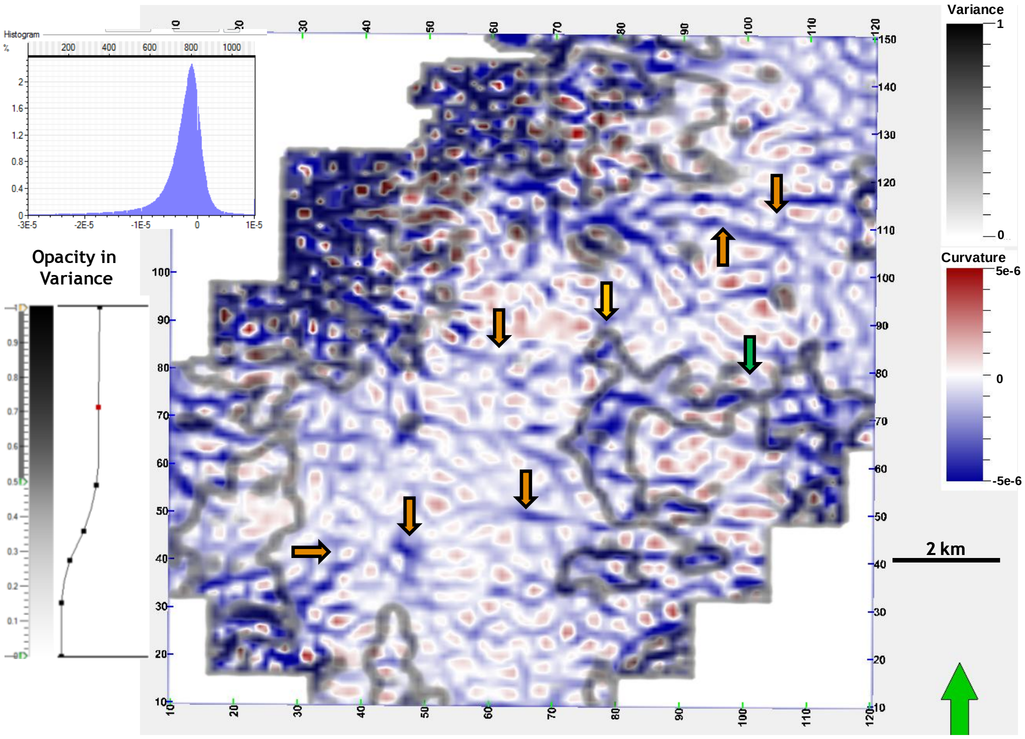

Figure III.32.- Timeslice at 850 ms of variance co-rendered with most- negative curvature from the Dickman stacked volume after one iteration of CLSM. Yellow and green arrows indicate the crevasse splay and a flood plain, respectively. Brown arrows indicate possible channels undetected by variance.

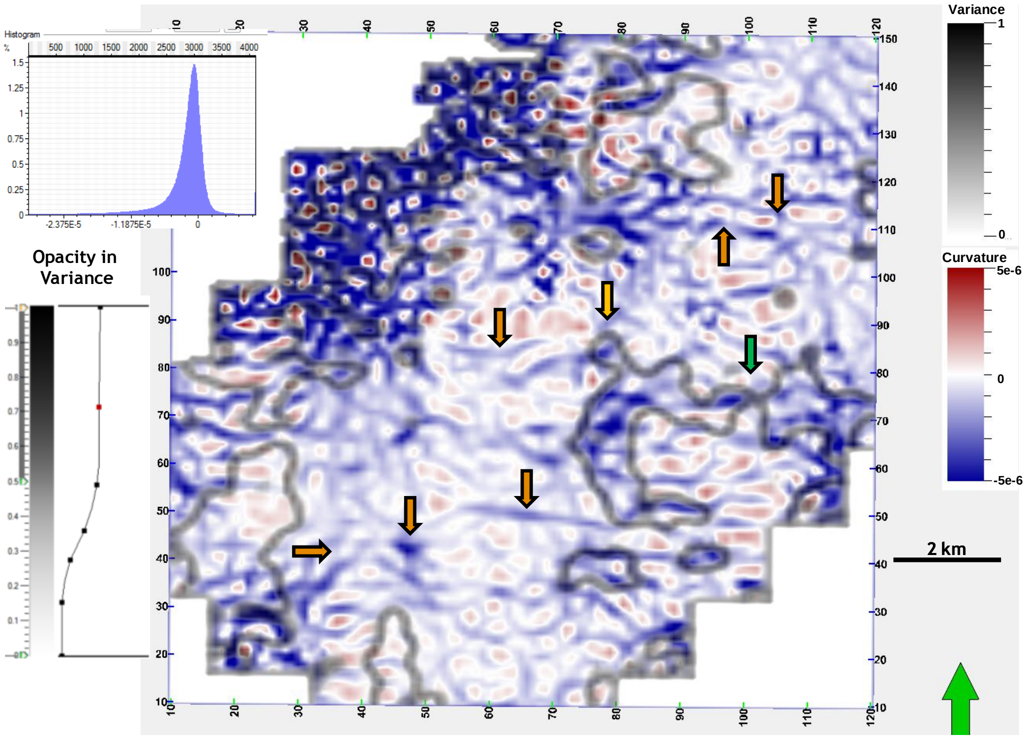

Figure III.33.- Timeslice at 850 ms of variance co-rendered with most- negative curvature from the Dickman stacked volume after two iterations of CLSM. Yellow and green arrows indicate the crevasse splay and a flood plain, respectively. Brown arrows indicate possible channels undetected by variance.

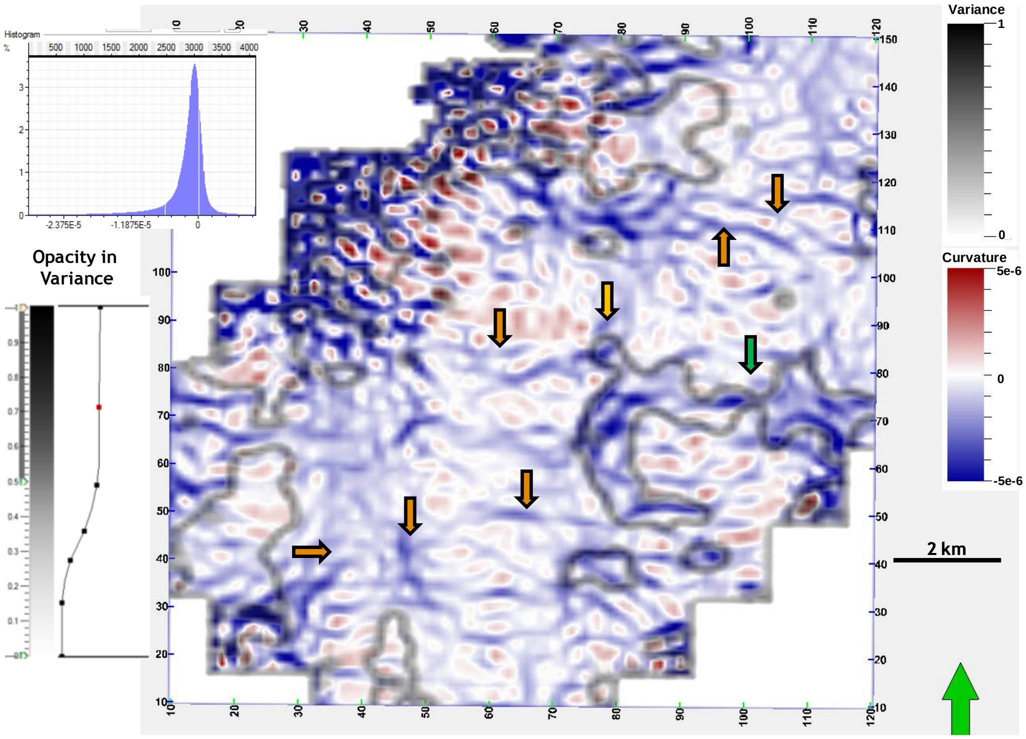

Figure III.34.- Timeslice at 850 ms of variance co-rendered with most- negative curvature from the Dickman stacked volume after three iterations of CLSM. Yellow and green arrows indicate the crevasse splay and a flood plain, respectively. Brown arrows indicate possible channels undetected by variance.

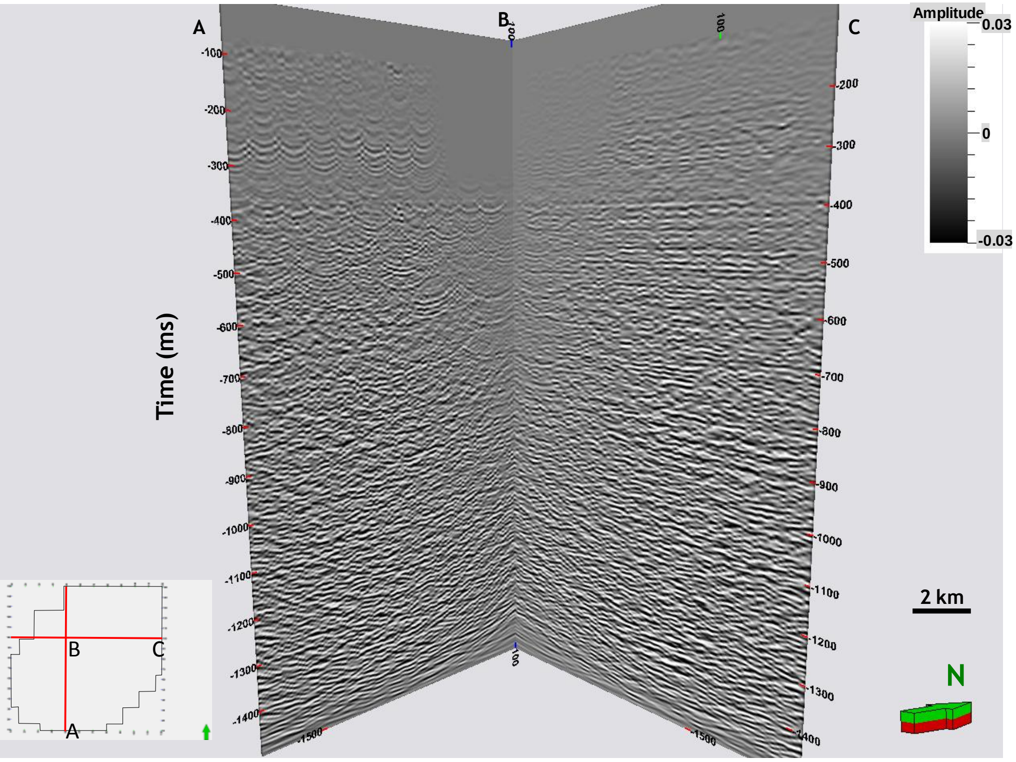

Figure III.35.- Near-offset volume (*h* = 450 ft) after unconstrained LSM.

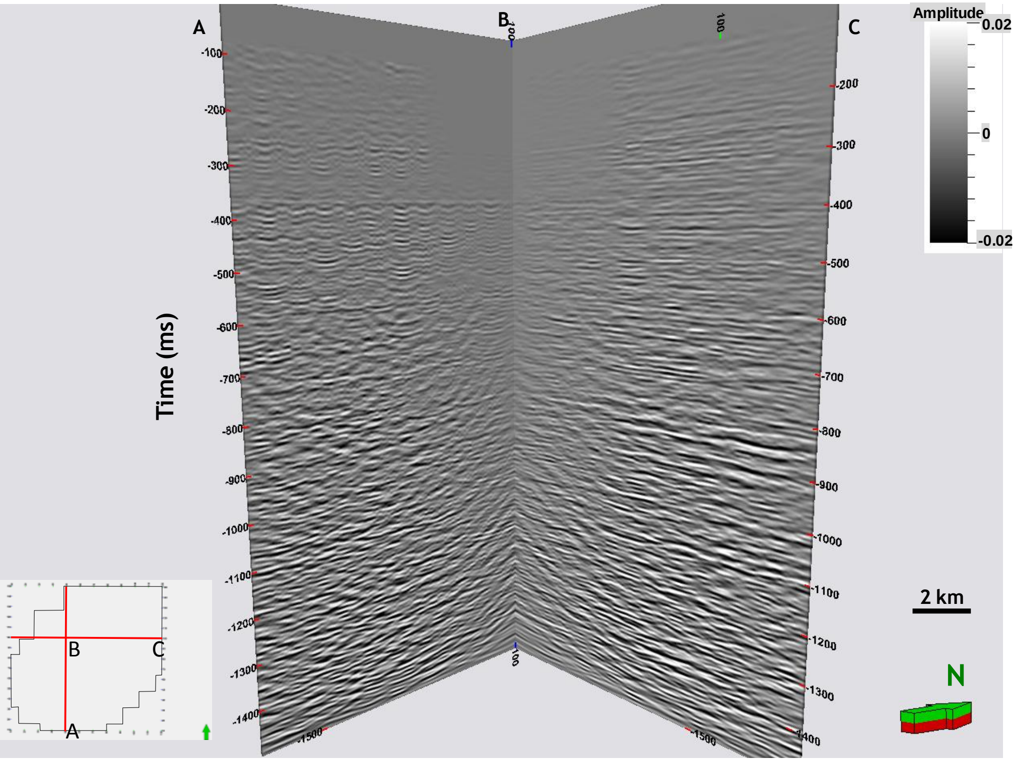

Figure III.36.- Near-offset volume (*h* = 450 ft) after constrained LSM.

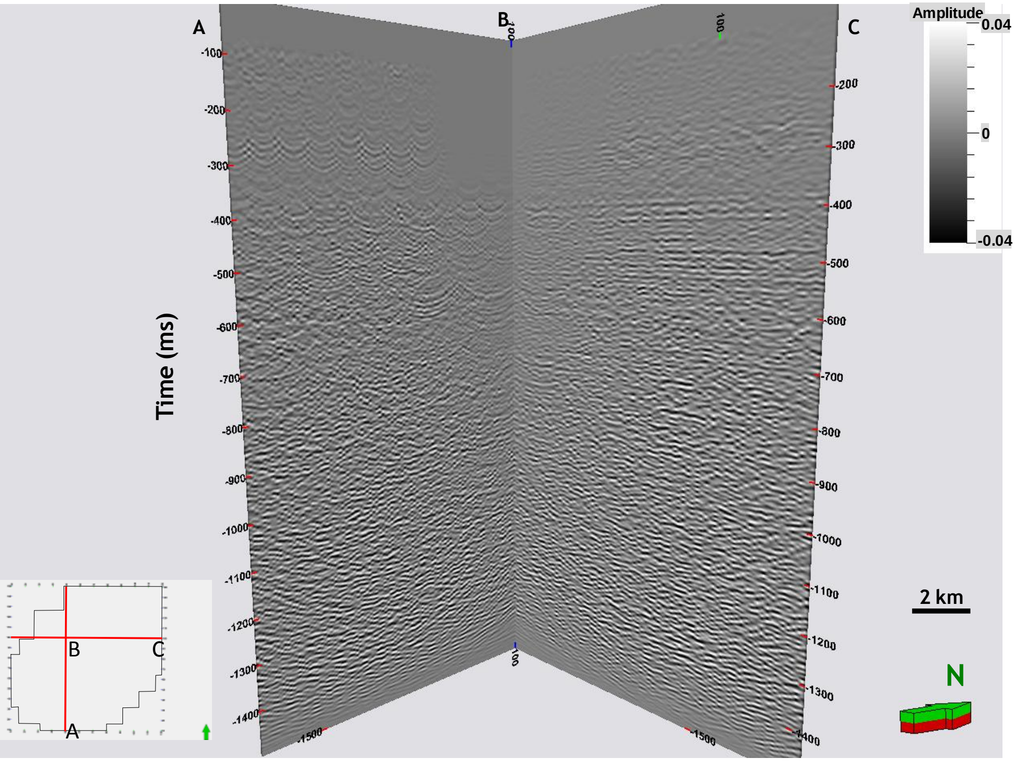

Figure III.37.- Difference between the unconstrained and constrained LSM near-offset volumes (Figures III.35 and III.36, respectively).

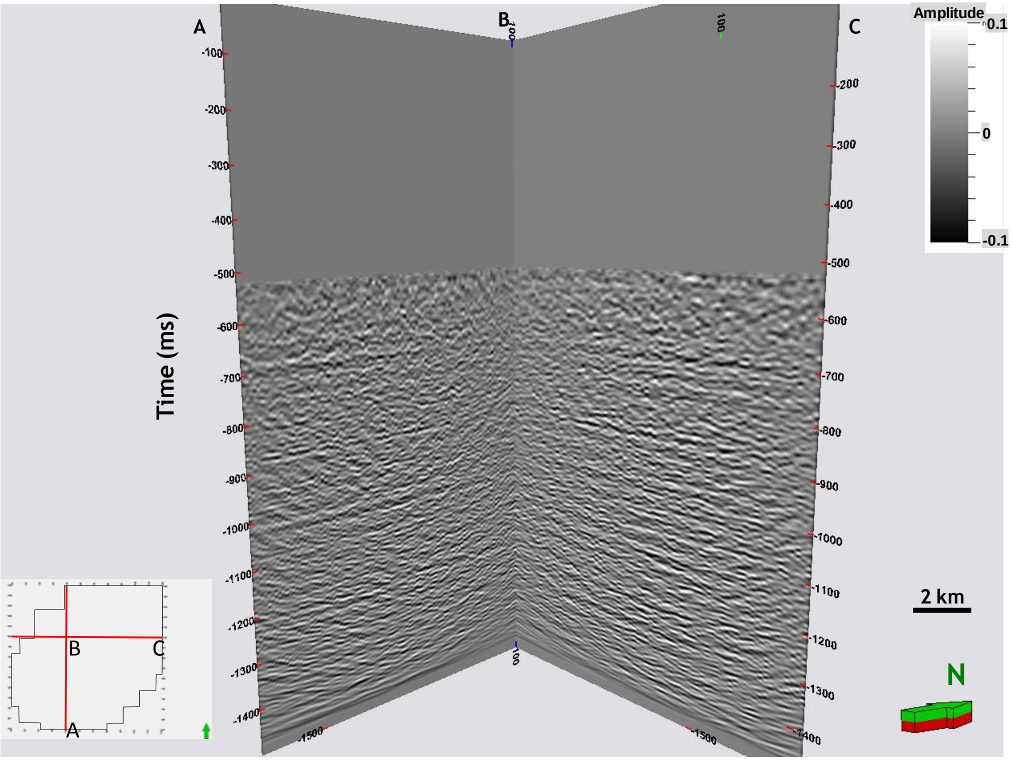

Figure III.38.- Medium-offset volume (h = 3550 ft) after unconstrained LSM.

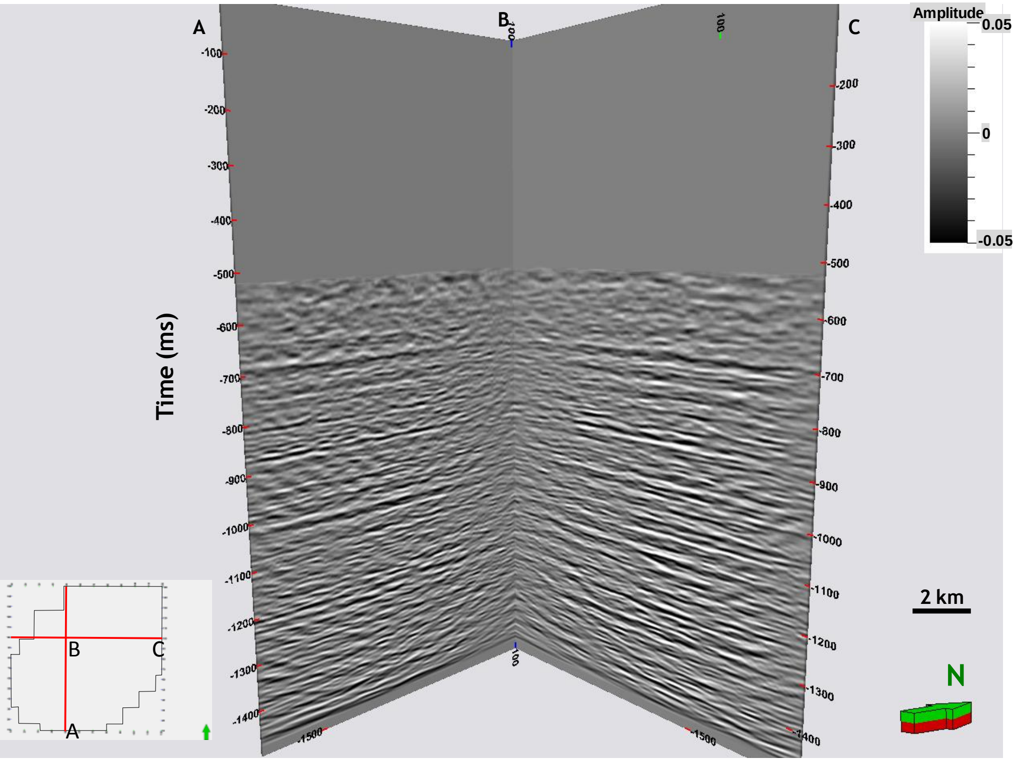

Figure III.39.- Medium-offset volume (*h* = 3550 ft) after constrained LSM.

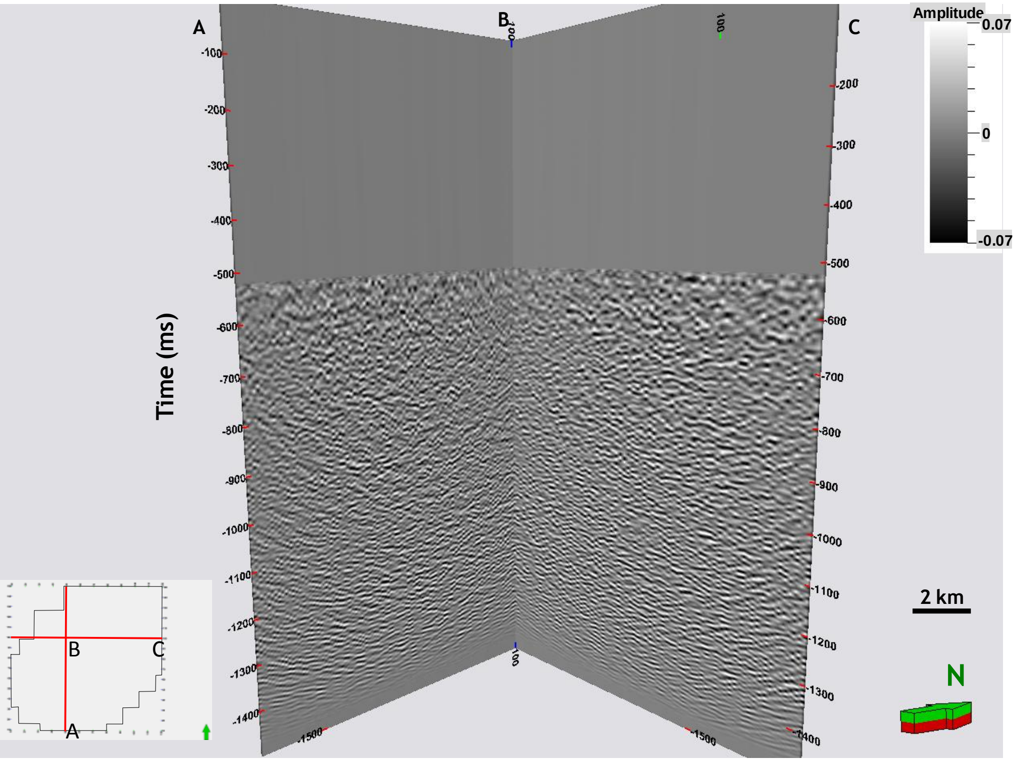

Figure III.40.- Difference between the unconstrained and constrained LSM medium-offset volumes (Figures III.38 and III.39, respectively).

CHAPTER IV

DISCUSSION AND CONCLUSIONS

By representing the consistent component of the Earth's reflectivity, constrained least-squares migration better represents the seismic amplitudes of both the migrated gathers and the corresponding stack than conventional migration. This fact is particularly important for prestack processing such as AVO, AVAZ, and elastic inversion, which strongly rely on the fidelity of the seismic amplitude. The appropriate use of a constraint function allows the attenuation of aliased artifacts, which are a product of irregular or incomplete acquisition pattern that often give rise to acquisition footprint. As a by-product, it is possible to predict missing traces in the dataset while improving the signal-to-noise ratio, which benefits processes like detailed velocity analysis. The predicted data by itself can be used as the input for depth migration. The main disadvantage of the method is the increase in computing time, because the algorithm requires one migration-demigration pair for each iteration. For this reason, preconditioning is desirable to reduce the required number of iterations. In this study, I preconditioned the data by using a tapered mute function that excludes direct waves and headwaves that cannot be predicted by Kirchhoff modeling, thus accelerating the convergence of the least-squares process and removing potential sources of instability. In contrast, the use of the constrained function can be regarded as a model preconditioning.

Application of CLSM to synthetic 2D data sets showed a significant improvement in the quality of CRP gathers from decimated input data. Unconstraint least-squares migration accurately predicts the input data but does not attenuate aliased artifacts in the migrated image. The simple median filter constraint generated spurious flat events on the common reflection point gathers. This noise constitutes a potential pitfall that can introduce random locally coherent events in the stacked sections, which otherwise are almost exactly equal to the unconstrained LSM and the conventional migration cases, demonstrating the power of the stacking process to attenuate aliasing noise.

For the three-dimensional test, I utilized the 3D Dickman survey from west Kansas to test the ability of CLSM to attenuate aliasing artifacts and deblur geologic features, using a median structure-oriented filter to play the role of the constraint function. The original shot gathers were seriously affected by aliased noise. The conventionally migrated gathers eliminate much of the properly sampled, short wavelength noise with moveout velocities smaller than those supported by the migration velocity model. However, CLSM provided the cleanest appearance, progressively improving the continuity of the reflectors and attenuating aliasing artifacts as the process was iterated. In contrast to the 2D synthetic data, stacking of conventional migration of 3D real data containing ground roll and other aliased short wavelength events results in strong acquisition footprint. In contrast, CLSM showed a noticeable reduction of the acquisition footprint pattern in both the original seismic volume and in the seismic attributes. The geologic features apparently show a trade-off between the deblurring effect of least-squares migration and the smoothing effect of the constraint function. As with any filter, an adequate selection of a "non-aggressive" constraint function seems to be vital to avoid over-smoothing the migrated events. For this reason, in the examples with the Dickman survey the second iteration yielded better balance between the attenuation of noise and the preservation of the geologic features. Finally, to test the noise-attenuation ability of the constraint function in the Dickman survey, I computed the difference between the unconstrained and the constrained LSM gathers for the first iteration in near and medium-offset volumes, showing that the sof4d median filter constitutes an adequate constraint function to remove aliased artifacts, with small tendency to remove coherent signal.

Summarizing, the main conclusions of this thesis are the following:

- CLSM can attenuate aliasing artifacts derived from irregular acquisition and incomplete data, improving the continuity of the flat events in CRP gathers.
- The methodology presented here has been applied to a very simple 3D time-migration algorithm. Significant improvements are expected with more sophisticated migration algorithms.
- In principal, the reconstructed (modeled) common shot gathers can be used to improve statics corrections (Pérez, 1997). The unmodeled component of the common shot gathers can be used to design better preprocessing filters.
- Finally, CLSM separates coherent PP signal from random noise, ground roll, head waves, shear waves and converted waves. This PP signal can serve as the starting point for diffraction imaging, whereby PP specular events are further separated from PP diffraction events (e.g., Landa et al., 2011; Moser, 2011).

APPENDICES

The following four appendices provide additional information for those not familiar with constrained least-squares migration. Appendix A summarizes the mathematical framework and computer implementation of the algorithm I have written. Appendix B is a very simple two layer tutorial example that illustrates the differences between conventional migration, unconstrained least-squares migration, and constrained least-squares migration. Appendix C applies these three algorithms to the well-documented Marmousi model, while Appendix D applies the same algorithms to the even more complicated Hess salt model. Note that all three models were generated using a finite difference solution of the scalar equation, and thus exhibit phenomena not well approximated by the Kirchhoff modeling algorithm. Furthermore, the Marmousi and Hess models both exhibit strong lateral velocity changes and were simulated using an anisotropic finite difference modeling algorithm. In contrast, the migration schemes all use a smooth background velocity model. Although my goal is to image aliased data in structurally simple geologies using 3D prestack time migration, these two structurally complex models serve to validate the robustness of the solution technique.

In this section I illustrate the performance of the CLSM algorithm on 2D synthetic seismic datasets, showing two scenarios in every model. In the first scenario I use the complete, "conventionally sampled" dataset to evaluate the performance of CLSM in attenuating mild aliasing artifacts and remodeling the original data. In the second scenario I kill two thirds of the seismic traces in every dataset to simulate a much sparser acquisition program somewhat representative of 3D irregular acquisition, which allows me to compare the performance of CLSM in attenuating severe aliasing artifacts and reconstructing the missing traces.

The first dataset corresponds to a two-layer horizontal model created using a commercial finite difference modeling software. The second dataset corresponds to the anisotropic version of the Marmousi model (Alkhalifah, 1997). The third dataset corresponds to the Hess Corporation® VIT model, available at the SEG software website. The decimation introduces aliasing artifacts that are to be suppressed by CLSM. Both the Marmousi model and the Hess model were migrated accounting for the anisotropy.

APPENDIX A: Theory and implementation of CLSM using the conjugate gradient method

Least squares formulation

Following Duquet et al. (2000), Nemeth et al. (1999), Fomel et al. (2002), among others, one can express the seismic data in terms of an earth model through the expression

$$\mathbf{d} = \mathbf{G}\mathbf{m}, \tag{A1}$$

where **d** denotes a vector of the seismic data, **m** a vector of the seismic reflectivity model (Duquet et al., 2000) and **G** is the forward modeling operator, expressed as a matrix. Theoretically, we may reconstruct **m** by pre-multiplying **d** with the inverse of **G**. Such inversion is impractical; **G** is an extremely large but highly sparse matrix, while its inverse $\mathbf{G}^{-1}$ is full. Instead, we preserve this sparseness by using the *adjoint* operator (Claerbout, 2009)

$$\mathbf{m}' = \mathbf{G}^T\mathbf{d}, \qquad \text{(A2)}$$

where $\mathbf{G}^T$ constitutes the adjoint of **G**, and **m'** represents an estimation of the real reflectivity model **m**. Equation A2 is an expression for conventional migration.

In spite of its usefulness, equation A2 has some flaws associated with the fact that $\mathbf{G}^T$ only approximates the inverse of the modeling operator. If I substitute equation A1 into equation A2, I obtain

$$\mathbf{m}' = \mathbf{G}^T\mathbf{G}\mathbf{m}, \qquad \text{(A3)}$$

where I note that the operator $\mathbf{G}^T\mathbf{G}$ is symmetrical whether **G** is symmetrical or not.

Observe that as our estimator **m'** approaches our reflectivity model **m**, the Hessian matrix $\mathbf{G}^T\mathbf{G}$ approaches the identity matrix, or alternately, $\mathbf{G}^T$ approaches the inverse of the modeling operator. Nemeth (1996) recognized that one key requirement for this approximation to the inverse to occur is a dense source-receiver acquisition program that avoids gaps in the surface coverage. Since such a dense acquisition is rarely met because of both practical and economic reasons, the matrix $\mathbf{G}^T\mathbf{G}$ usually differs considerably from the identity matrix. Such differences introduce migration artifacts as well as acquisition footprint into the migrated image (Schuster, 1997; Nemeth, 1996). The goal of CLSM is to attenuate those undesirable artifacts by augmenting the matrix $\mathbf{G}^T\mathbf{G}$ with constraints to make it more diagonally dominant, where the constraints favor solutions that are geologically reasonable and penalize solutions associated with aliasing and imaging of coherent seismic noise.

Following Schuster (1997), my goal is to minimize the misfit function

$$\varepsilon = ||\mathbf{Gm} - \mathbf{d}||^2 + ||\mathbf{Cm}||^2, \qquad \text{(A4)}$$

where $\mathbf{C}$ is a constraint matrix. The expression that minimizes equation A4 is (Schuster, 1997)

$$[\mathbf{G}^T\mathbf{G} + \mathbf{C}]\mathbf{m} = \mathbf{G}^T\mathbf{d}. \tag{A5}$$

Equation A5 constitutes a simplified expression where one assumes that the *a priori* model, $\mathbf{m}_0$, is zero.

Tarantola (2005) derives expressions equivalent to equation A5 where he defines $\mathbf{C}$ to be the inverse of the covariance matrix in the model space. He also includes a covariance matrix of the seismic measurements. If one can estimate these two covariance matrices, one can balance the fit to the data with the fit to the *a priori* model. In practice, any operator that makes the data look smooth constitutes a constraint operator. In the two-dimensional examples of this Appendix, I utilize a simple five-point median filter as a constraint function, except in the Hess salt model, where I obtained better results using a three-point median filter.

Direct implementation of equation A5 is impractical and expensive, as it would imply the calculation of the inverse of the huge $\mathbf{G}^T\mathbf{G}+\mathbf{C}$ matrix. Instead, I implement the CLSM method using the conjugate gradient algorithm where Kirchhoff migration plays the role of $\mathbf{G}^T$, the adjoint operator, and the corresponding demigration algorithm plays the role of $\mathbf{G}$, or the forward Kirchhoff modeling operator. The added advantage of an iterative solution is that it is simple to apply any desired constraint (such as Radon filters or structure-oriented filters into the workflow). Furthermore, these filters do not need to be linear differential operators, thus allowing the use of median and other robust filters.

Constrained least-squares migration using the conjugate gradient method

In order not to bias my result I follow Nemeth et al. (1999) and set my initial model (at iteration 0) to be

$$\mathbf{m}_0 = \mathbf{0}. \tag{A6}$$

To update this model, I first use the Gram-Schimdt orthogonalization process to generate a set of orthogonal vectors $\mathbf{h_i}$, given the $\mathbf{g_i}$ linear independent vectors (Jovanovic, 2004), called the conjugate direction vectors and the regularized gradient vectors (Nemeth, 1996), respectively:

$$\mathbf{h}_{\boldsymbol{i}} = \mathbf{g}_i + \sum_{\boldsymbol{k=0}}^{\boldsymbol{i-1}} \beta_k^i \mathbf{h}_k, \tag{A7}$$

with $\mathbf{h_0} = \mathbf{g_0}$. The first gradient vector $\mathbf{g_0}$, is given by the migration of the residual vector, defined as

$$\mathbf{r}_0 = \mathbf{d}_0 - \mathbf{Gm_0}, \tag{A8}$$

where $\mathbf{d_0}$ constitutes the data. Since my initial model $\mathbf{m_0} = \mathbf{0}$, $\mathbf{r_0} = \mathbf{d_0}$. Hence, the first linear independent vector is given by

$$\mathbf{g}_0 = \mathbf{G}^T \mathbf{d}_0, \tag{A9}$$

which constitutes the conventionally migrated data, or the 0th iteration.

With these elements I update our model using the expression (Fomel et al., 2002)

$$\mathbf{m}_{\boldsymbol{i+1}} = \mathbf{m}_{\boldsymbol{i}} + \alpha_i \mathbf{h}_i, \tag{A10}$$

as well as the residual vector

$$\mathbf{r}_{\boldsymbol{i+1}} = \mathbf{r}_{\boldsymbol{i}} - \alpha_i \mathbf{G}\mathbf{h}_i, \tag{A11}$$

which allows me in turn to update the gradient vectors

$$\mathbf{g}_{i+1} = \mathbf{G}^T \mathbf{r}_{i+1}. \tag{A12}$$

According to Hestenes (1973), for the case where **G** is a non-negative Hermitian matrix, the optimum values of the factors α and β are given by

$$\alpha_i = \frac{\langle \mathbf{g}_{i,} \mathbf{g}_i \rangle}{\langle \mathbf{G}\mathbf{h}_{i,} \mathbf{G}\mathbf{h}_{i,} \rangle}, \text{ and} \tag{A13}$$

$$\beta_i = \frac{\langle \mathbf{g}_{i+1,} \mathbf{g}_{i+1} \rangle}{\langle \mathbf{g}_{i,} \mathbf{g}_i \rangle}, \tag{A14}$$

where the brackets <,> denote the inner product of the two vectors.

Up to this point I have shown the equations that define least-squares migration using the CGM *without* the constraint function. Defining a filtering operator, *F* (such as my five-point median filter), I apply it in the updated model vector in equation A7 to obtain

$$\bar{\mathbf{m}}_{i+1} = F(\bar{\mathbf{m}}_{\boldsymbol{i}} + \alpha_{\boldsymbol{i}} \boldsymbol{h}_{\boldsymbol{i}}), \tag{A15}$$

and

$$\bar{\mathbf{h}}_{\boldsymbol{i}} = \frac{\bar{\mathbf{m}}_{i+1} - \bar{\mathbf{m}}_i}{\alpha_i}. \tag{A16}$$

Substituting equation A16 into equations A11 and A13 I obtain the constrained version of the least-squares migration.

I will use the difference between the new and the previous models (from here on referred to as the "model difference")

$$\|\boldsymbol{\delta}\mathbf{m}_i\| = \|\bar{\mathbf{m}}_{i+1} - \bar{\mathbf{m}}_i\|, \qquad \text{(A17)}$$

as well as the difference between the predicted data and the original data (from here on referred to as the "data difference")

$$\|\boldsymbol{\delta}\mathbf{d}_i\| = \|\mathbf{G}\bar{\mathbf{m}}_{i+1} - \mathbf{d}_0\|, \qquad \text{(A18)}$$

as well as the modulus of the residual vector $\|\mathbf{r}\|$ and the modulus of the gradient vector $\|\mathbf{g}\|$, to monitor the convergence of CLSM.

Preconditioning the data: Weighting factors

Preconditioning the data is performed by using a function that excludes events inconsistent with Kirchhoff modeling such as direct waves, head waves, and other events that are not reflected or diffracted. I define a linear mute whose slope in the offset domain is just enough to exclude the undesirable events, and taper it using a raised cosine tapering function. For real vs. synthetic data, one would simply apply standard processor-define mutes stored in the trace headers after each iteration. To account for spherical divergence I multiply the mute function by the gain factor t^n, where n usually varies between 1.2 and 1.4, obtaining the following weighting function

$$W(t,h) = \begin{cases} t^n, \text{if } s \geq t/h \\ 0\ , \text{elsewhere} \end{cases} \quad , \qquad \text{(A19)}$$

where s is the slope of the mute region, t is the time, h is the source-receiver offset and W is the weighting function, which must not be confused with the weighting coefficients used to correct the amplitudes in migration and demigration.

This weighting function is incorporated in the least-squares migration framework by expressing the misfit function in equation A4 as

$$\varepsilon = \left|\left|\mathbf{W}(\mathbf{Gm} - \mathbf{d})\right|\right|^2 = [\mathbf{W}(\mathbf{Gm} - \mathbf{d})]^T[\mathbf{W}(\mathbf{Gm} - \mathbf{d})]. \quad \text{(A20)}$$

W is simply a diagonal matrix that applies the mute function to the data vector and the modeled data from the reflectivity. Taking the first derivative of equation A20 with respect to each model parameters, $\mathbf{m}_k$, and setting the result to zero gives

$$[\mathbf{G}^T\mathbf{W}^T\mathbf{W}\mathbf{G}]\mathbf{m} = \mathbf{G}^T\mathbf{W}^T\mathbf{W}\mathbf{d}, \quad \text{(A21)}$$

which following Nemeth (1996) can be expressed as

$$\left[\underline{\mathbf{G}}^T\underline{\mathbf{G}}\right]\mathbf{m} = \underline{\mathbf{G}}^T\underline{\mathbf{d}}, \quad \text{(A22)}$$

where $\underline{\mathbf{d}} = \mathbf{Wd}$, $\underline{\mathbf{G}} = \mathbf{WG}$, and $\underline{\mathbf{G}}^T = \mathbf{G}^T\mathbf{W}^T$. Thus, equation A22 has the same form as equation A4, which means that can be solved with the same conjugate gradient method. The matrices **G**, $\mathbf{G}^T$ and **C**, are not explicitly calculated. Instead, we apply the migration and demigration operators and the weighting function in the appropriate order. It is important to note that the objective of the muting is not to zero the undesirable events, but rather to disregard this prediction their prediction in the CLSM solution, thereby avoiding Gibb's phenomena at mute edges.

Flowcharts and implementation in Fortran 2003

Figure A1 shows a detailed flowchart that summarizes the CLSM using the conjugate gradient method.

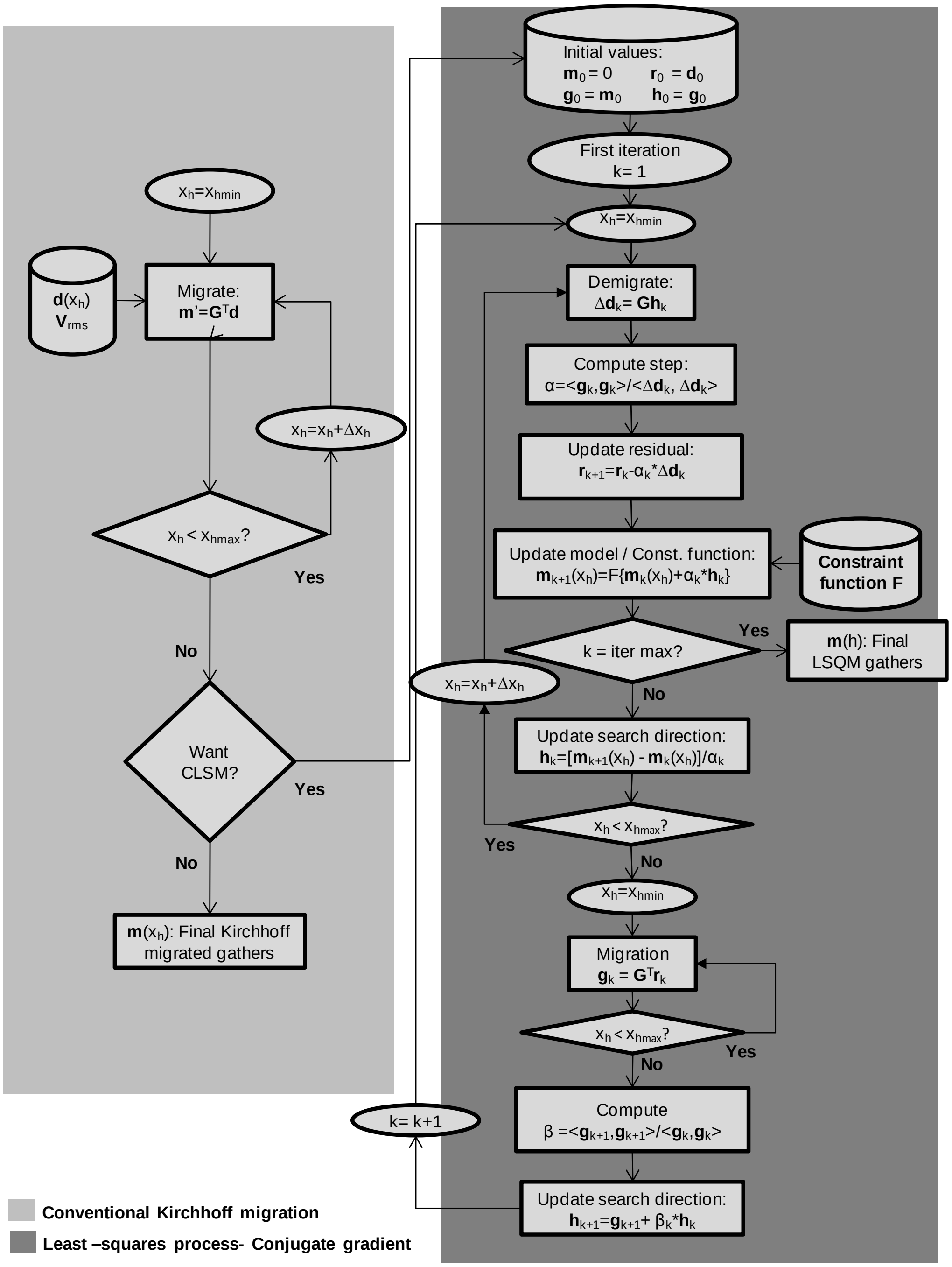

Figure A1.- Flowchart of the constrained least-squares migration algorithm using the conjugate gradient method.

The algorithm discussed above was implemented in Fortran 2003. It was split into several subroutines linked to the main program that supplies the prestack shot gathers and velocity model, and produces common offset migrated gathers. The 3D version of the software was split into several programs, as described in Chapter III and the Appendix E, economizing RAM by saving temporary files in the hard disc.

In the following list I summarize the main programs and briefly describe its function.

PROGRAM	DESCRIPTION
alexmig3d_1st_mig	"First" migration program. It obtains calculates the gradient **g**, if LSM is chosen, otherwise it performs conventional Kirchhoff migration.
alexmig3d_1st_dem	Demigration program. It calculates the vector $\Delta\mathbf{d}$ by demigrating the search direction **h**, which is used to obtain α and update the residual.
alexmig3d_2nd_mig	"Second" migration program. It updates the gradient **g** by migrating the updated residual, and the search direction **h** using equation A7.
stack	AASPI stacking utility, utilized to stack the modeled gathers **m** before the application of the constraint function.
dip3d	AASPI utility used to calculate the inline and crossline dip components, required by the sof4d program.
sof4d	AASPI utility used to implement the constraint function through the structure-oriented filter. One can choose among mean filter, median filter and principal component filter.
update_h	This program updates the search direction **h** using equation A16, when the constraint function is used.
alexmute	This program applies a mute to the modeled gathers **m** after the constraint function, to zero any numerical artifact produced by the sof4d program in the muted zone.
alexsorting	Sort the data from common-offset to common reflection point gathers.
alexresorting	Sort the data from common reflection point to common-offset gathers.

Figure A2 shows the flowchart of the interaction between the Fortran 2003 programs of Table I, which is implemented in the script shell. Secondary programs implemented as subroutines (e.g., fast Fourier transform, half derivative and its adjoint, etc.) are not shown explicitly. To speed up the process I used OpenMP to parallelize the migration and demigration loops. When the data becomes too large respect to the available RAM, the program can work the whole process with blocks of data according to offset intervals. Another step to further reducing computing time is the parallelization of the blocks using MPI. While not still implemented in the 2D version of CLSM, MPI has been used in the more compute intensive 3D version, as explained in Chapter III.

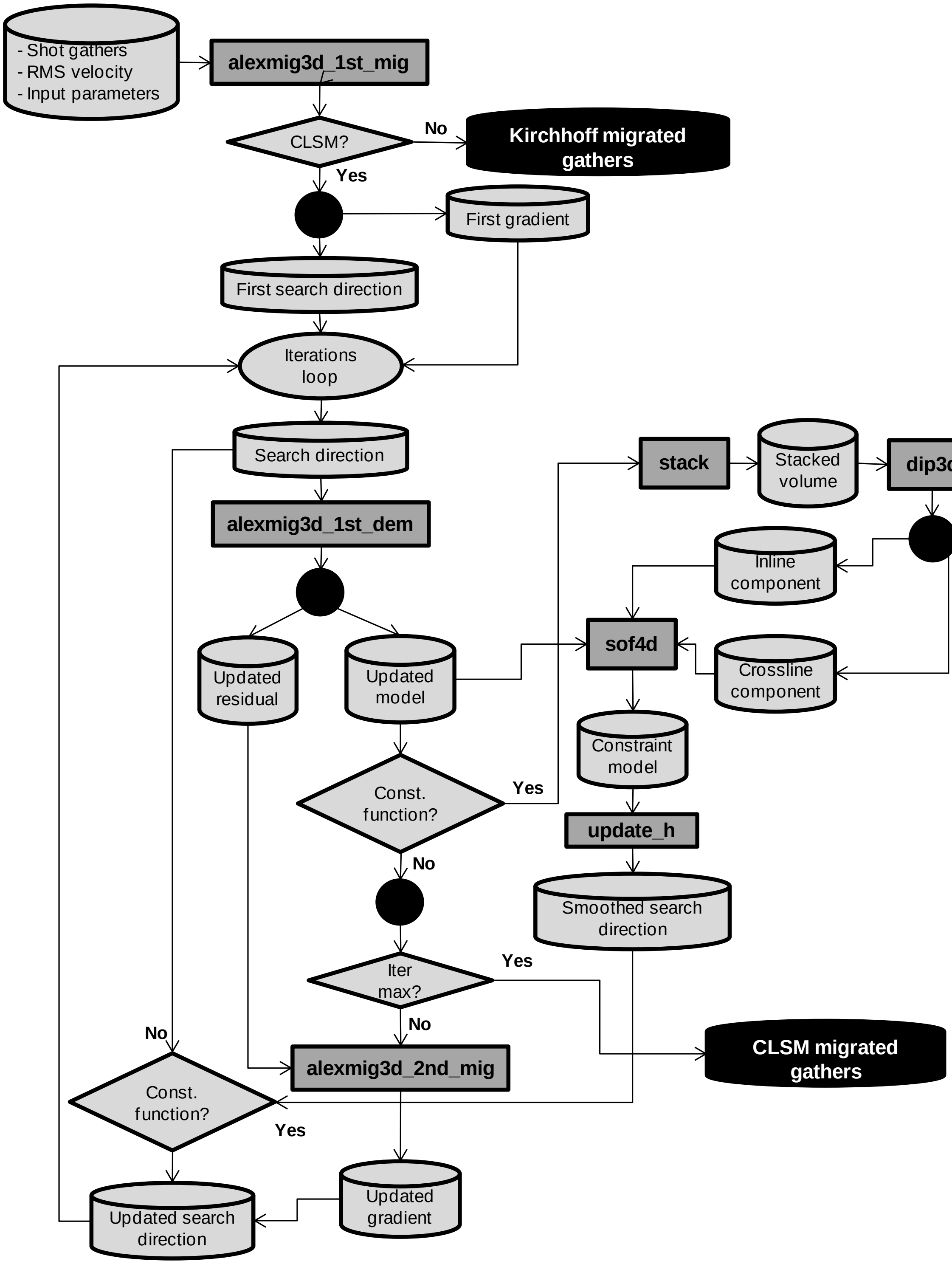

Figure A2.- Flowchart of the Fortran 2003 main programs that perform 3D constrained least-squares migration using the conjugate gradient method.

APPENDIX B: Two-layer horizontal model

Densely sampled input data

The synthetic data of the two-layer model consist of 45 shot gathers spaced 200 m apart, with 154 receivers along the section spaced 60 m apart, for a total of 6930 traces with time sampling of 4 ms and 3 s of time recording. The velocity model (and finite difference computation grid) consists of 232 vertical samples and 736 horizontal samples, with spacings of 12.5 m in both dimensions.

Figure B1 shows the velocity model and Figure B2 shows a detail of the undecimated dataset. Figures B3-B5 show the predicted data after conventional migration, unconstrained LSM and constrained LSM, respectively. LSM was run for ten iterations in both cases. The predicted (reconstructed) surface data show the muting effect of the preconditioning function, which only allows the comparison of the predicted and observed data within the zone of interest, excluding direct waves and headwaves. When compared with the original dataset, we observe that conventional migration fails to reproduce the scale of magnitude of the data, whereas both unconstrained and constrained LSM achieve this goal while attenuating background noise at the same time. Although constrained LSM exhibits fewer early and late phantom events than the unconstrained case, it introduces some high-frequency noise in the background.

Figures B6-B8 show a common-offset gather at h = 150 m after conventional migration, unconstrained LSM and constrained LSM, respectively. Unconstrained LSM slightly attenuates the aliased noise compared with conventional migration, whereas the highest attenuation is achieved with constrained LSM, as expected. Another important improvement using both unconstrained and constrained LSM is the virtual elimination of the migration artifacts below the main horizontal event after conventional migration.

Figure B9 shows the three cases for a common reflection point gather at x = 3750 m. The attenuation of the migration artifacts is analogous to that in the previous set of common-offset gather figures. Additionally, the continuity of the flat event is improved by the constraint function. However, what constitutes a drawback for constrained LSM (using a five-point median filter) is the creation of spurious flat events as a consequence of artificial connectivity of numerical artifacts. I suspect that these artifacts give rise to the medium to high frequency noise introduced in both the full stack and the predicted data. For this reason, in the 3D calculations shown in Chapter III a more sophisticated structure-oriented filter was utilized to constrain the data, thus avoiding the generation of spurious flat events.

Figures B10-B12 show the corresponding full-stack sections. As observed by Kühl and Sacchi (2003), the quality of the stack sections using conventional migration and LSM are comparable, thanks to the healing effect of the stacking process. However, constrained LSM exhibits enhanced migration artifacts as a consequence of the spurious flat events observed in the common reflection point gather.

Finally, Figure B13 shows the decrease of the residual, the gradient, the model difference and the data difference as a function of the iteration number.

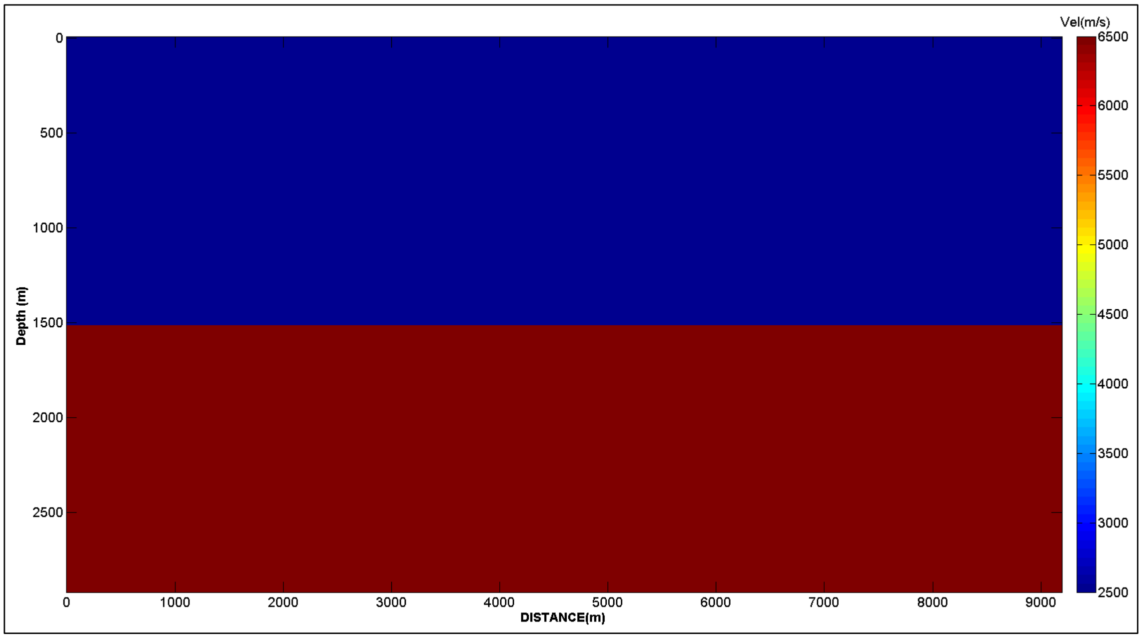

Figure B1. Two-layer velocity depth model.

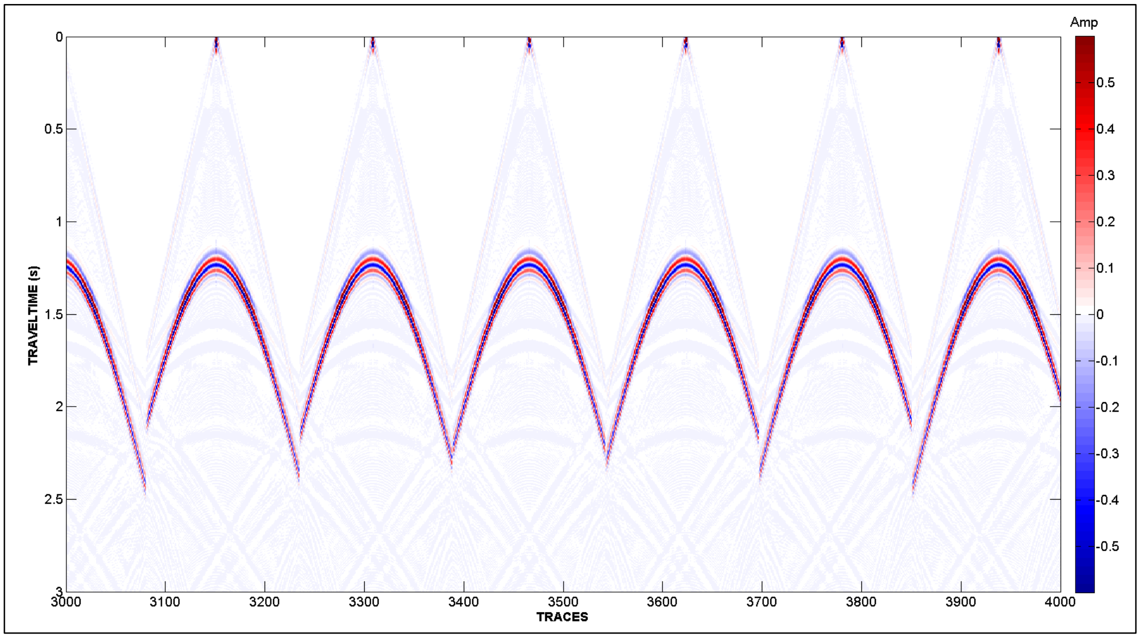

Figure B2.Representative shot gathers, $\mathbf{d}_0$, generated for the two-layer model using a finite difference solution of the scalar equation.

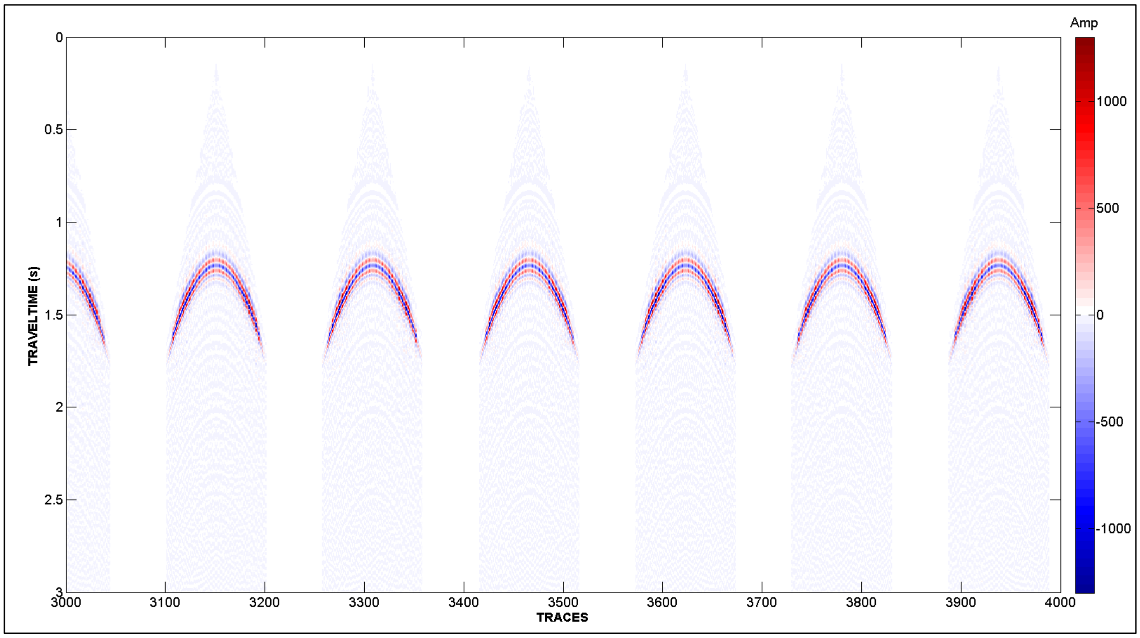

Figure B3. Predicted (modeled) common shot gathers, **d**, from the conventionally migrated vector, **m**. Note the data inside the mute zone are not predicted. Also, note the amplitudes between the two images differ by three orders of magnitude.

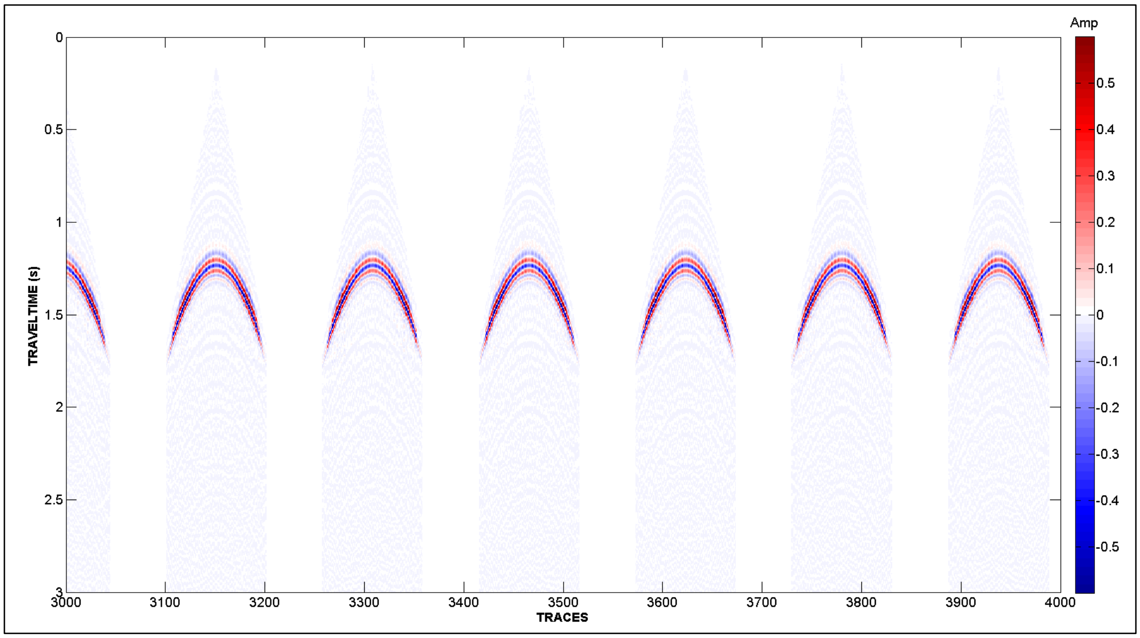

Figure B4. Predicted (modeled) common shot gathers, **d**, computed from the unconstrained LSM vector, **m**. Note the predicted data have the same amplitude values as the input data.

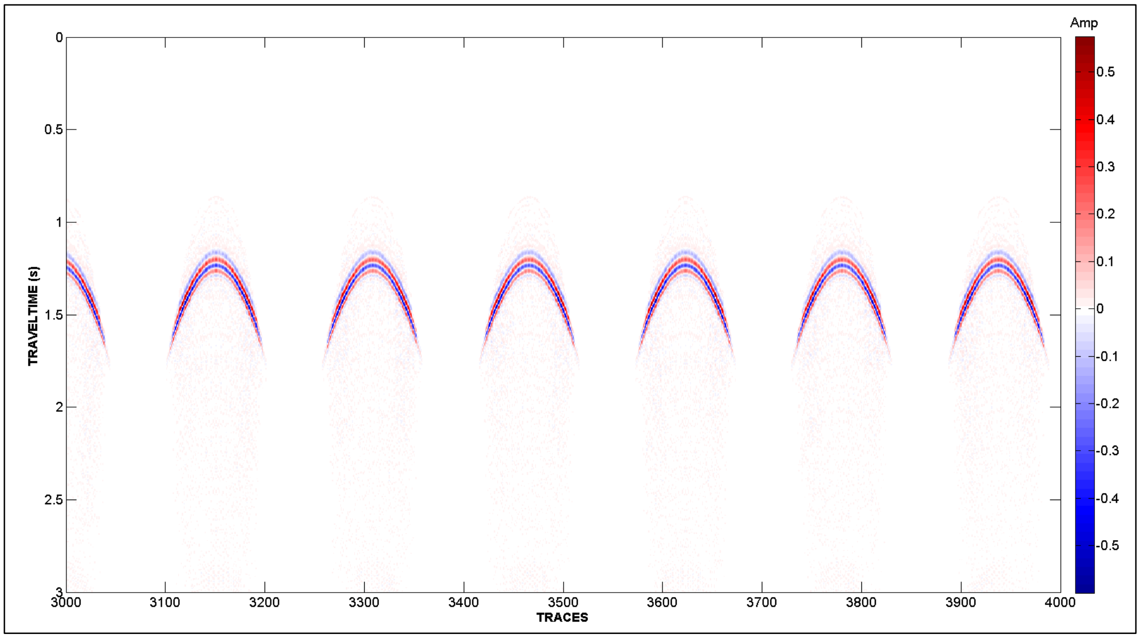

Figure B5. Predicted (modeled) common shot gathers, **d**, computed from the constrained LSM vector, **m**. Note the predicted data have the same amplitude values as the input data.

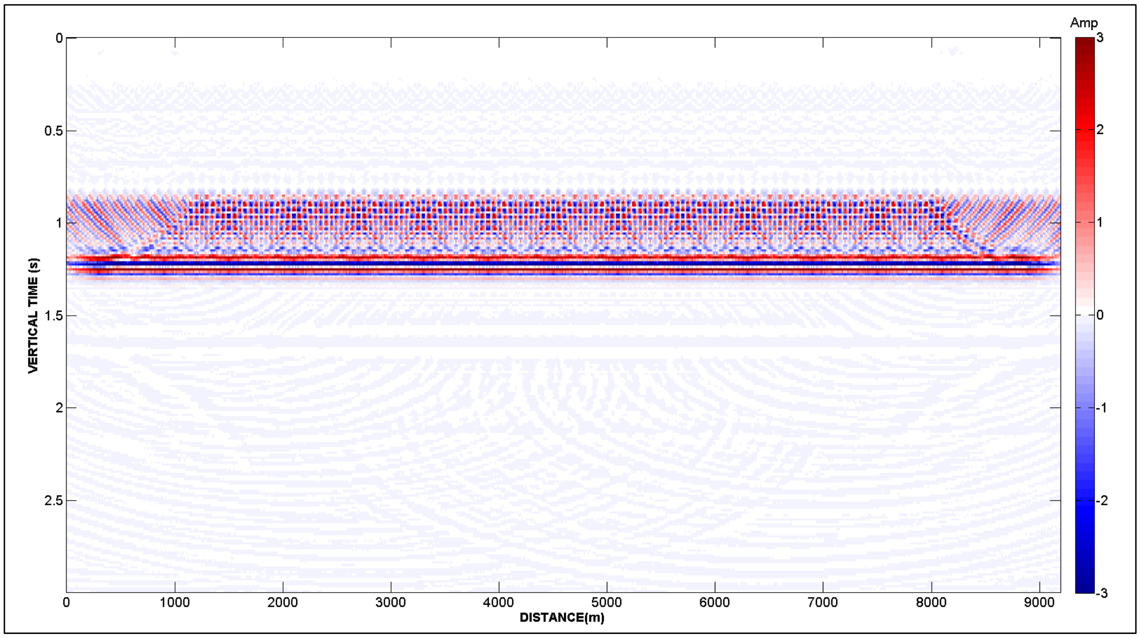

Figure B6. Common offset gather, **m**, at *h* = 150 m computed for the two-layer model using conventional migration.

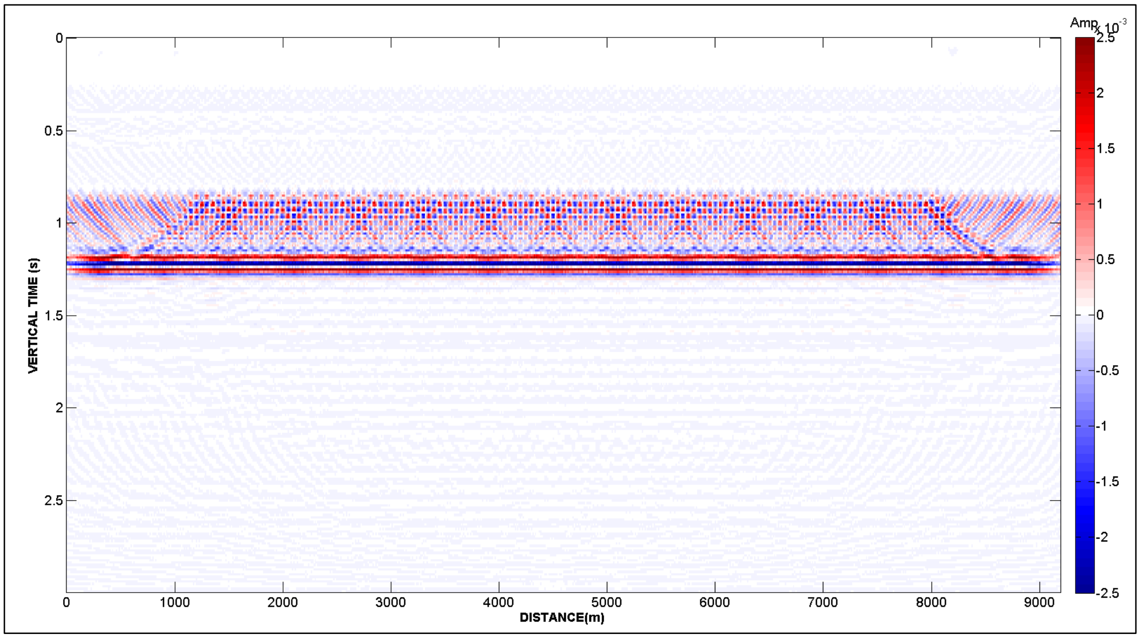

Figure B7. Common offset gather, **m**, at *h* = 150 m computed for the two-layer model using unconstrained LSM.

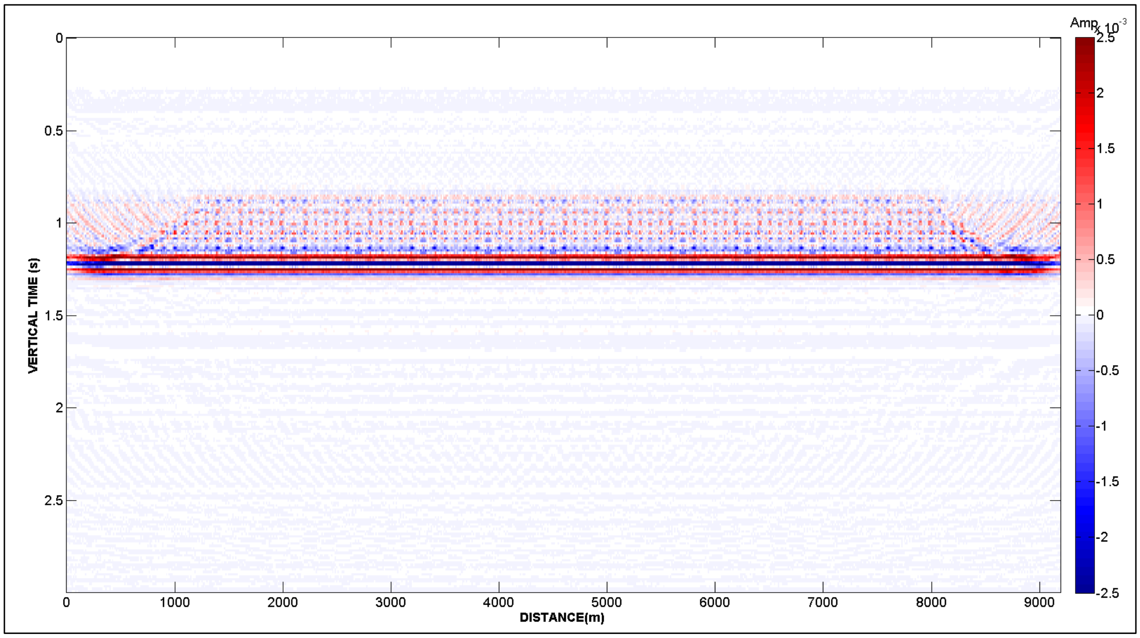

Figure B8. Common offset gather, **m**, at *h* = 150 m computed for the two-layer model using constrained LSM.

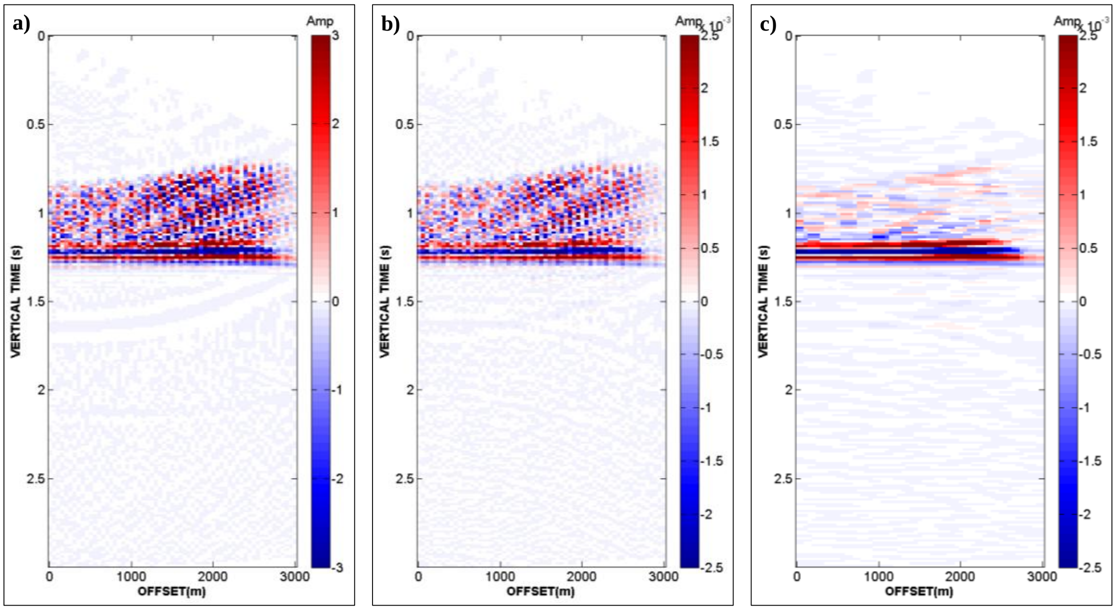

Figure B9. Common reflection point gathers, **m**, at *x* = 3750 m computed using (a) Conventional migration, (b) Unconstrained LSM, and (c) Constrained LSM.

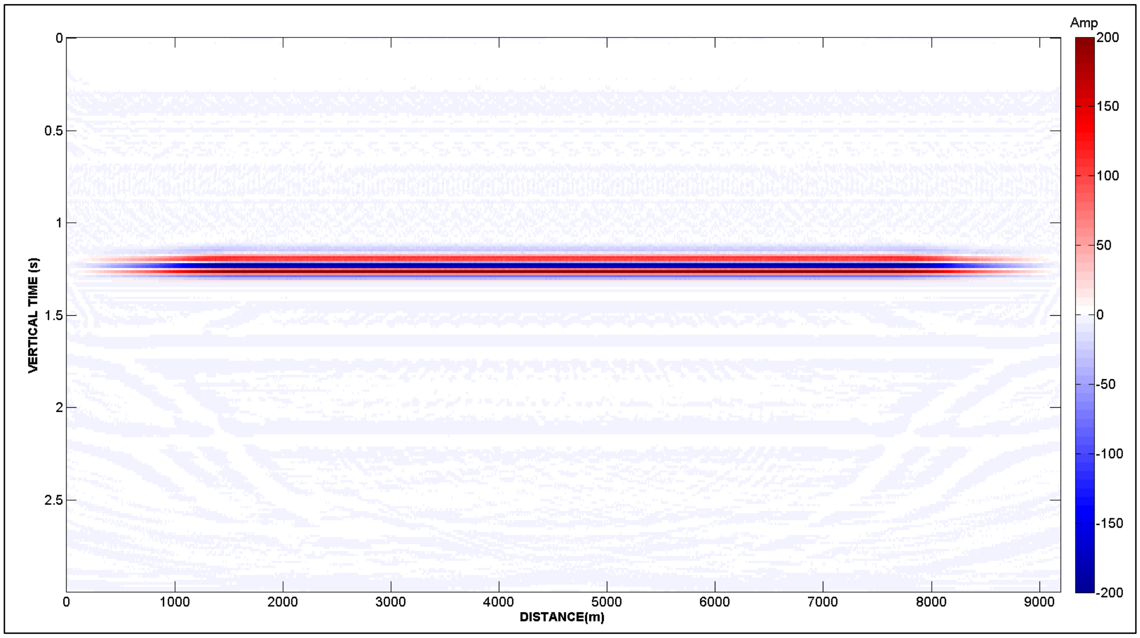

Figure B10. Stacked image of **m** over all offsets for the two-layer model using conventional migration.

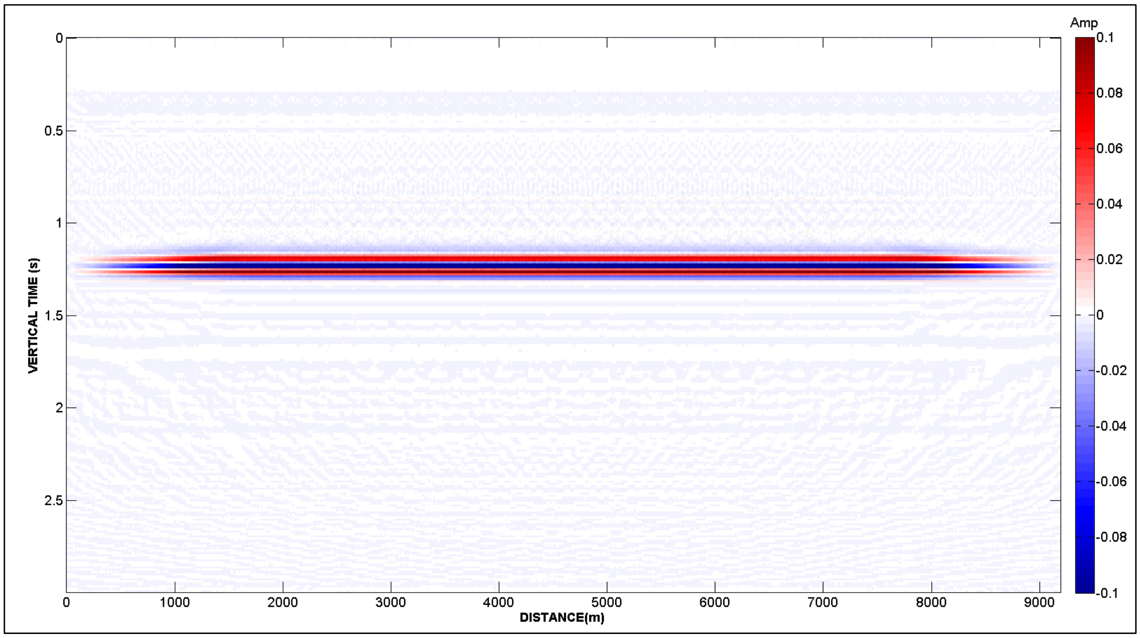

Figure B11. Stacked image of **m** over all offsets for the two-layer model using unconstrained LSM.

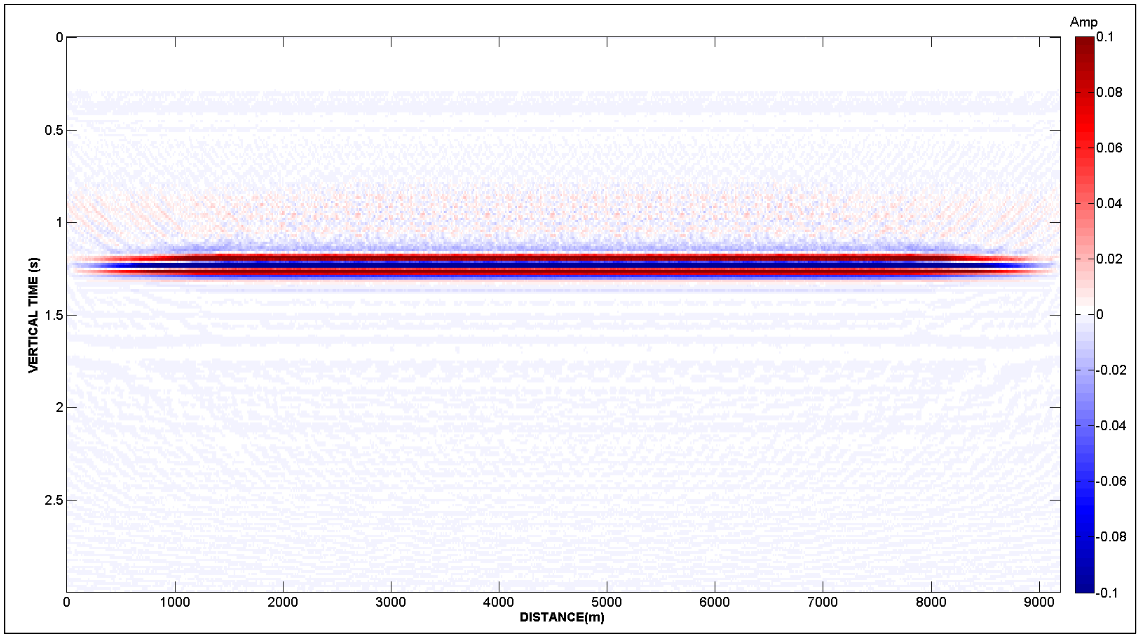

Figure B12. Stacked image of **m** over all offsets for the two-layer model using constrained LSM.

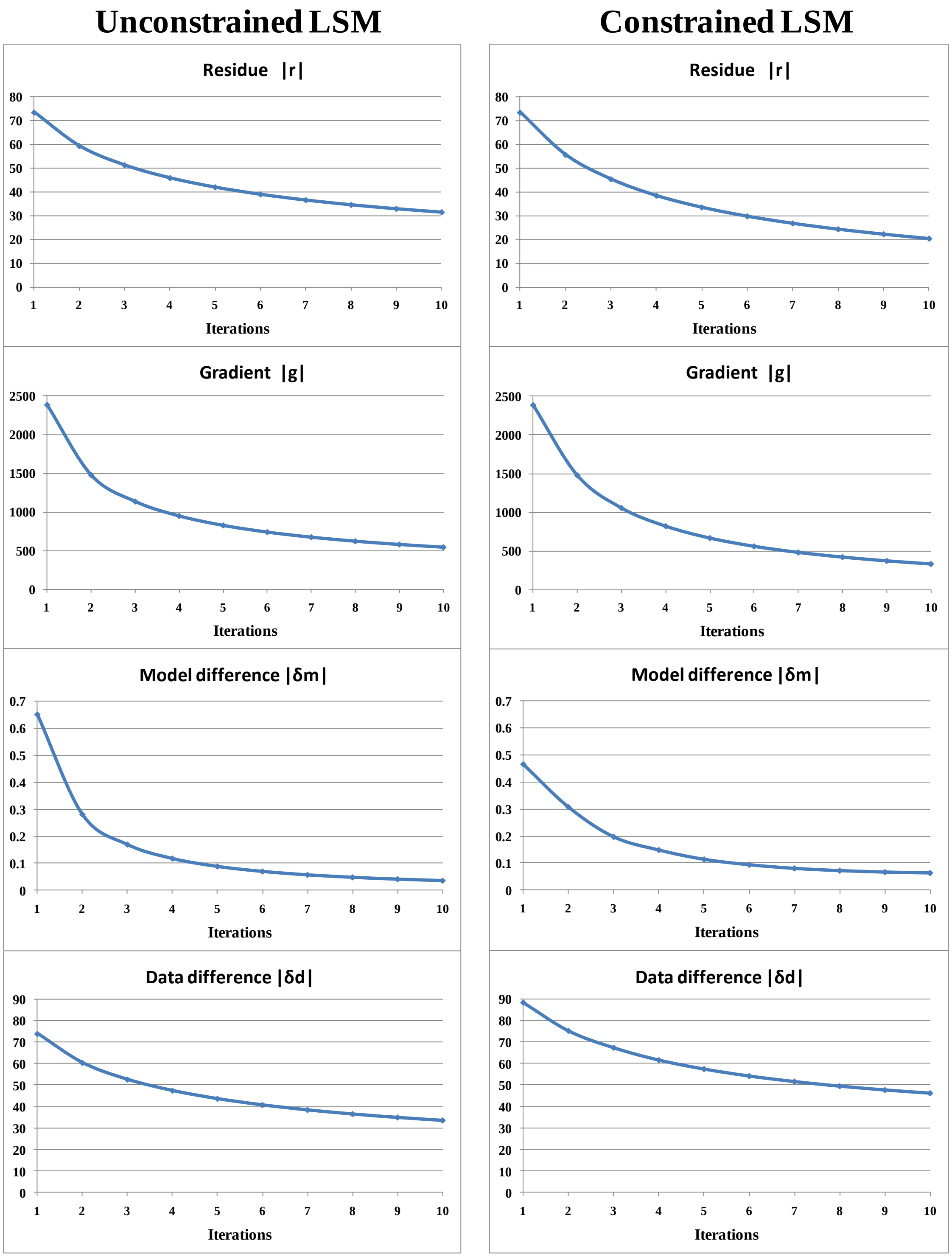

Figure B13. Behavior of the residual, the gradient, the model difference and the data difference with unconstrained and constrained LSM for the two-layer model. Note that the unconstrained migration more closely fits the surface data, $\mathbf{d}_0$, as evidence by the smaller value of |**δd**|. To do so, the unconstrained model will make use of aliases in the migration domain. Although this example shows the behavior using ten iterations, a more efficient algorithm would stop iterating after the change in |**δd**| falls below a threshold (the convergence slows down). In contrast, the residual and the gradient tend to converge faster because the constraint function constitutes a preconditioning factor.

Decimated input data

Figure B14 shows representative shot gathers from the decimated dataset, obtained after randomly killing two thirds of the traces. Figures B15-B17 show the predicted data after conventional migration, unconstrained LSM and constrained LSM, respectively. Although the unconstrained LSM better predicts the decimated data vector, $\mathbf{d_m}$, through the use of aliases in the model domain, $\mathbf{m}$, the constrained LSM better reconstructs the missing traces of the data vector by suppressing these aliases through the constraints, such that $\mathbf{d}$ now approximates the original undecimated data, although some voids still persist. As in the undecimated case, the magnitude of the amplitudes is accurately reconstructed with either implementation of LSM.

Figures B18-B20 show a common-offset gather at h = 150 m after conventional migration, unconstrained LSM and constrained LSM, respectively. Conventional migration and unconstrained LSM exhibit similar artifacts, except that the later arriving "smiles" are eliminated by LSM. Constrained LSM, however, notably improves the continuity of the horizontal reflector, filling the voids that otherwise can mislead the interpretation.

Similarly, Figure B21 shows the three cases for the common reflection point gather at x = 3750 m, where constrained LSM enhances horizontal events at the expense of introducing additional spurious flat events. Conventional migration and unconstrained LSM yield similar quality, as observe by Kühl and Sacchi (2003).

Figures B22-B24 show the final migration stack, where the quality of the sections is similar again. In contrast to the undecimated case, constrained LSM does not generate more high-amplitude noise than conventional migration and unconstrained LSM, yet it produces additional high-frequency artifacts corresponding to the spurious flat events introduced by the median filter constraint in the common reflection point gathers.

Finally, the plots of the residue, the gradient and model difference are shown in Figure B25.

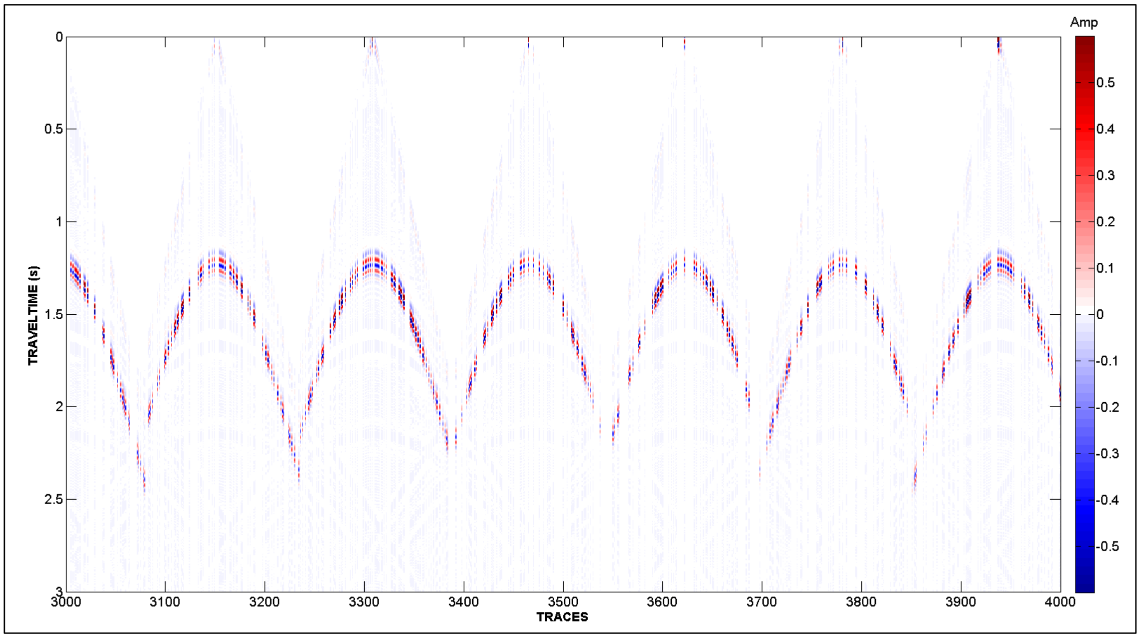

Figure B14. Representative common shot gathers from the decimated two layer model corresponding to Figure B2.

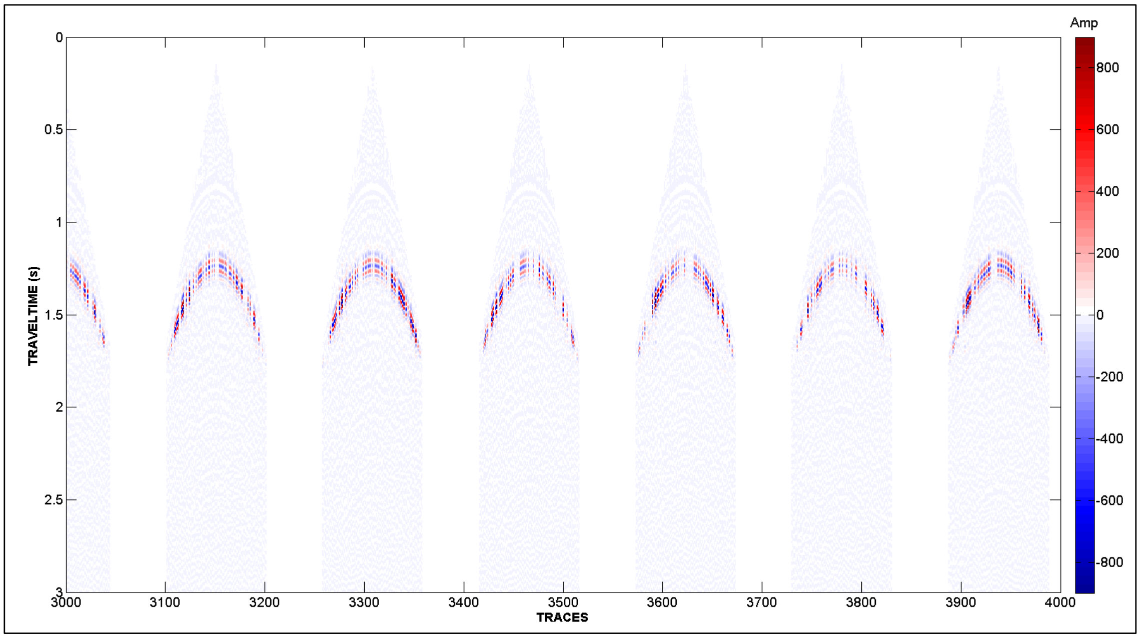

Figure B15. Predicted (modeled) common shot gathers, **d**, computed from the conventionally migrated vector, **m**. Note that data gaps in **d** persist.

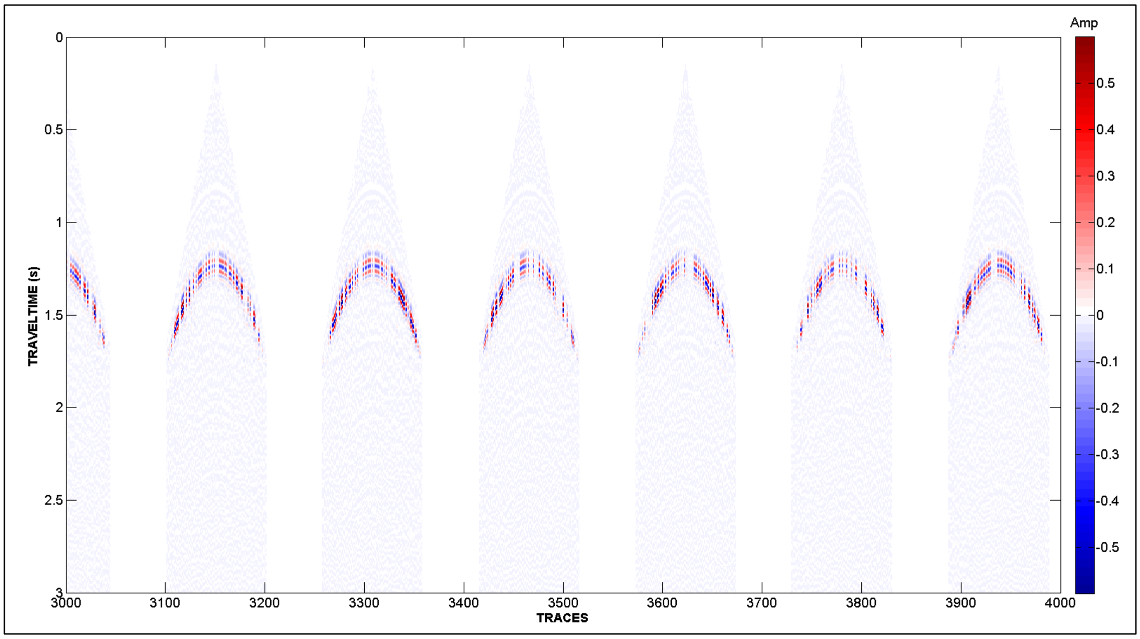

Figure B16. Predicted (modeled) common shot gathers, **d**, computed from the unconstrained LSM migrated vector, **m**. Note that data gaps in **d** persist.

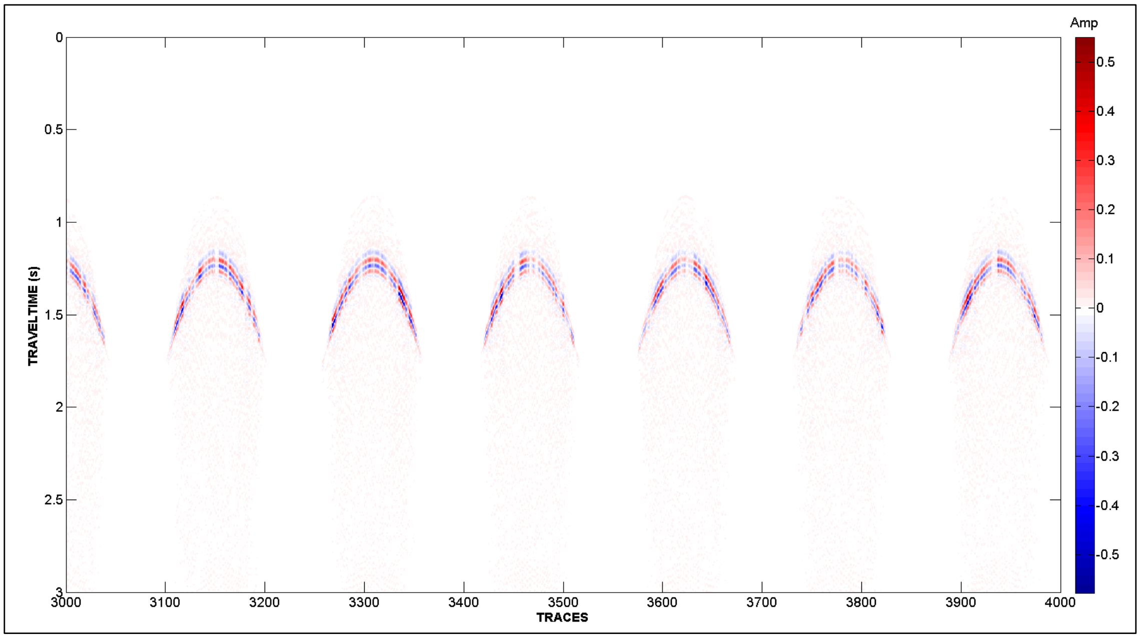

Figure B17. Predicted (modeled) common shot gathers, **d**, computed from the constrained LSM migrated vector, **m**. Note that most gaps in **d** are now healed.

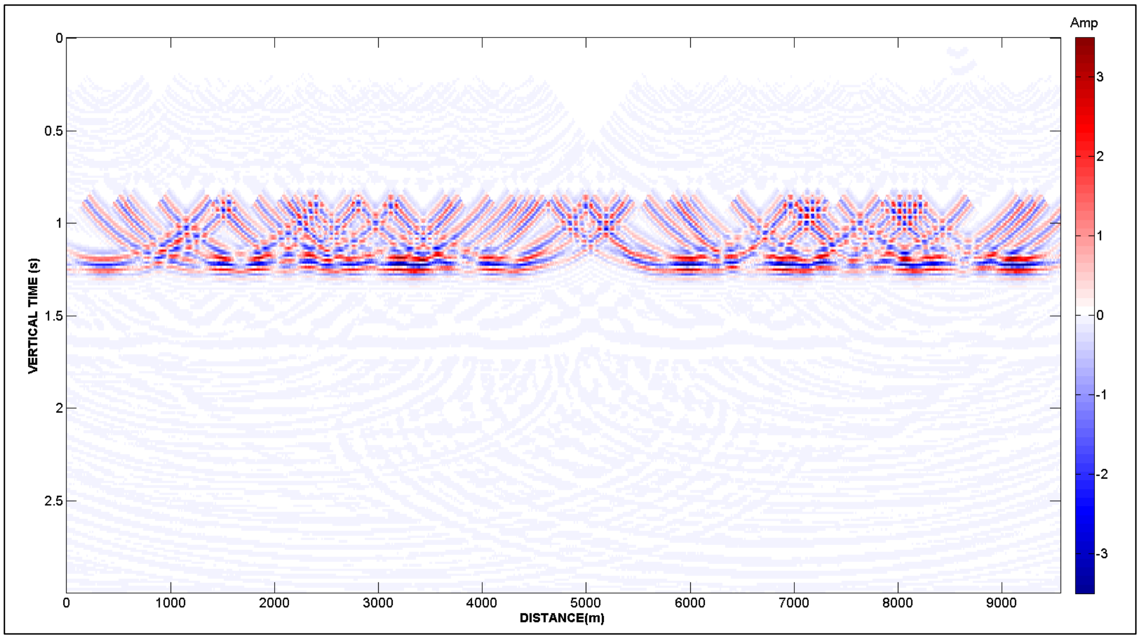

Figure B18.- Common offset gather, **m**, at *h* = 150 m computed from the decimated dataset for the two-layer model using conventional migration. Compare to Figure B6.

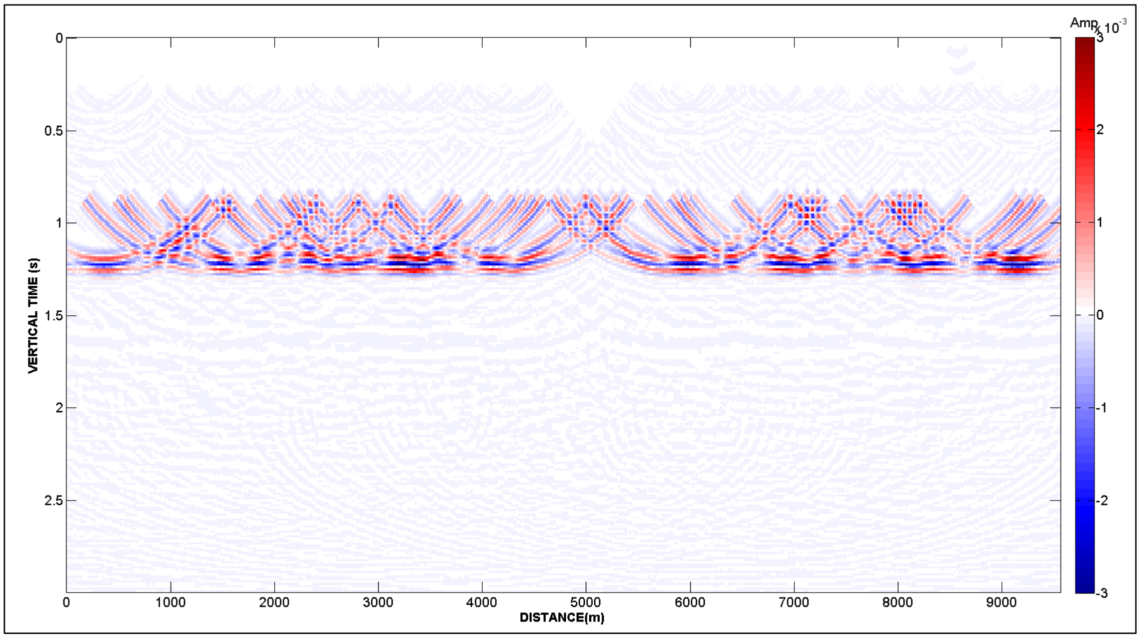

Figure B19. Common offset section gather, m, at *h* = 150 m computed from the decimated dataset for the two-layer model using unconstrained LSM. Compare to Figure B7.

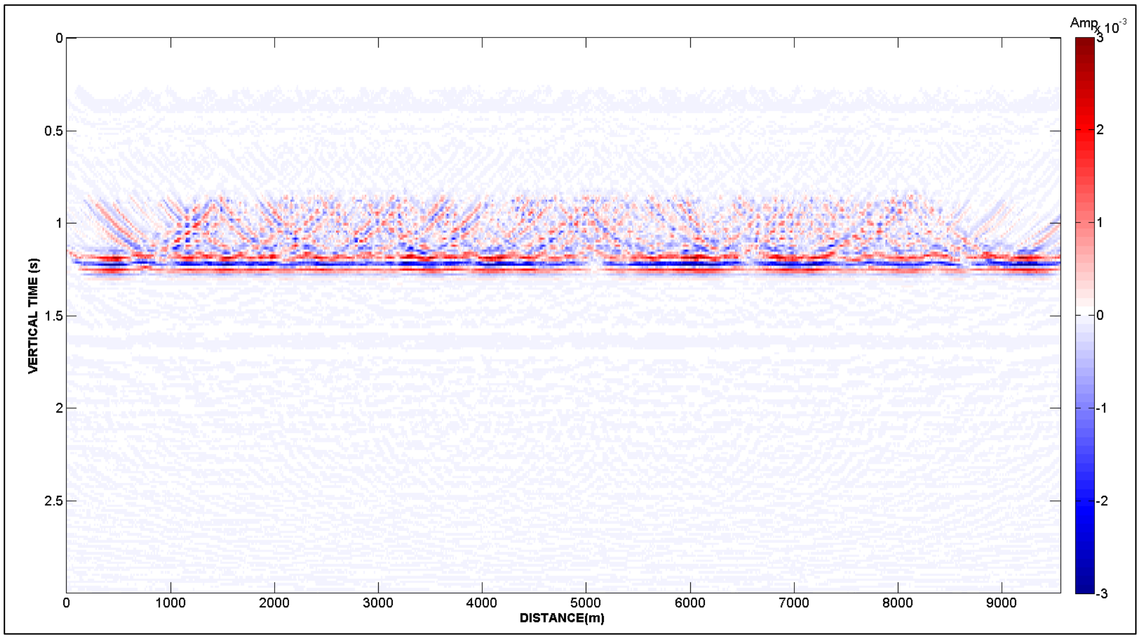

Figure B20. Common offset gather, **m**, at *h* = 150 m computed from the decimated dataset for the two-layer model using constrained LSM. Note that most of the holes in the image have been properly predicted and that the migration smiles are attenuated compared to those in Figure B19. Compare to Figure B8.

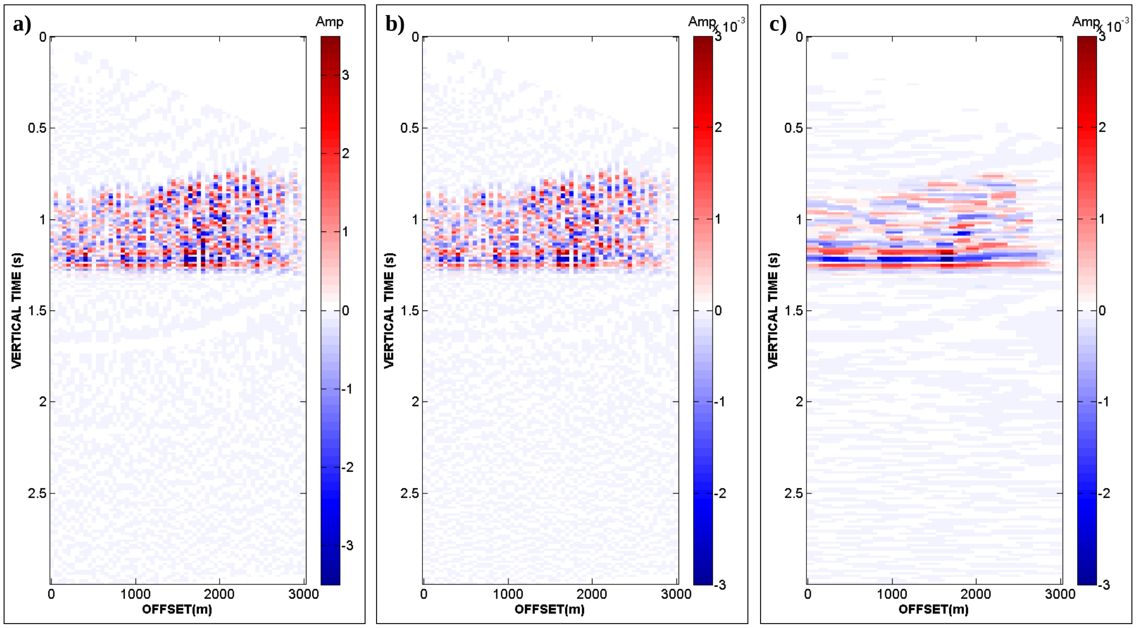

Figure B21. Common reflection point gathers, **m**, at *x* = 3750 m computed from the decimated dataset using (a) Conventional migration, (b) Unconstrained LSM, and (c) Constrained LSM .

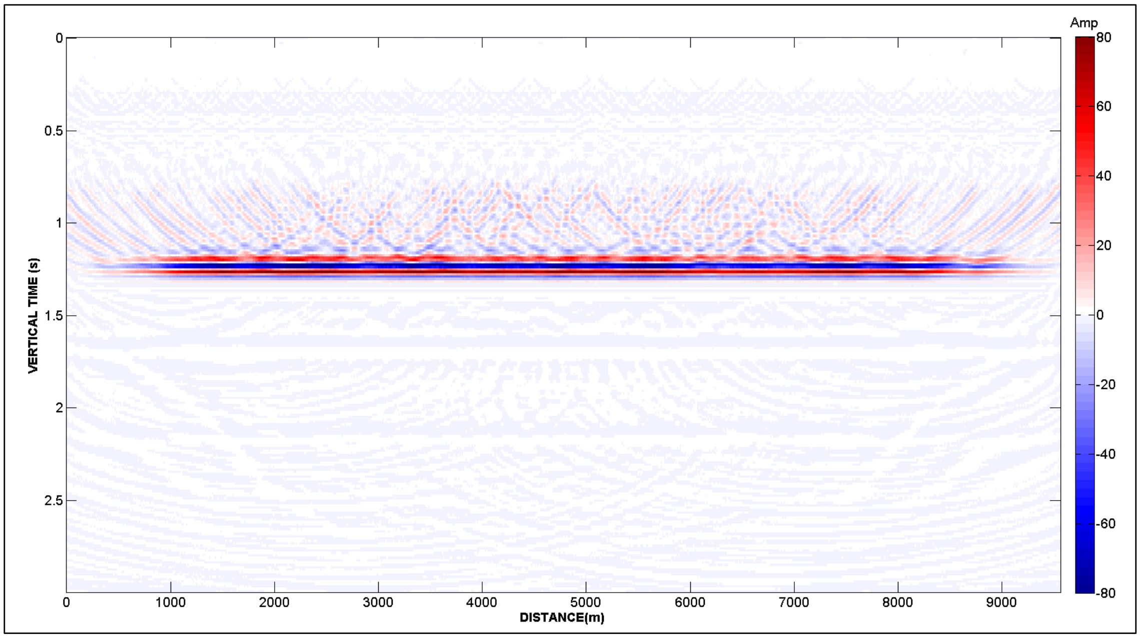

Figure B22. Stacked image of **m** over all offsets for the two-layer model computed from the decimated dataset using conventional migration.

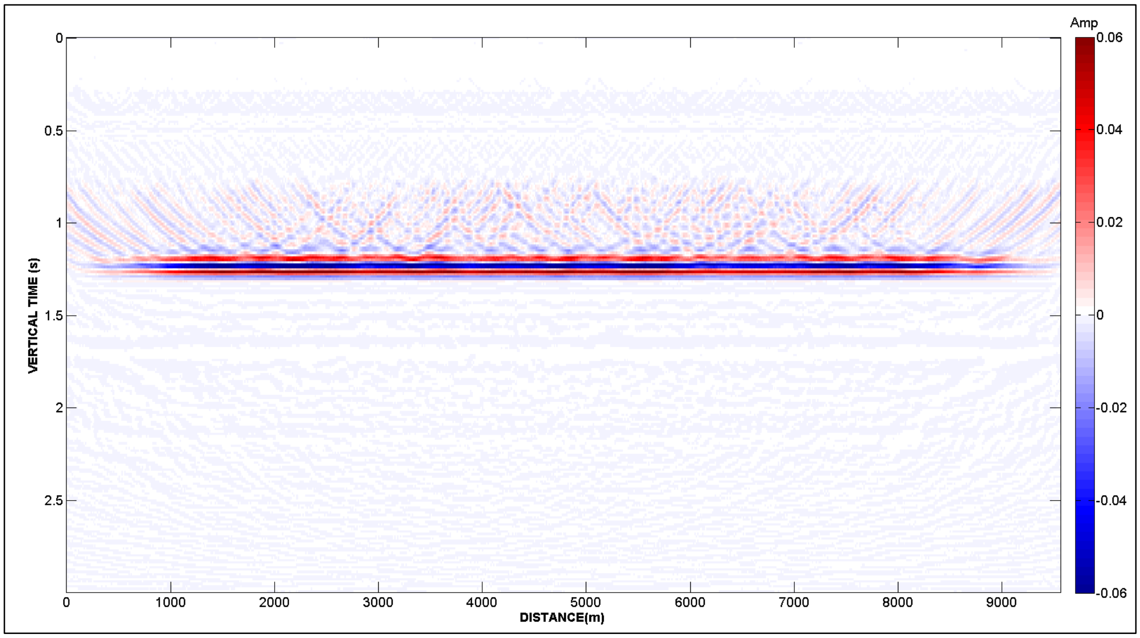

Figure B23. Stacked image of **m** over all offsets for the two-layer model computed from the decimated dataset using unconstrained LSM.

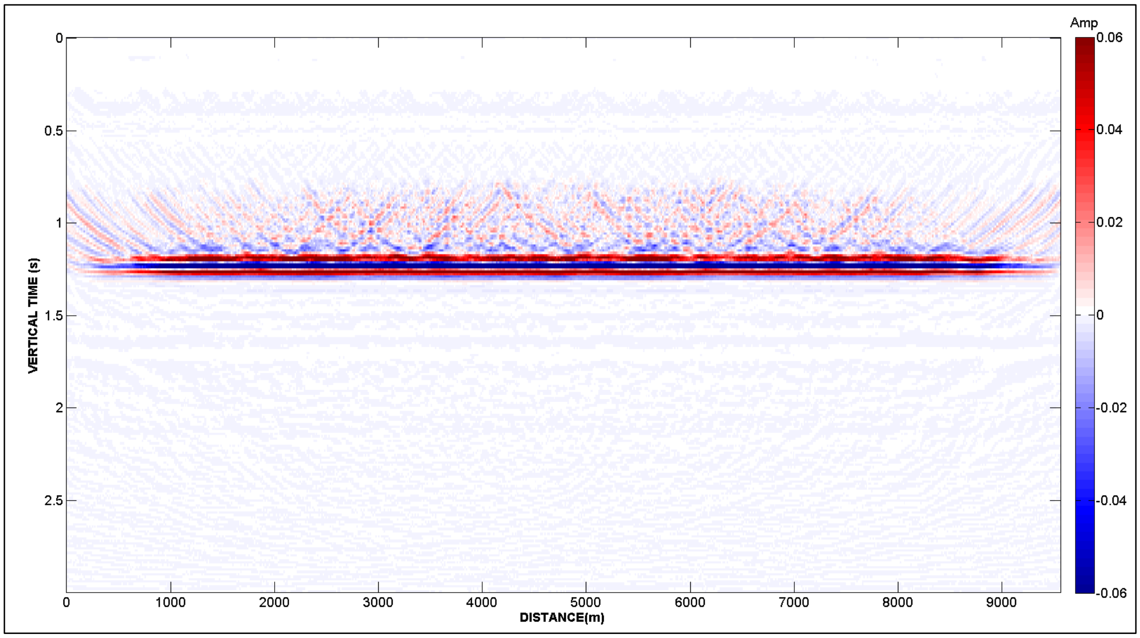

Figure B24. Stacked image of **m** over all offsets for the two-layer model computed from the decimated dataset using constrained LSM.

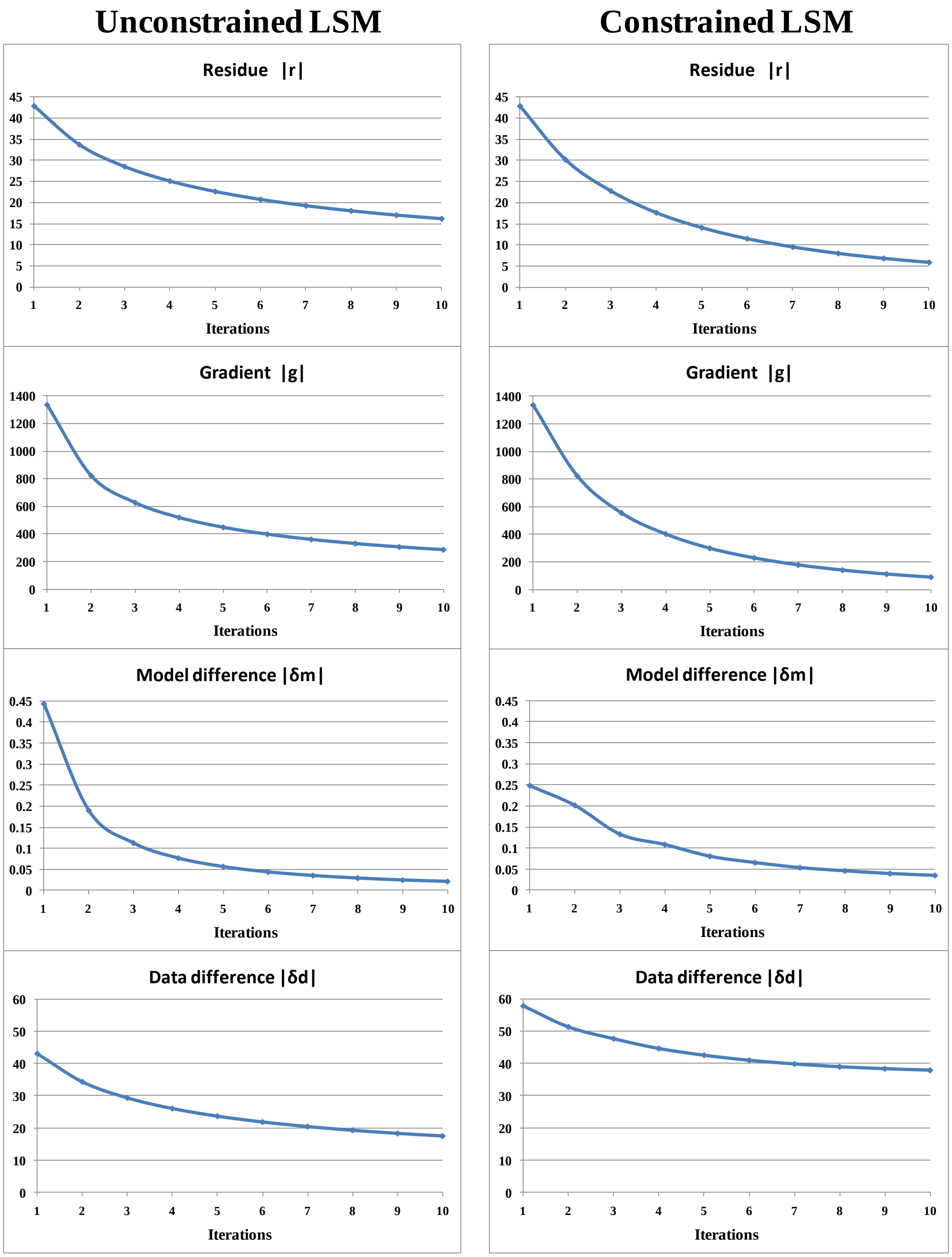

Figure B25. Behavior of the residual, the gradient, the model difference and the data difference with unconstrained and constrained LSM computed from the decimated dataset of the two-layer model. As with the undecimated (full) dataset, the unconstrained migration more closely fits the surface data, $\mathbf{d_0}$, as evidenced by the smaller value of |**δd**|. To do so, the unconstrained model makes use of aliases in the migration domain. In contrast, the residual and the gradient tend to converge faster because the constraint function constitutes a preconditioning factor.

APPENDIX C: Marmousi model

Densely sampled input data

The Marmousi dataset corresponds to the anisotropic version generated by Alkhalifah (1997). The data consist of 232 shots and 136 traces by shot, both spaced 25 m apart, for a total of 31552 traces with time sampling of 4 ms and 3 s of time recording. The velocity and anisotropy models consist of 240 vertical samples and 737 horizontal samples, with spacing of 12.5 m both dimensions. For the sake of better visualization, I plotted the Marmousi results in gray scale.

Figure C1 shows the velocity model and Figure C2 shows a detail of the corresponding shot gathers. Figures C3-C5 show the predicted images using conventional migration and unconstrained and constrained LSM respectively, for five iterations. Whereas conventional migration yields a relatively noisy predicted data, with amplitudes four orders of magnitude greater than the original data, unconstrained and constrained LSM predicted data sections are cleaner and have the correct order of magnitude. Constrained LSM slightly reduces more background noise than unconstrained LSM.

Figures C6-C8 show the common-offset gather at h = 250 m. Other than some attenuation of noisy events at 1.75 s, between 5800 and 6000 m, there is no significant improvement of unconstrained LSM compared to conventional migration. High frequency noise, possibly associated with moderate aliasing becomes greatly attenuated by constrained LSM. The common-offset sections have more frequency content than the full stack sections, allowing more differentiation of thin beds.

Similarly, Figure C9 shows a common reflection point gather at x = 3750 m for the three processes, where there are virtually no changes between conventional migration and unconstrained LSM. Constrained LSM almost eliminates the background noise giving a clean appearance. Spurious flat events are not observed.

Figures C10-C12 show the final stacked sections. In this case both unconstrained and constrained LSM reduce low frequency artifacts due to stretch both in the left and right packages of sediments, which improves the resolution of some thin beds and the visibility of some faults in the middle shallow section. There is no difference between unconstrained and constrained LSM because there was no noise produced by spurious flat events in the latter.

Finally, Figure C-13 shows the reduction of the residual, the gradient, model difference and the data difference.

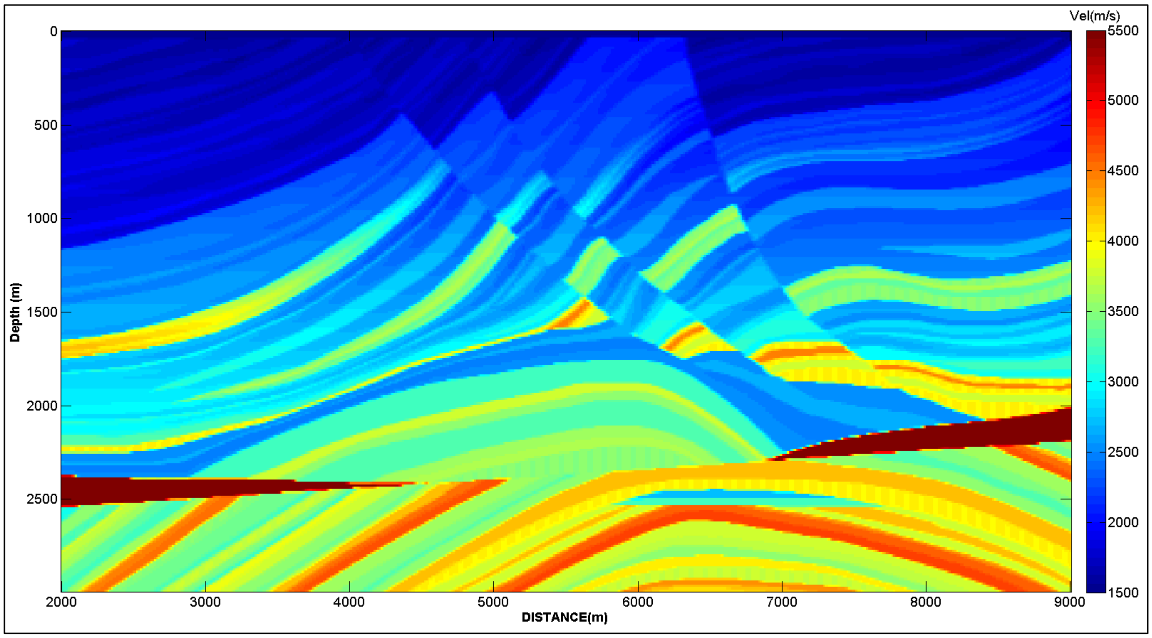

Figure C1. Marmousi velocity depth model.

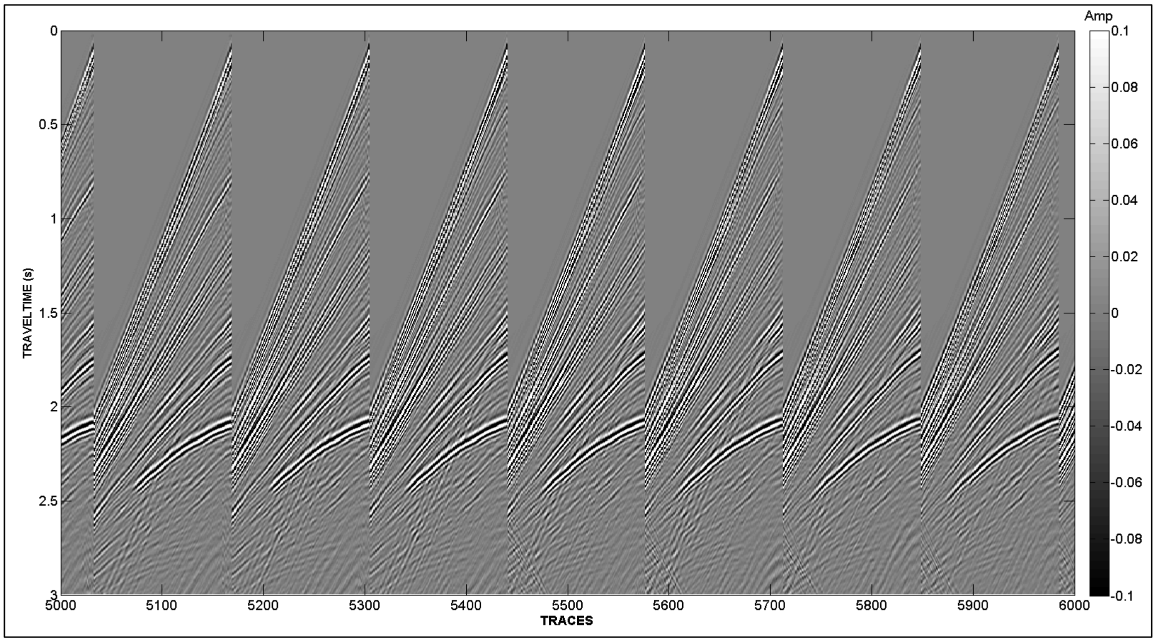

Figure C2. Representative shot gathers, $\mathbf{d_0}$, generated for the Marmousi model.

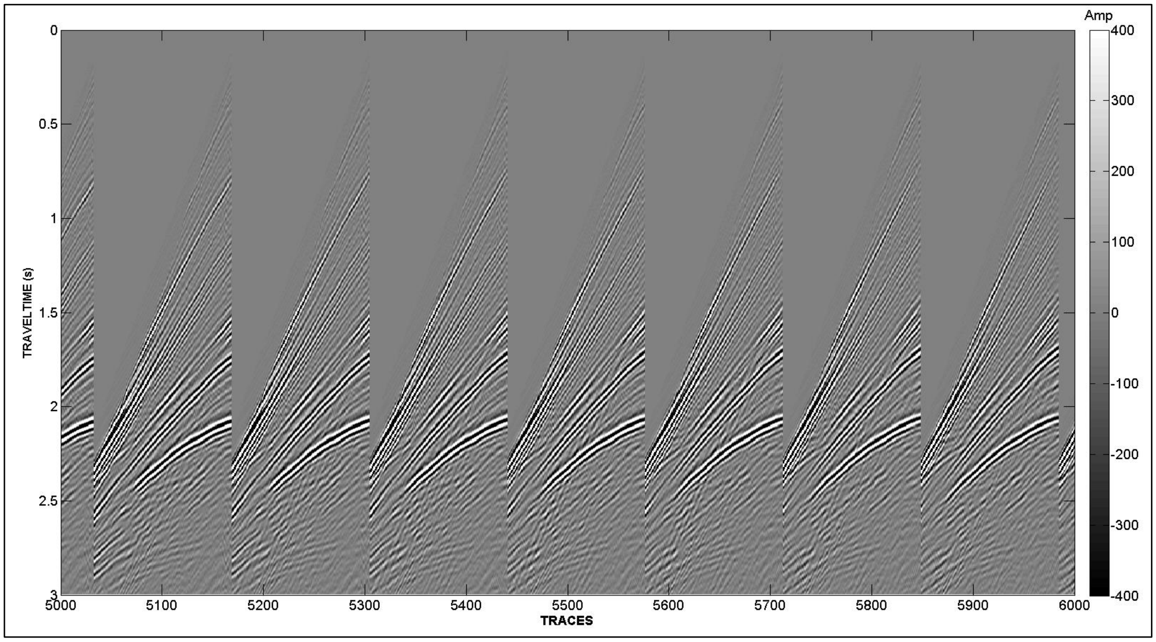

Figure C3. Predicted (modeled) common shot gathers, **d**, from the conventionally migrated vector, **m**..

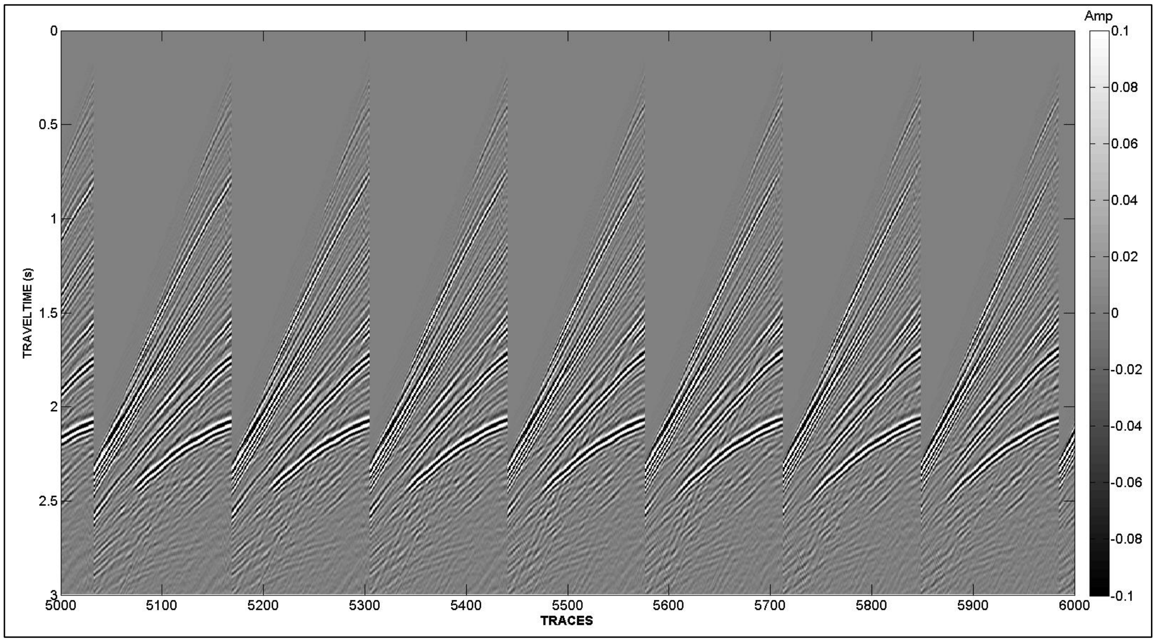

Figure C4. Predicted (modeled) common shot gathers, **d**, computed from the unconstrained LSM vector, **m**.

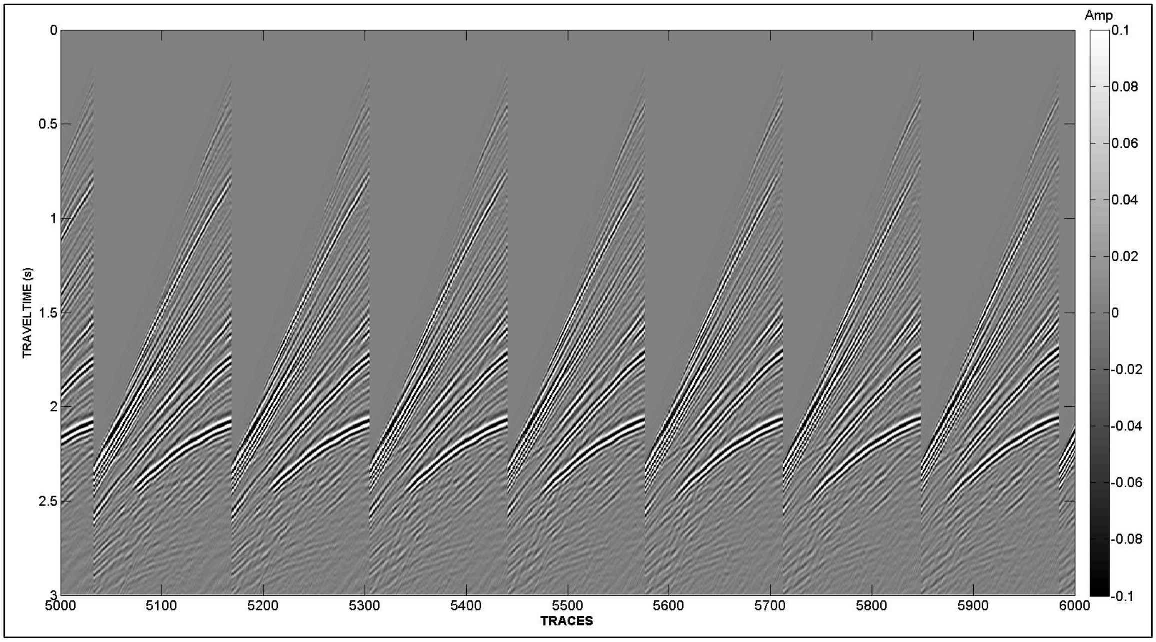

Figure C5. Predicted (modeled) common shot gathers, **d**, computed from the constrained LSM vector, **m**.

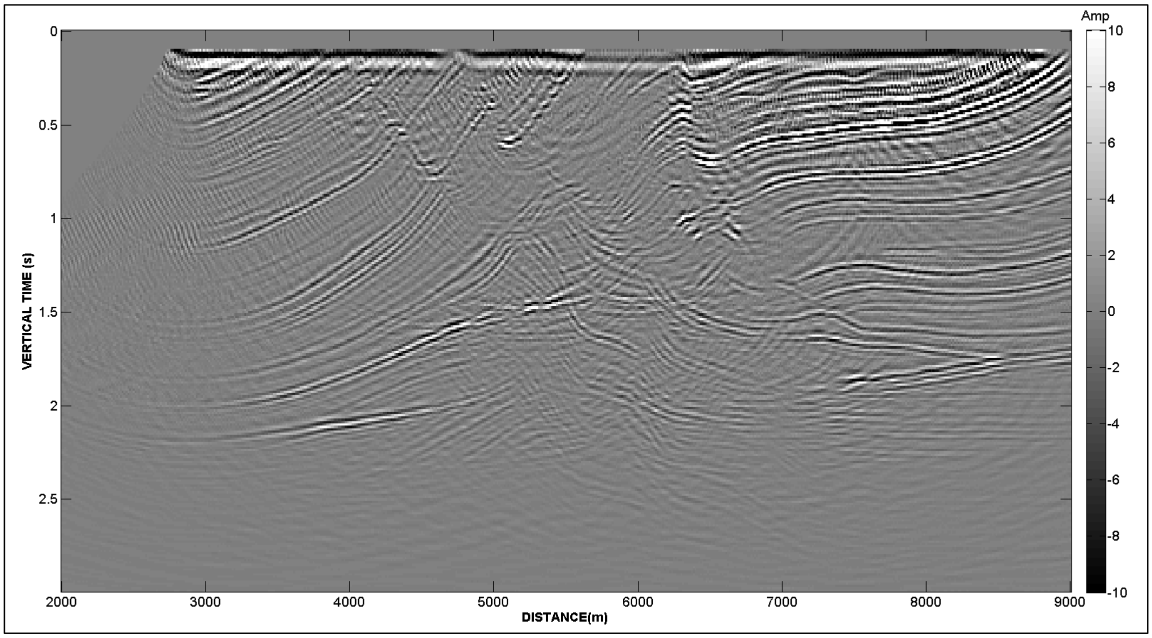

Figure C6. Common offset gather, **m**, at *h* = 250 m computed for the Marmousi model using conventional migration.

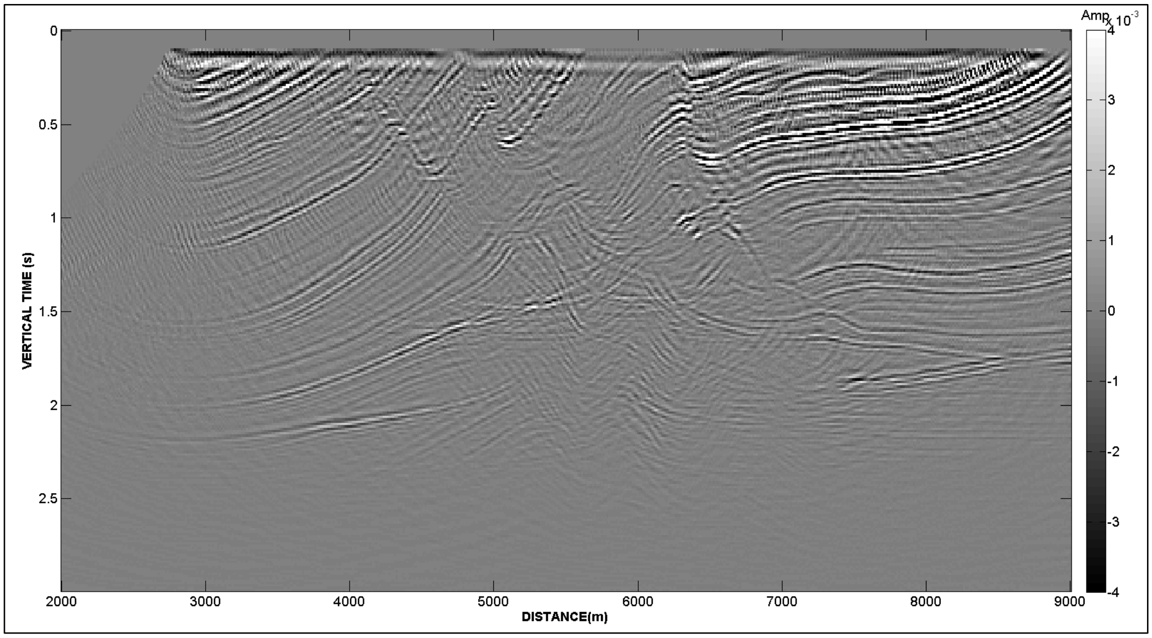

Figure C7. Common offset gather, **m**, at *h* = 250 m computed for the Marmousi model using unconstrained LSM.

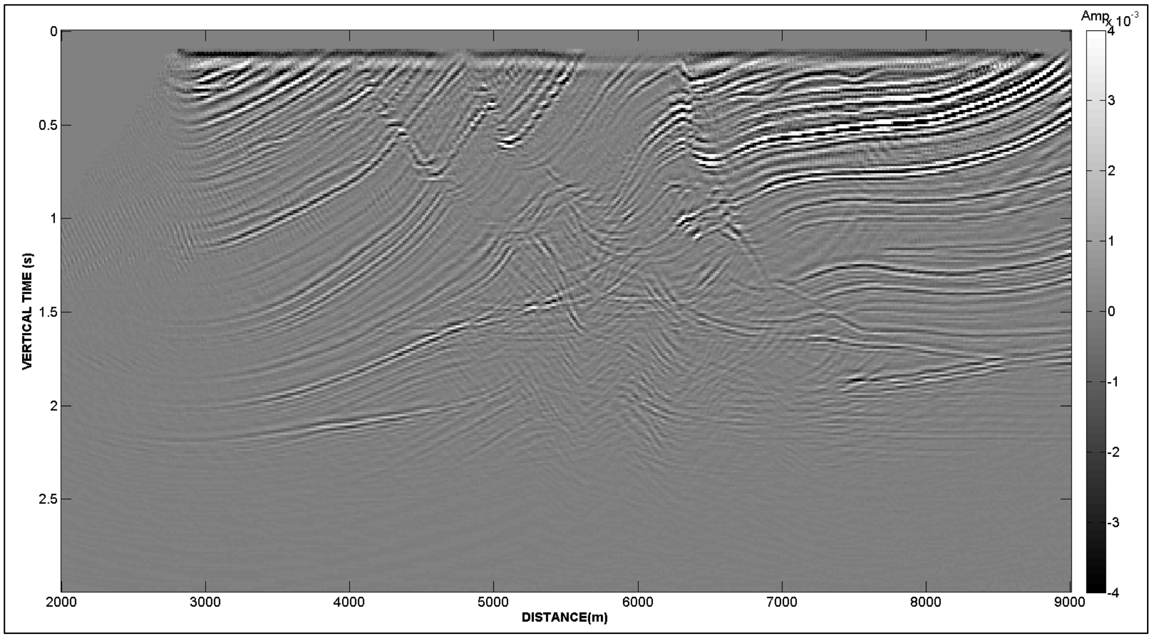

Figure C8. Common offset gather, **m**, at *h* = 250 m computed for the Marmousi model using constrained LSM.

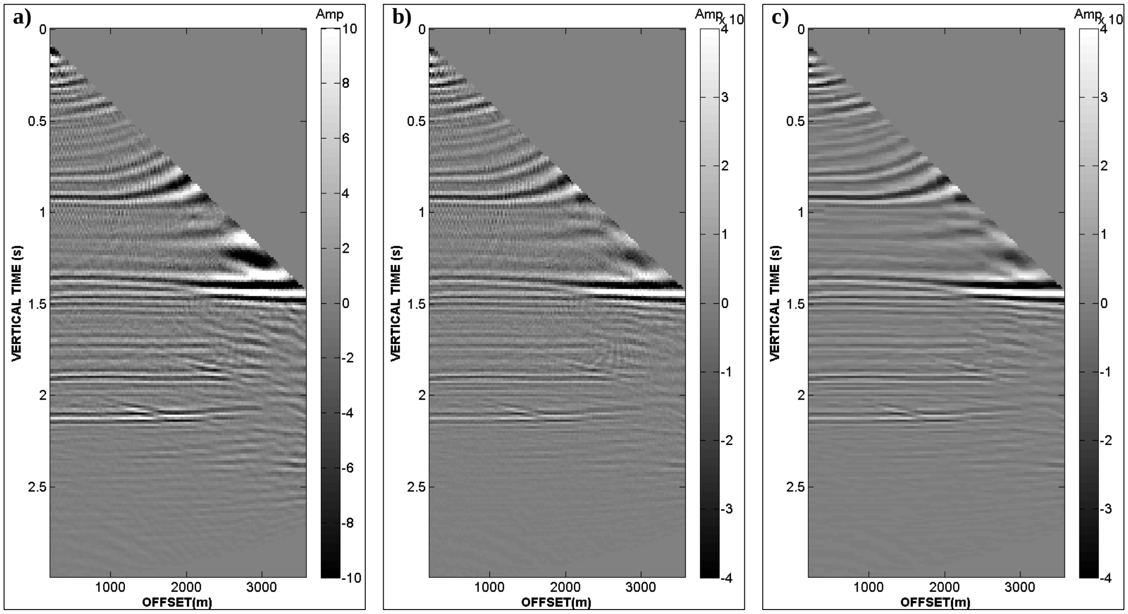

Figure C9. Common reflection point gathers, **m**, at *x* = 3750 m computed using (a) Conventional migration, (b) Unconstrained LSM, (c) Constrained LSM.

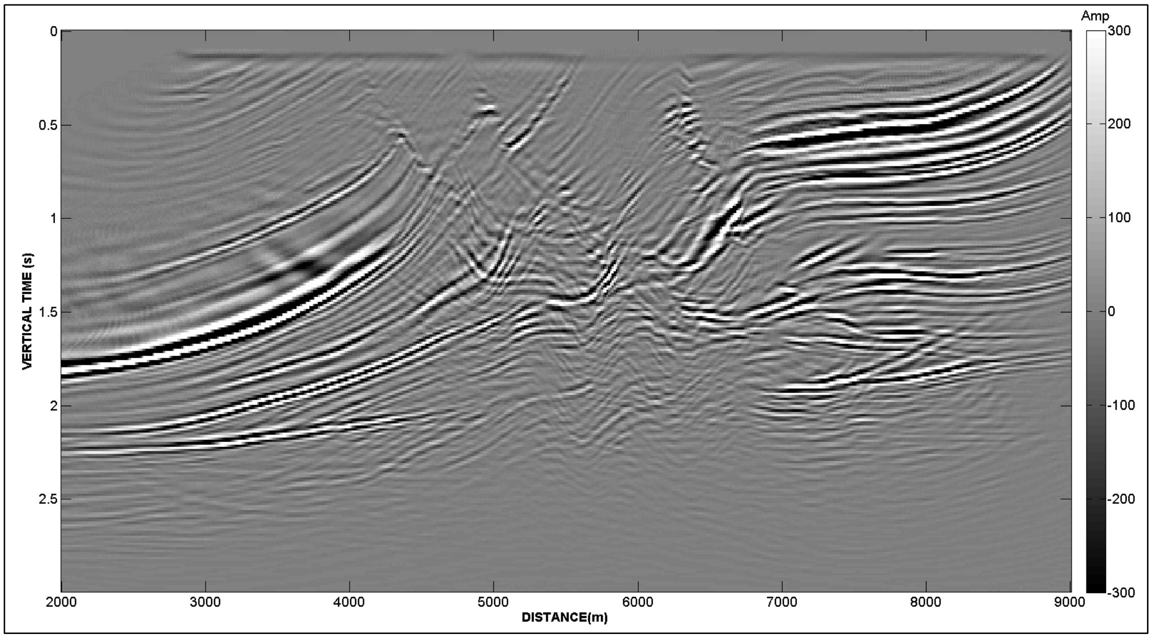

Figure C10. Stacked image of **m** over all offsets for the Marmousi model using conventional migration.

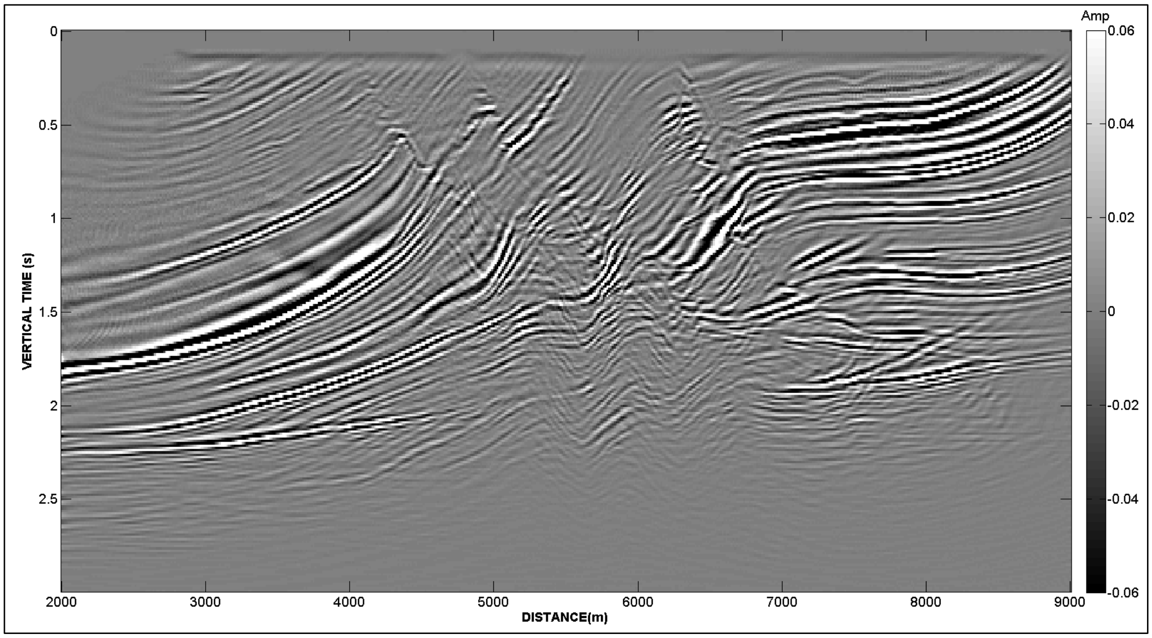

Figure C11. Stacked image of **m** over all offsets for the Marmousi model using unconstrained LSM.

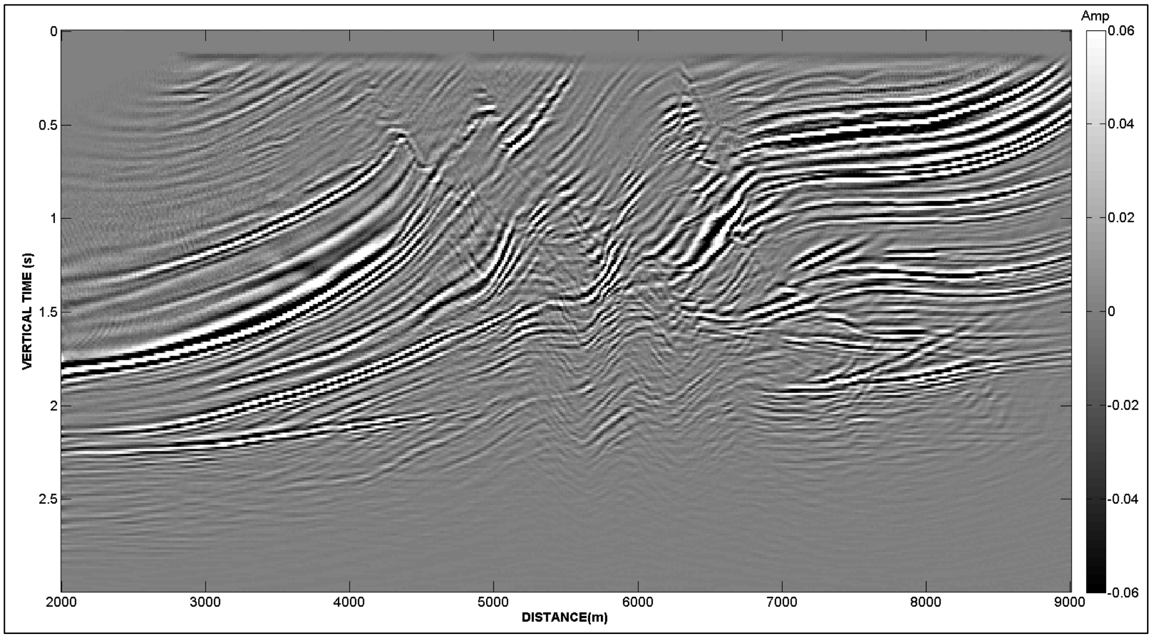

Figure C12. Stacked image of **m** over all offsets for the Marmousi model using constrained LSM.

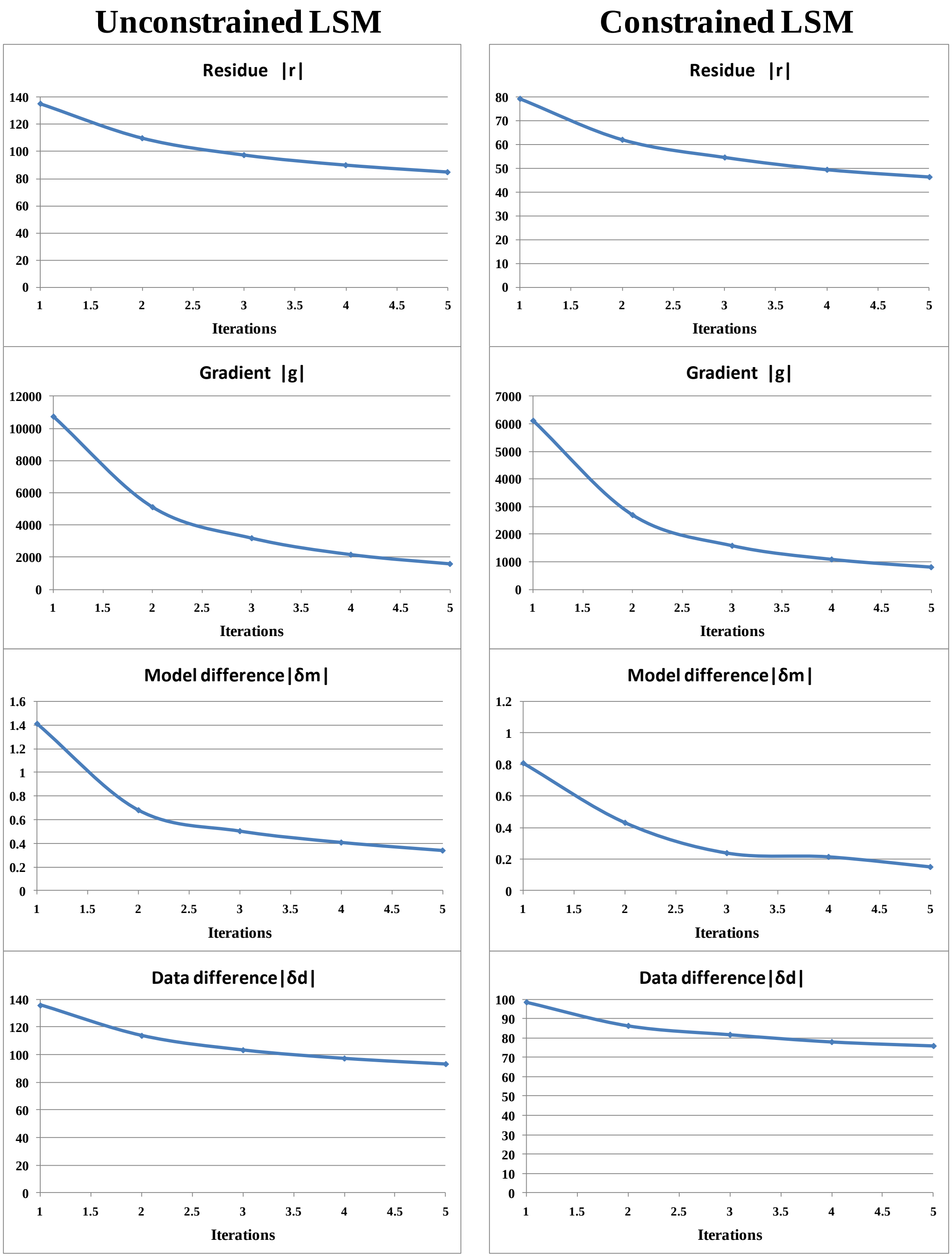

Figure C13. Behavior of the residual, the gradient, the model difference and the data difference with unconstrained and constrained LSM for the Marmousi model. The plots look very similar because the filtering introduced by the constraint function suppressed the very little noise, since the Marmousi model is adequately sampled, hence exhibiting minimum aliasing.

Decimated input data

Figure C14 shows representative shot gathers from the decimated dataset, after randomly killing two thirds of the traces. Figures C15-C17 show the predicted data after conventional migration, unconstrained and constrained LSM, respectively, run until five iterations. Both conventional migration and unconstrained LSM predict the data without adequately interpolating the gaps and with some background noise. Unconstrained LSM corrects the amplitudes to the order of magnitude of the data, as expected. On the other hand, constrained LSM greatly improves the predicted data by attenuating the background noise and better predicting the missing traces. Compare to Figure C5.

Figures C18-C20 show a common-offset gather at h = 250 m after the three processes. Conventional migration and unconstrained LSM sections look very similar with the geologic framework difficult to interpret due to severe aliasing artifacts, particularly in the shallower section. After constrained LSM the geology becomes clearer and easier to interpret after most of the aliasing artifacts have been attenuated.

Similarly, Figure C21 shows the common reflection point gather at x = 3750 m, where conventional migration and unconstrained LSM sections look almost identical, with the aliasing artifacts affecting the flat events. Constrained LSM virtually eliminates the noise, resulting in an image almost free of spurious flat events.

Figures C22-C24 show the final stacked sections. The three sections are similar in quality, with some improvements of marginal events in the LSM cases. There is not apparent noise related to spurious flat events in the constrained LSM section.

Finally, Figure C-25 shows the reduction of the residual, the gradient, the model difference and the data difference.

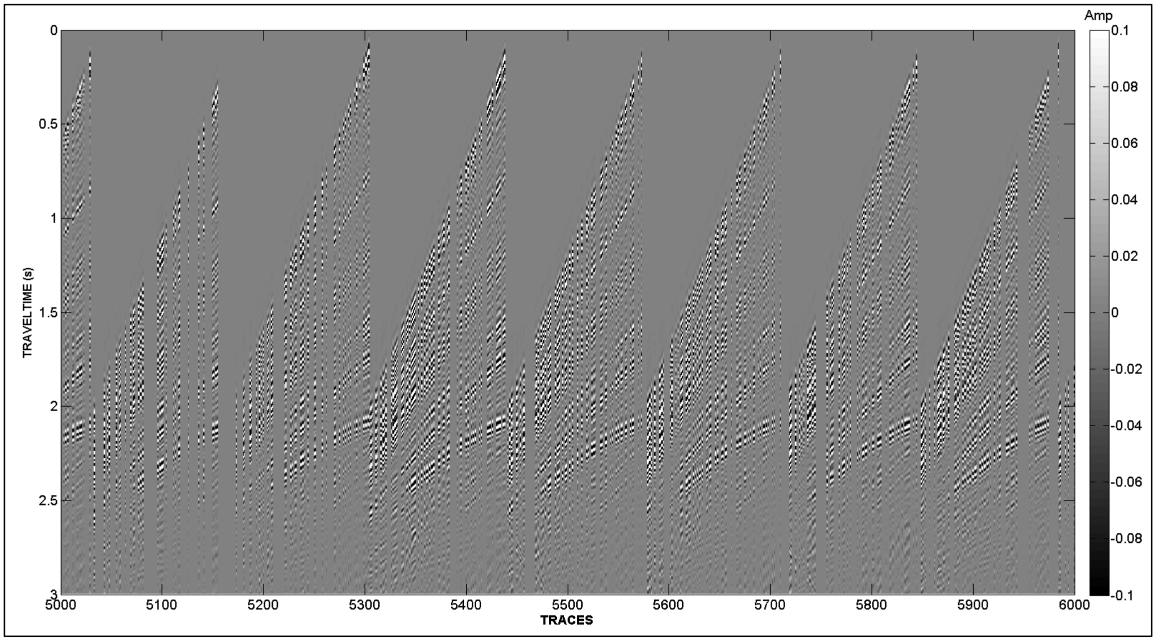

Figure C14 . Representative common shot gathers, $\mathbf{d_0}$, from the decimated Marmousi model, corresponding to figure C2.

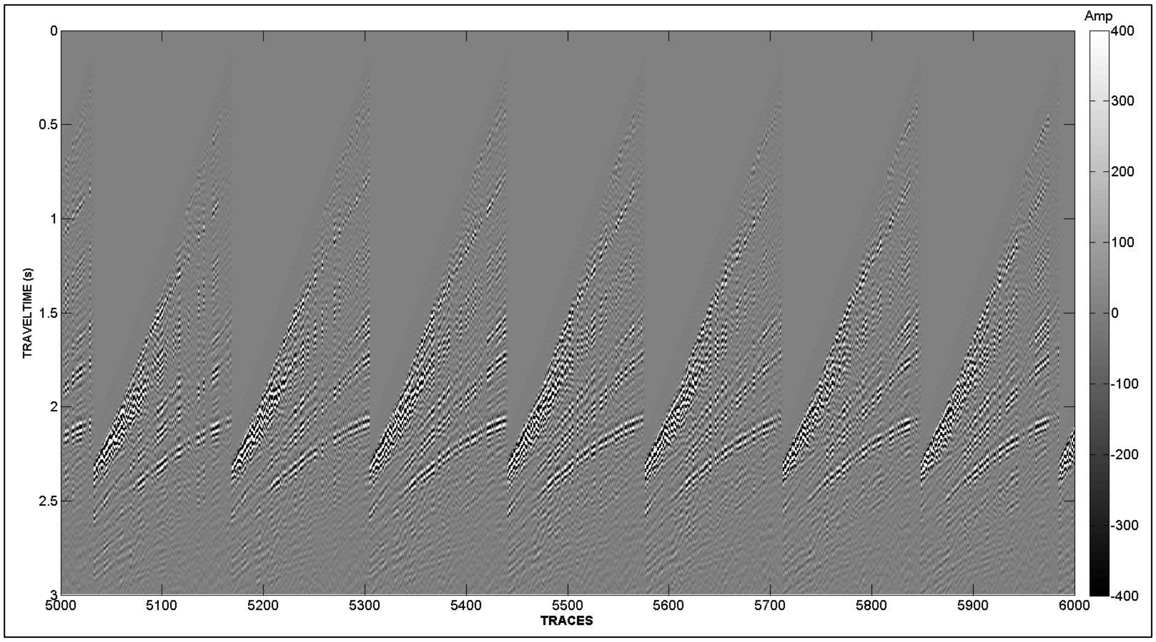

Figure C15. Predicted (modeled) common shot gathers, **d**, from the conventionally migrated vector, **m**. The gaps have not been completely interpolated.

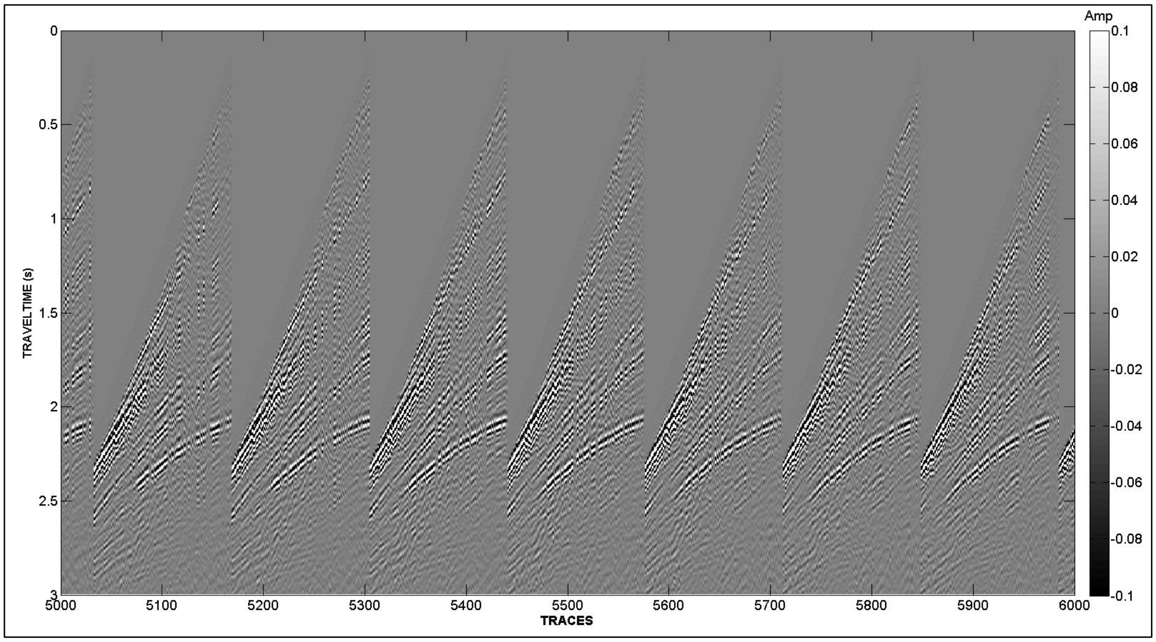

Figure C16. Predicted (modeled) common shot gathers, **d**, from the unconstrained LSM migrated vector, **m**. Note that the gaps in **d** still persist.

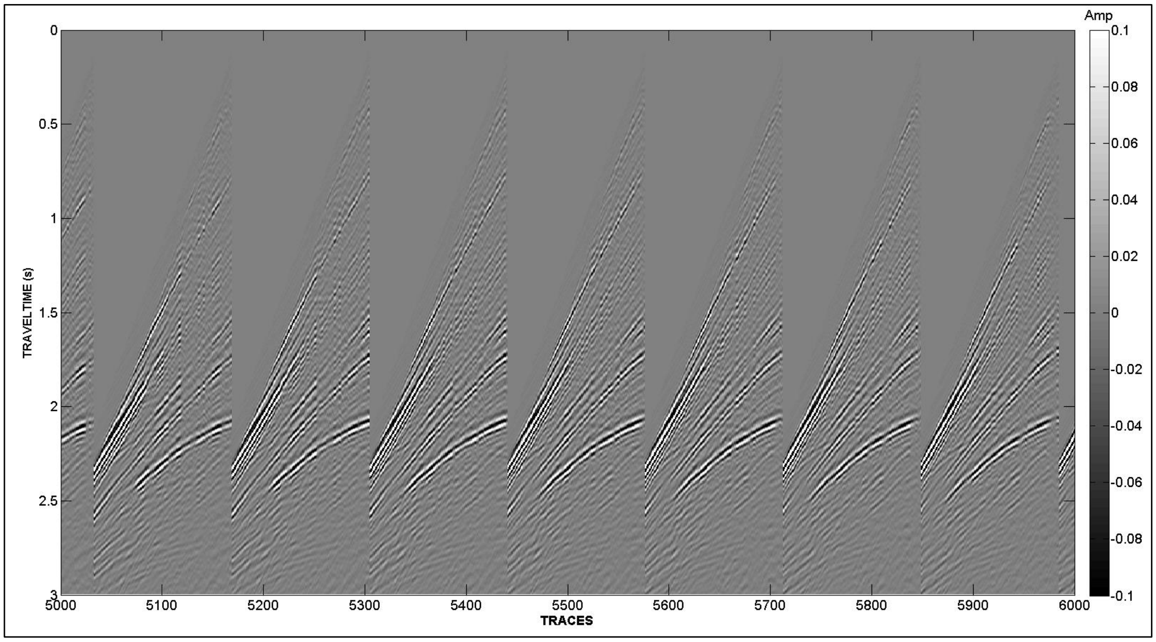

Figure C17. Predicted (modeled) common shot gathers, **d**, from the constrained LSM migrated vector **m**. Now most of the gaps are healed.

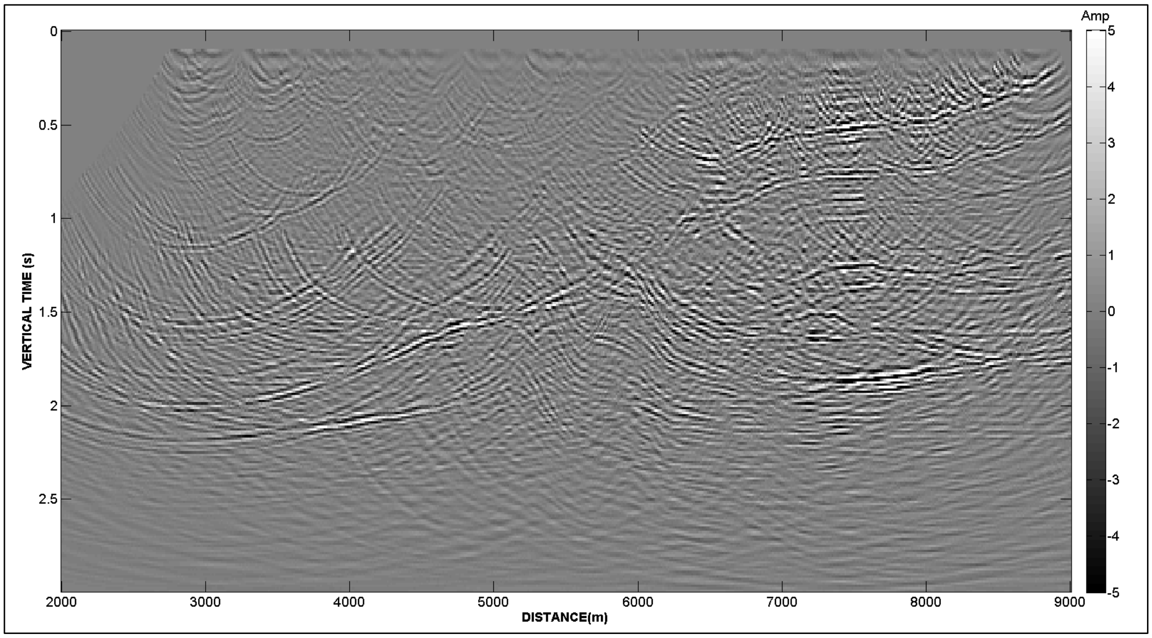

Figure C18. Common-offset gather, **m**, at *h* = 250 m computed from the decimated dataset for the Marmousi model using conventional migration. Compare to Figure C6.

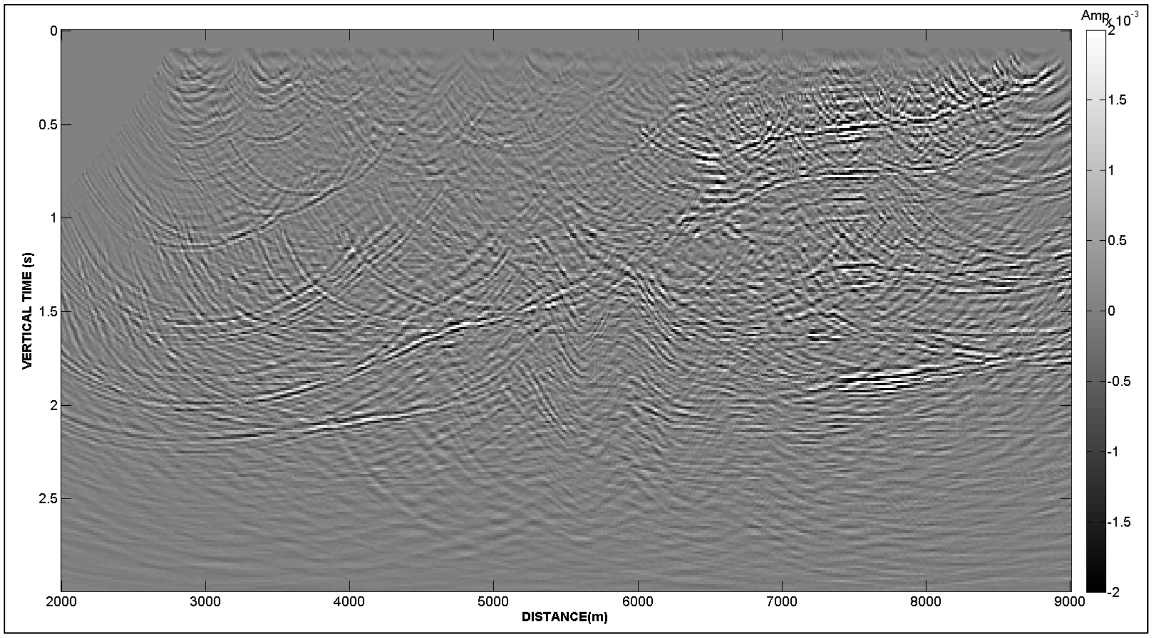

Figure C19. Common-offset gather, **m**, at *h* = 250 m computed from the decimated dataset for the Marmousi model using unconstrained LSM. Compare to Figure C7.

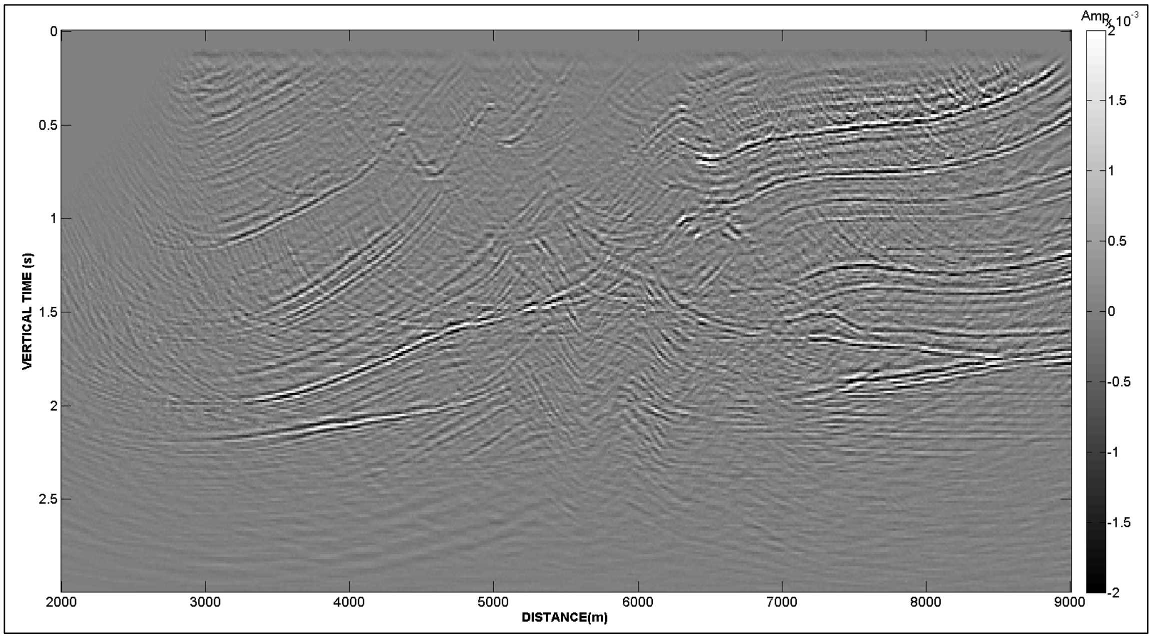

Figure C20. Common-offset gather, **m**, at *h* = 250 m computed from the decimated dataset for the Marmousi model using constrained LSM. Most of the aliasing artifacts have been suppressed and the continuity of the reflectors was notably improved. Compare to Figure C8.

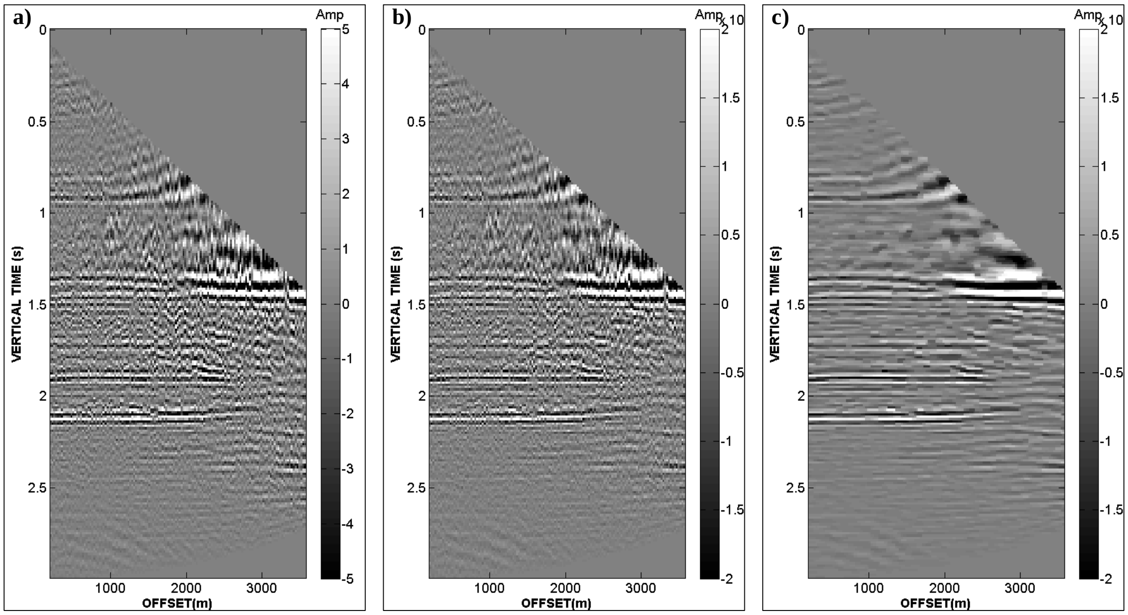

Figure C21. Common reflection point gathers, **m**, at *x* = 3750 m computed from the decimated dataset using (a) Conventional migration, (b) Unconstrained LSM, and (c) Constrained LSM.

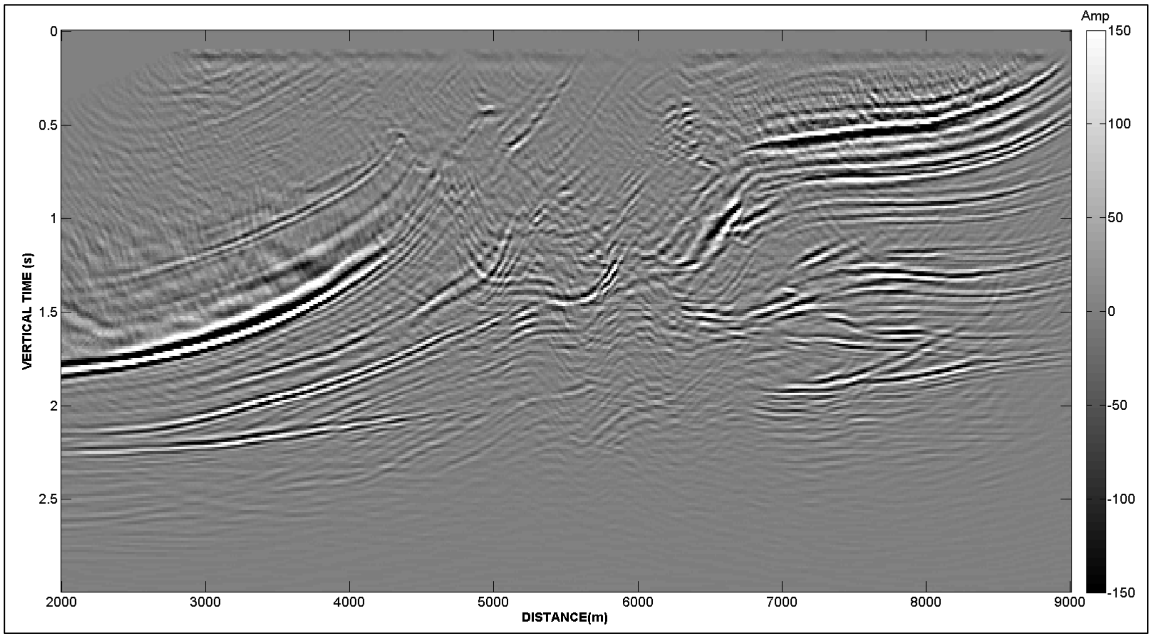

Figure C22. Stacked image of **m** over all offsets for the Marmousi model computed from the decimated dataset using conventional migration.

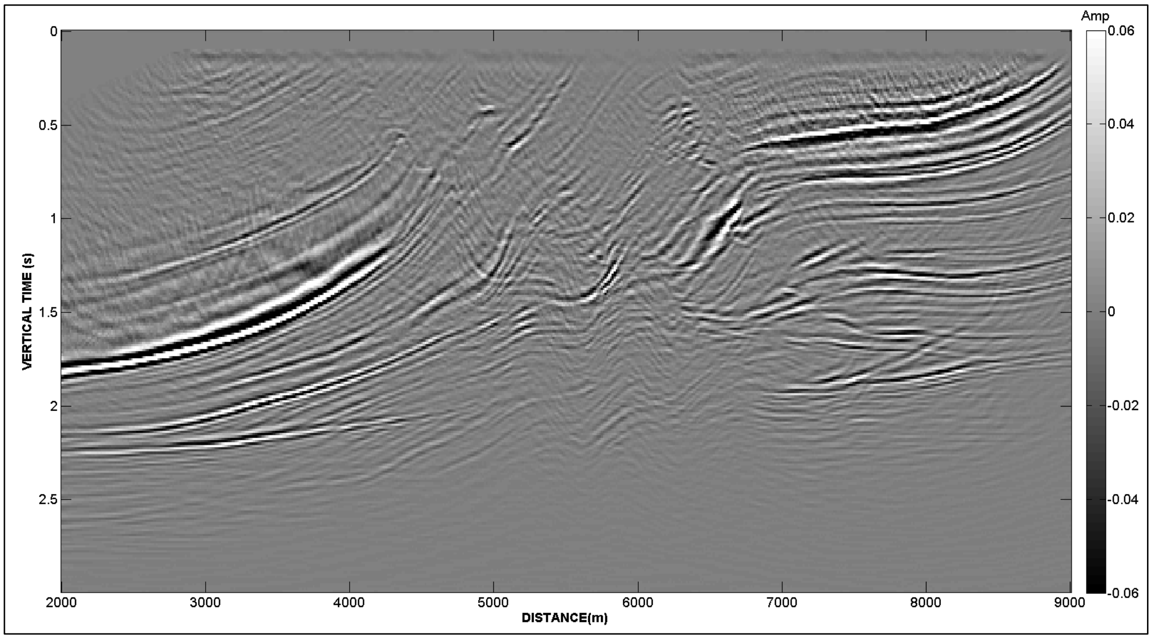

Figure C23. Stacked image of **m** over all offsets for the Marmousi model computed from the decimated dataset using unconstrained LSM.

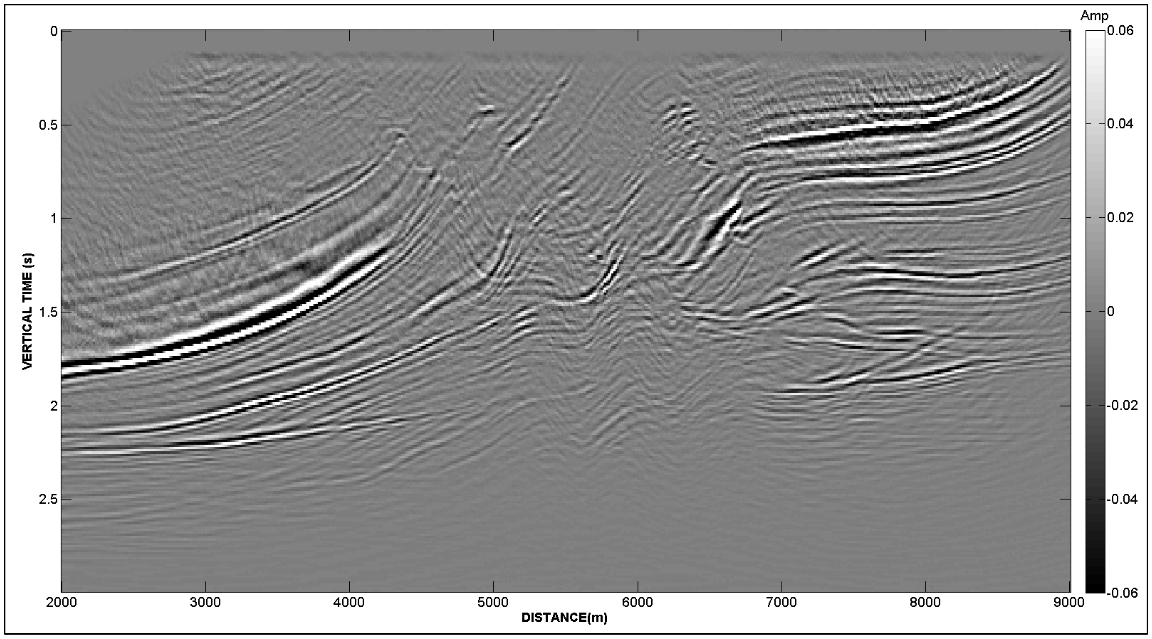

Figure C24. Stacked image of **m** over all offsets for the Marmousi model computed from the decimated dataset using constrained LSM.

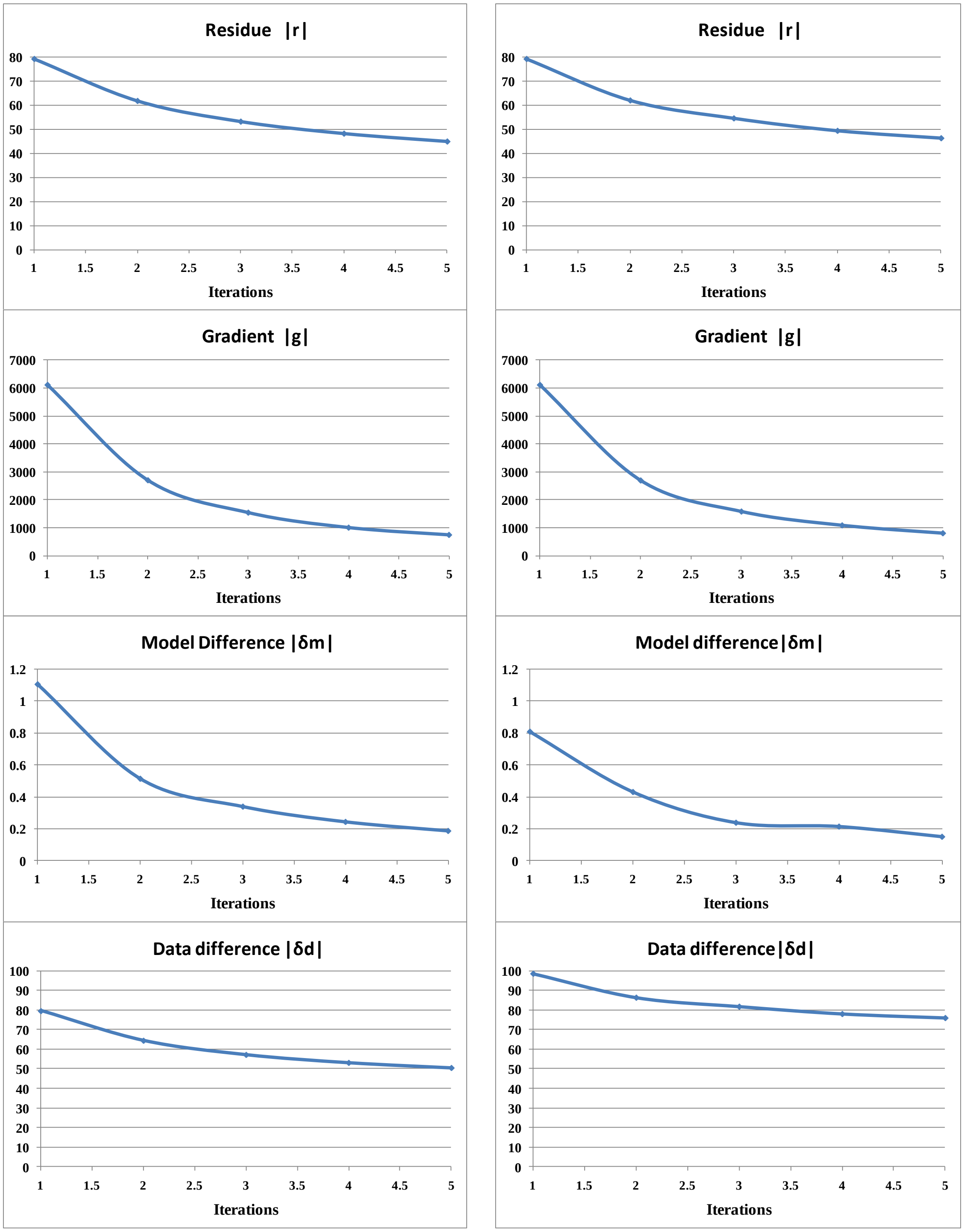

Figure C25. Behavior of the residual, the gradient, the model difference and the data difference with unconstrained and constrained LSM computed from the decimated dataset of the Marmousi model. The first three plots look very similar, with just subtle changes. In contrast, note that the data difference begins and asymptotically converges at higher values in constrained LSM. The aliasing artifacts (which contribute with the reconstruction of the original data) provide a better fit, compared to the constrained LSM predicted data.

APPENDIX D: Hess salt model

Densely sampled input data

The Hess dataset consists of 360 shots spaced at 200 ft. There are 504 traces per shot, spaced at 40 ft, resulting in 156047 live traces. Each trace is 8 s in length and sampled every 4 ms, for a total of 2000 samples per trace. I decimated the traces to a spacing of 80 ft to accelerate the computation. The velocity and anisotropy models have 1501 vertical samples and 3617 horizontal samples, spatially sampled every 20 ft. The considerable size of the prestack data required the computation to be performed in blocks of data, migrating traces which correspond to offset intervals defined for a given block, and applying the overall method before passing to the next block. To perform the Hess model computations I split the data into eight blocks. The first block corresponding to the near offsets exhibited a lack of convergence, producing undesirable noise in the final sections. The reason seems to be the presence of gaining inaccuracies that make the modeled data differ from the original data, which greater effect in the near offsets. Hence, I repeated the calculations excluding the near offset traces. Unfortunately, this sacrifices the imaging of the very shallow reflectors.

Figure D1 shows the original velocity model while Figure D2 shows a detail of the corresponding shot gathers. Note the strength of the direct wave, ultimately excluded from the calculations by the muting function, as well as the multiple reflections which will be mismigrated. The original data and the predicted data figures were gained using a time function of $t^{1.5}$ for better display. Figures D3-D5 show the predicted images for conventional migration, unconstrained LSM, and constrained LSM respectively, for five iterations. The predicted data obtained through conventional migration show an anomalously strong reflection corresponding to the top of salt at about 2.3 s (black arrows) for medium offset and background noise, which may be remnants the direct waves measured at the far offset. In contrast, unconstrained LSM suppresses the anomalous reflection at 2.3 s, restores the amplitude of the salt reflection and attenuates the noise caused by direct waves at the far offset. Constrained LSM cleans the background noise which yields a better visualization of the seismic reflectors, and attenuates the steeply dipping multiple events that are not flat in the common-reflection point gathers. Application of the constraint function (median filtering) in every block of data produced edge effects in the data. Similarly to the previous datasets, the order of magnitude of the amplitude and its distribution is restored by LSM.

Figures D6-D8 show a common-offset gather at h = 4000 ft for the three processes, that have been gained in vertical time by τ^2 for better visualization. Conventional migration shows the influence of aliasing noise and multiple reflections. Some of the multiples are attenuated by unconstrained LSM, mainly those present in the salt body and near the base, although not in their entire extension. The small thin bodies in the velocity model (Figure D1), which are observed between x = 30000 ft and x = 40000 ft, t = 4.5 s and t = 5.5s (z = 15000 ft and z = 20000 ft in the velocity model) (presumably the drilling target), are apparently better imaged in the conventionally migrated image. Some medium frequency noise is introduced in the background. In contrast, constrained LSM greatly attenuates the aliasing artifacts and the background noise, allowing the interpretation of the common-offset section. The high frequency content, often lost during the stacking process allows us to interpret the target reflectors more easily than in the full stack sections.

Figure D9 shows a common reflection point gather corresponding to x = 30000 ft for the three processes, gained as in the previous sections. Conventional migration shows the flat primaries reflections and the overcorrected long-period multiples, which correspond to smaller velocities. The short-period multiples (e.g. peg-leg multiples) closely follow the primaries, which make them difficult to distinguish. The overall image is obscured by the presence of aliased noise in the background, giving the checkerboard appearance. Unconstrained LSM slightly attenuates such noise and shifts the higher amplitudes from far offsets to medium offsets. Constrained LSM (right) significantly suppresses the aliased noise, revealing previously unseen reflectors. Similar to the predicted data, the artificial vertical divisions constitute a side effect of median filtering boundaries when applied to blocks of data. Some spurious flat events arise as well, which negatively impacts the final stack section.

Figures D10-D12 show the final stacked sections, gained vertical time by τ^2. The conventionally migrated section is affected by the multiples that sometimes exhibit amplitudes as high as the primaries. Unconstrained LSM partially attenuates some multiples and shows a cleaner background. However, noise is introduced around the target area below 4.5 s. The constrained LSM introduces low to medium frequency artifacts product of the spurious flat events.

Finally, Figure D13 shows the decrease of the residue, the gradient, the model difference and the data difference as a function of the iteration number. In this case I show the eight curves corresponding to the blocks in which the data traces were divided.

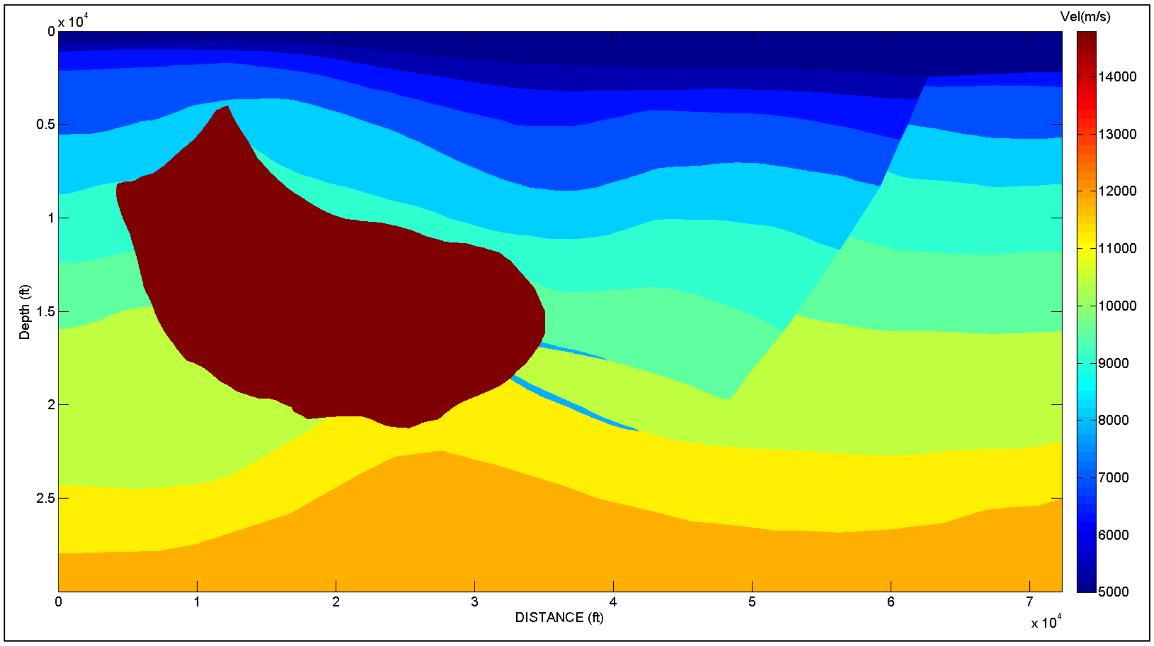

Figure D1. Hess salt velocity depth model.

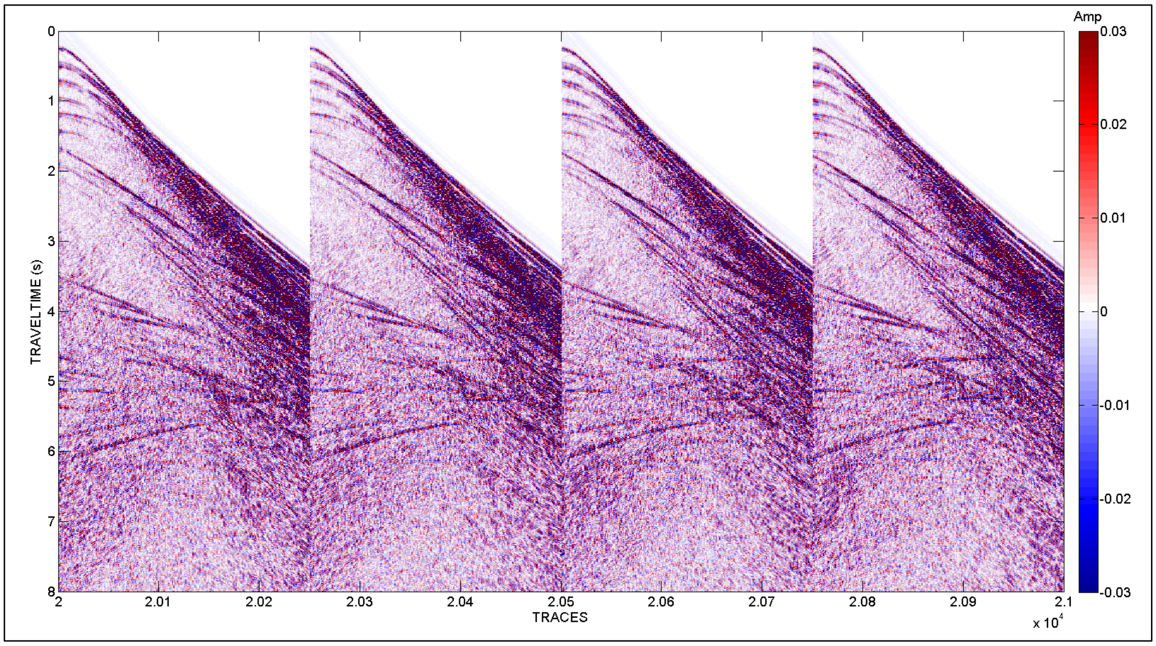

Figure D2. Representative shot gathers, $\mathbf{d}_0$, generated for the Hess salt model using a finite difference solution of the scalar equation.

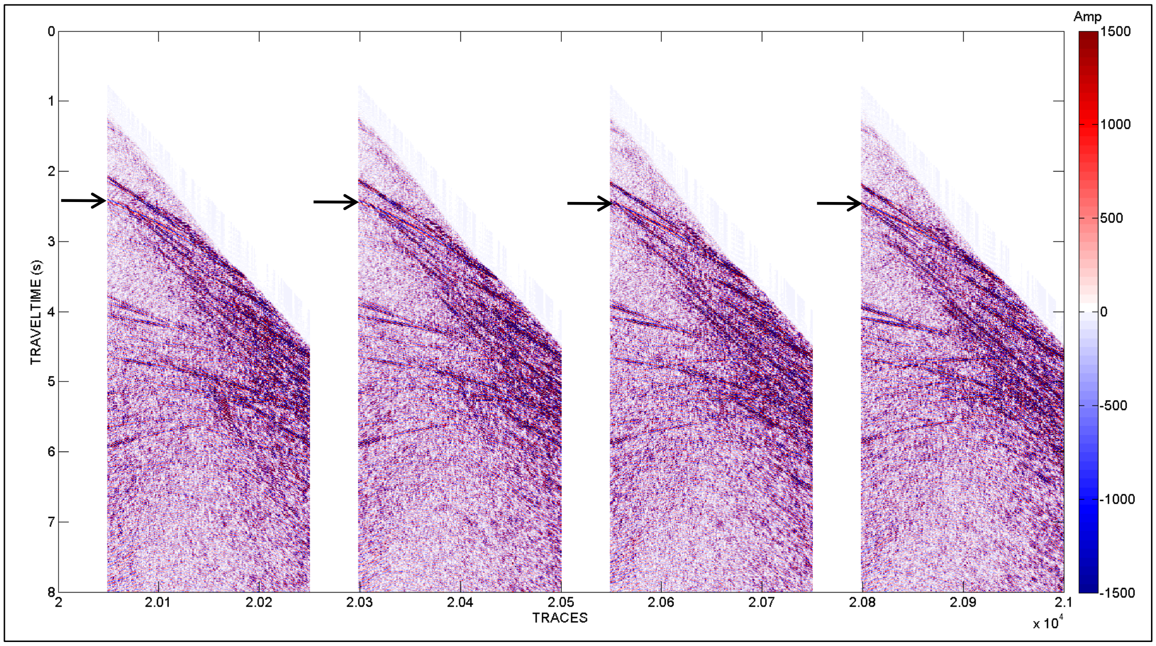

Figure D3. Predicted (modeled) common shot gathers, **d**, from the conventionally migrated vector, **m**. Note the anomalous reflector indicated by the black arrow, virtually absent in the original data, possibly a multiple.

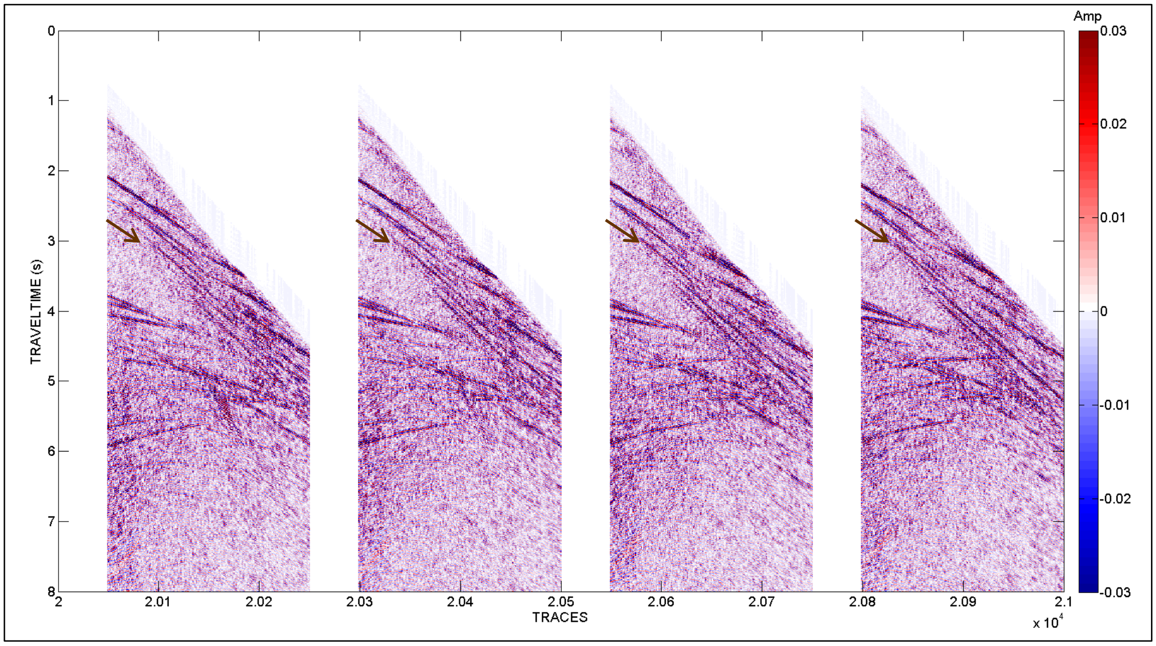

Figure D4. Predicted (modeled) common shot gathers, **d**, computed from the unconstrained LSM vector, **m**. Note that the anomalous reflector is now attenuated. Brown arrows indicate steeply dipping multiples.

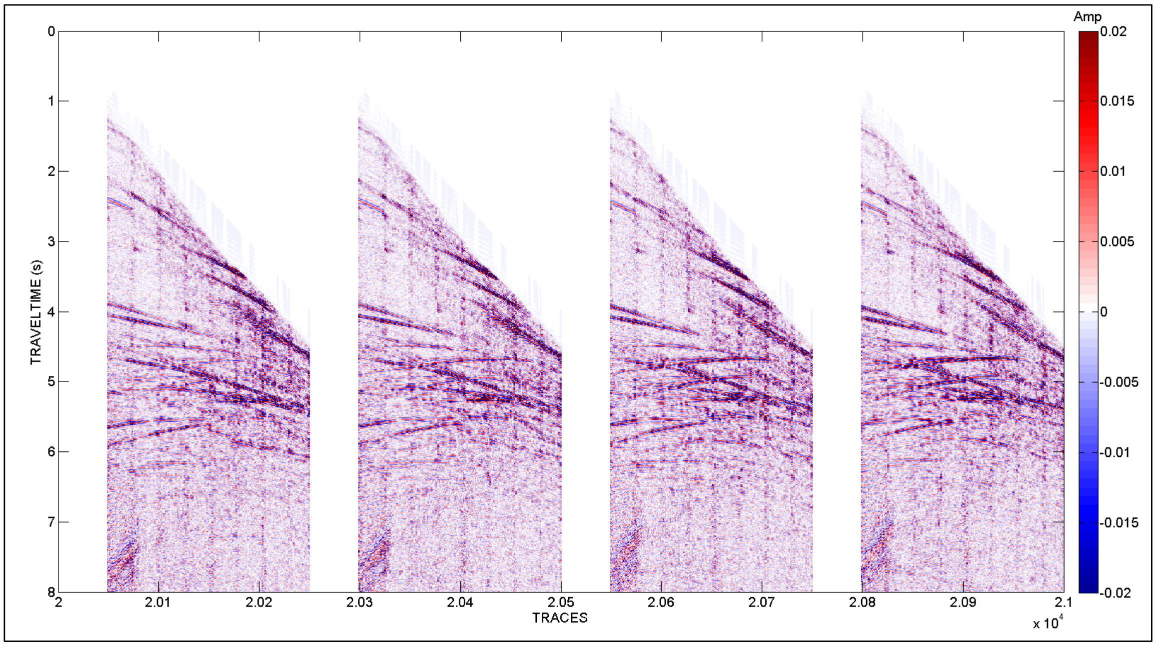

Figure D5. Predicted (modeled) common shot gathers, **d**, computed from the constrained LSM vector, **m**. Note the steeply dipping multiples have been attenuated.

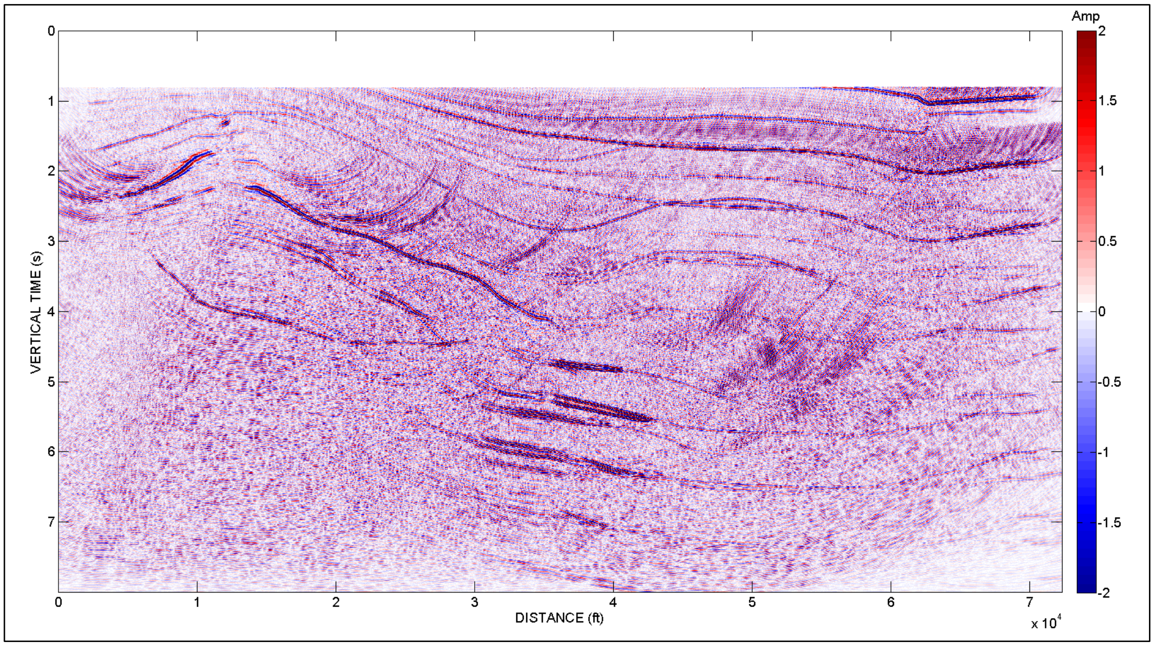

Figure D6. Common offset gather, **m**, at *h* = 4000 ft computed for the Hess salt model using conventional migration.

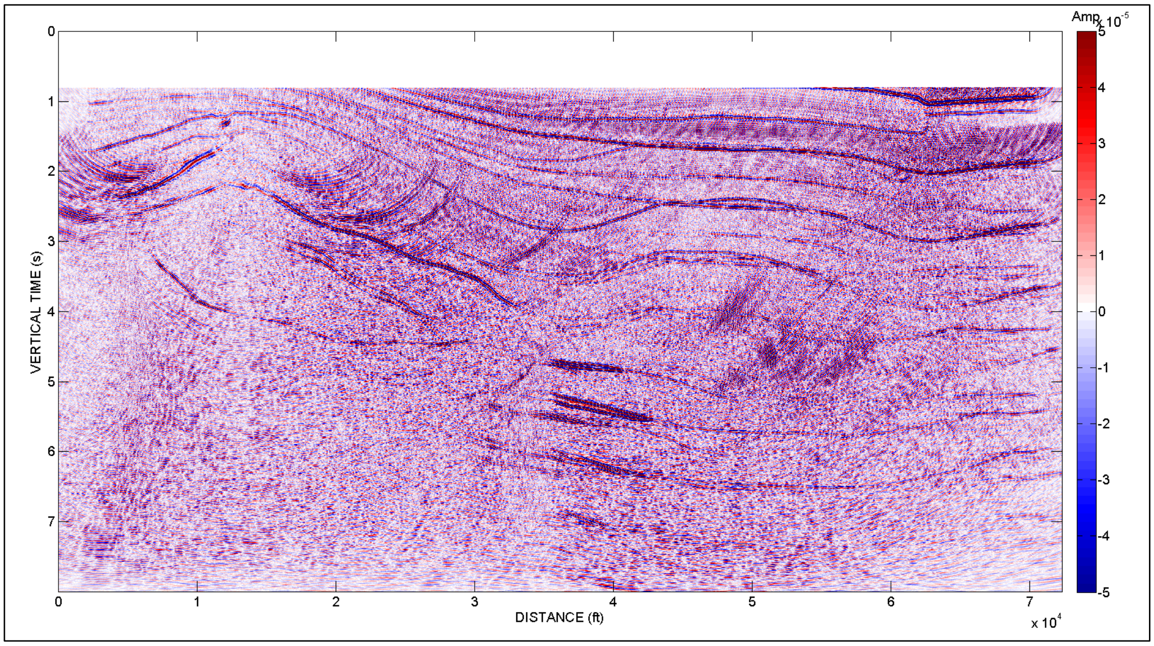

Figure D7. Common offset gather, **m**, at *h* = 4000 ft computed for the Hess salt model using unconstrained LSM.

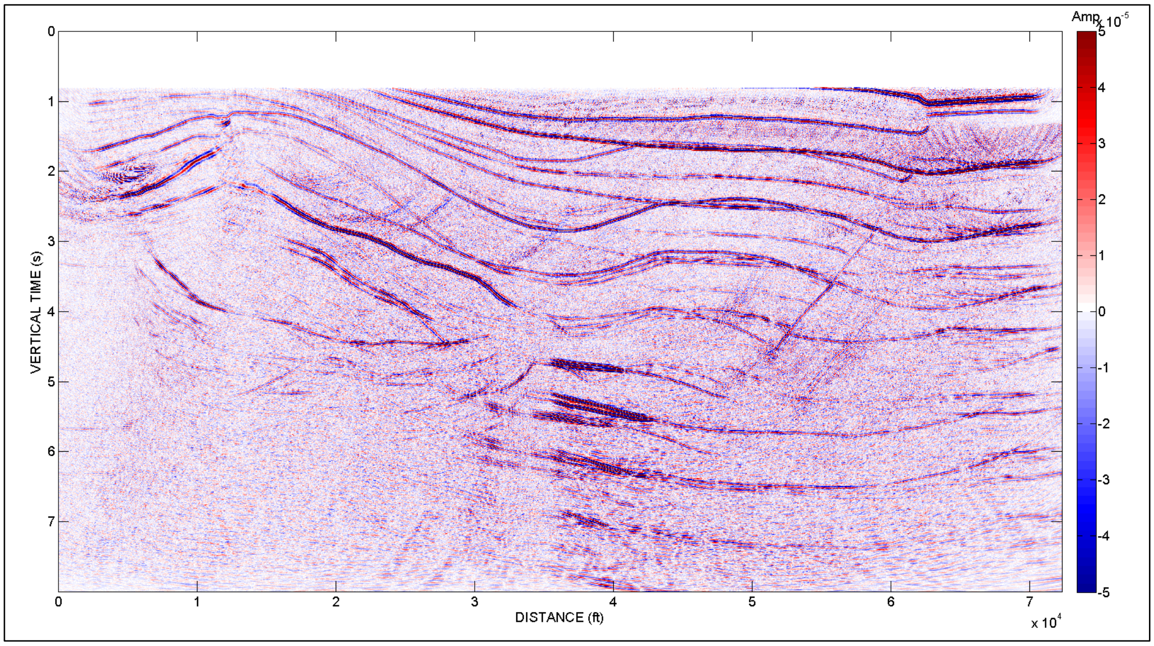

Figure D8. Common offset gather, **m**, at *h* = 4000 ft computed for the Hess salt model using constrained LSM. Note how the target zone and fault plane reflections can be interpreted even better than in the full stack sections because of the higher frequency content, normally lost during the stacking process for inaccurate velocity models.

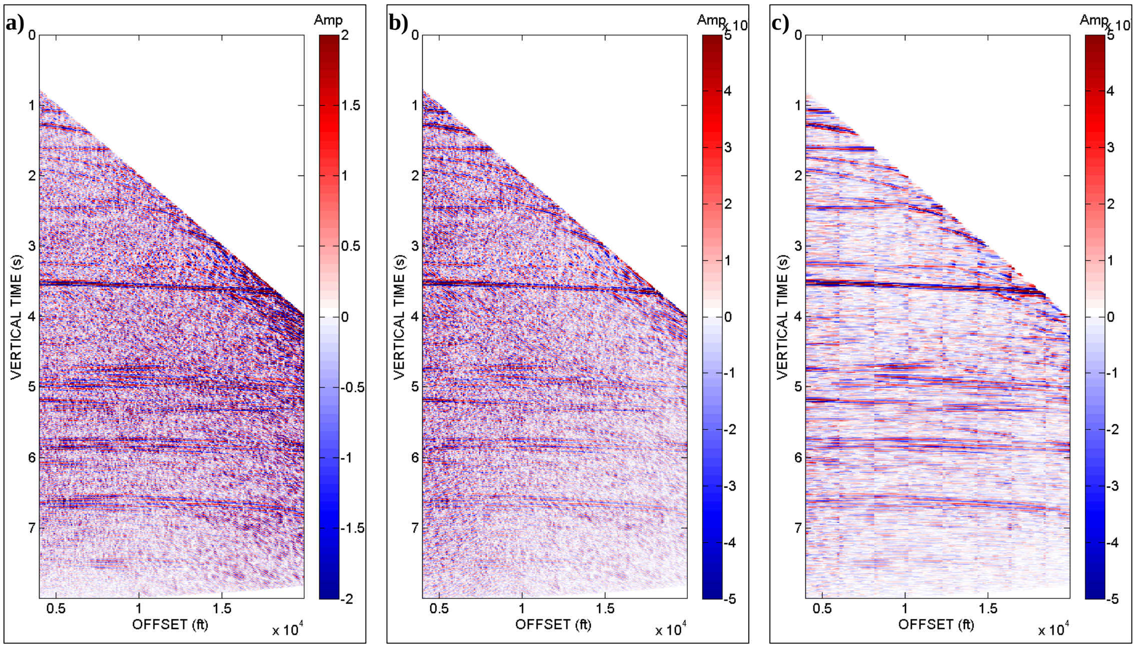

Figure D9. Common reflection point gathers, **m**, at *x* = 30000 ft computed using (a) Conventional migration, (b) Unconstrained LSM, and (c) Constrained LSM.

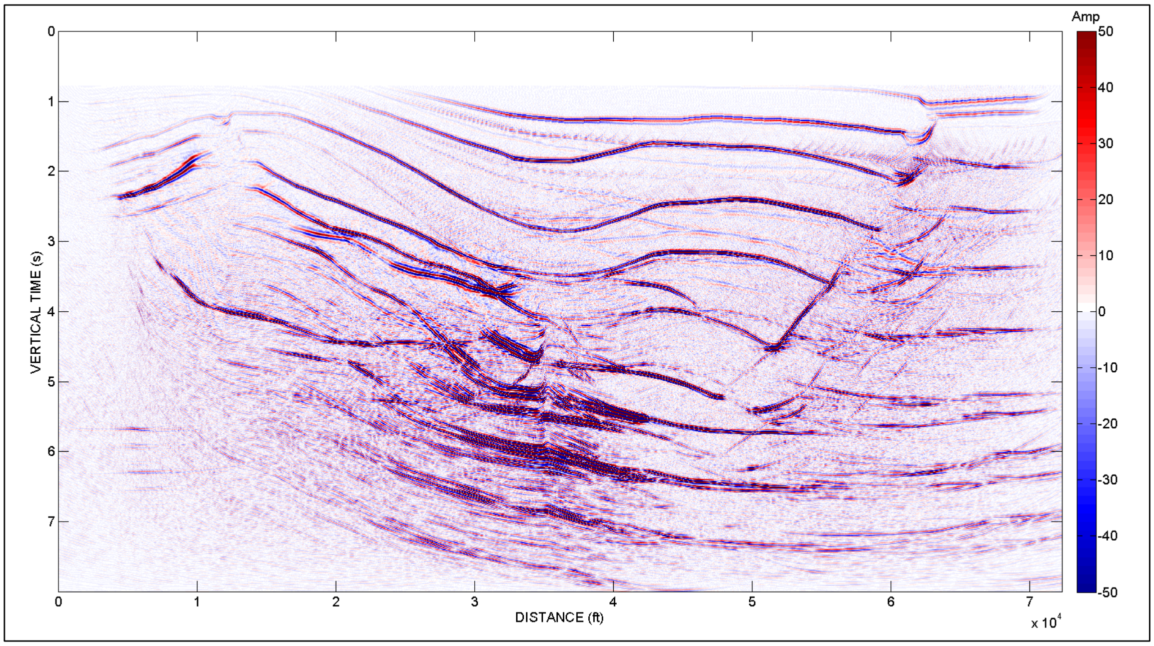

Figure D10. Stacked image of **m** over all offsets for the Hess salt model using conventional migration.

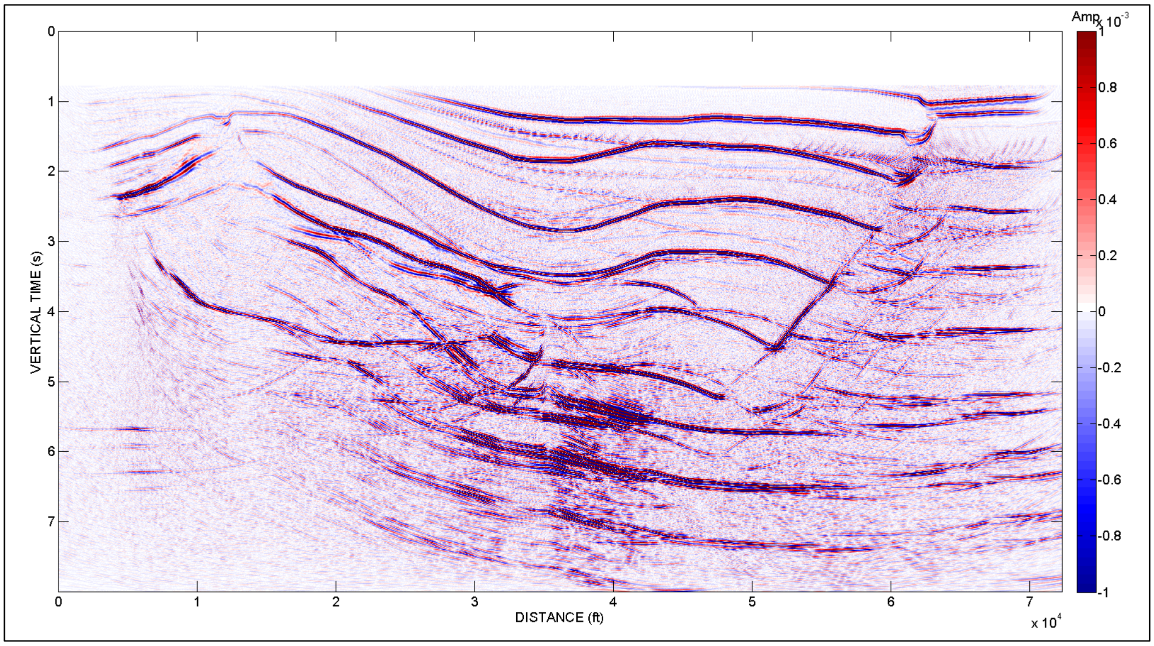

Figure D11. Stacked image of **m** over all offsets for the Hess salt model using unconstrained LSM. Note the attenuation of multiples inside the salt body and some background noise.

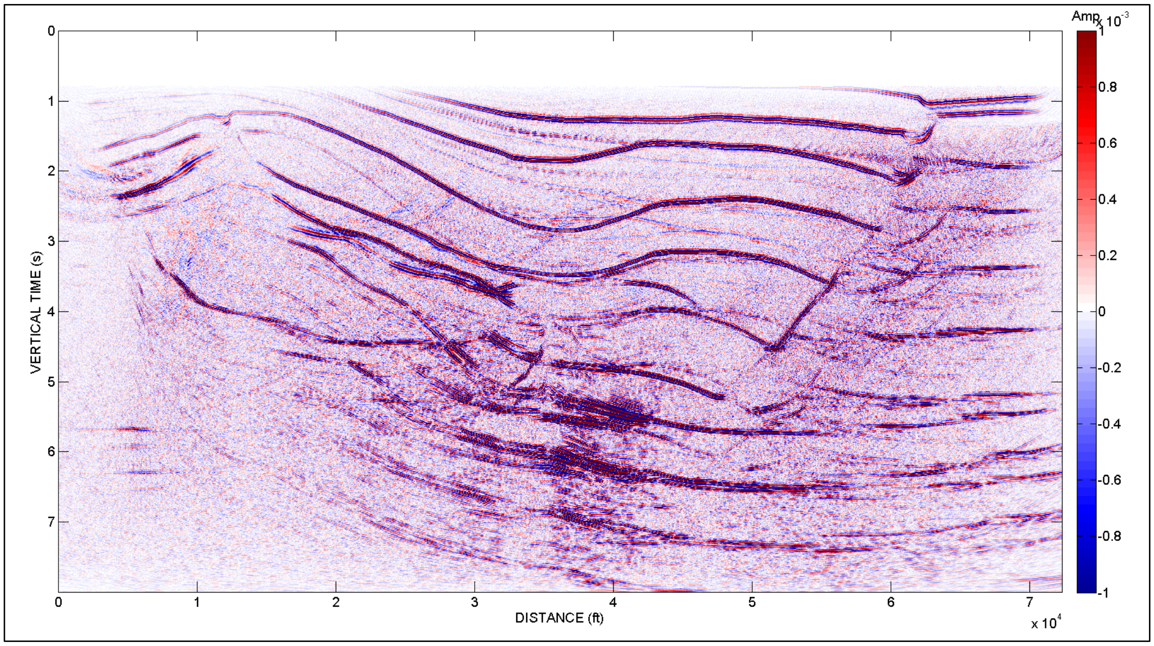

Figure D12. Stacked image of **m** over all offsets for the Hess salt model using constrained LSM. Note the low to medium background noise introduced by spurious flat events in the common reflection point gathers (Figure D9c).

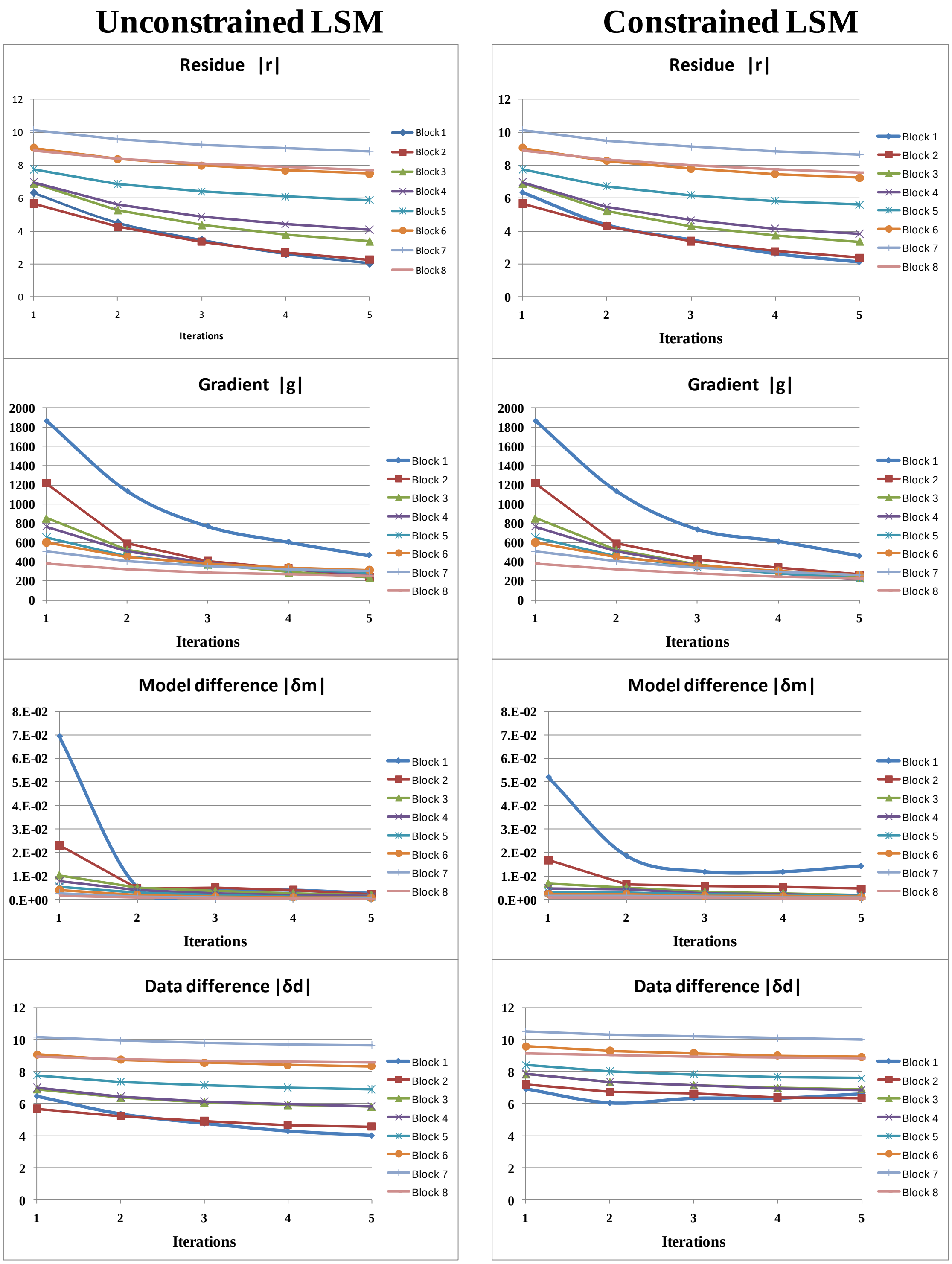

Figure D13. Behavior of the residual, the gradient, the model difference and the data difference with unconstrained and constrained LSM for the Hess salt model. Note that the residual and the gradient converge just slightly faster in this case using constrained LSM. It is interesting to observe that the behavior of the gradient and the model difference of first block departs from the main trend of the other blocks, perhaps because it still includes traces of the numerical problem that prevented the convergence of the near offset. Data difference slightly reduces after the major change from the zero iteration (not plotted) and the first iteration.

Decimated input data

Figure D14 shows representative shot gathers from the decimated dataset, obtained after randomly killing two thirds of the traces. The seismic reflectors become difficult to discern. Figures D15-D17 show the predicted data after conventional migration, unconstrained LSM and constrained LSM, respectively, after five iterations. Conventional migration artificially enhances the amplitude of the top of salt (black arrows), as occurred in the undecimated case. Aliasing artifacts derived from the lack of regular sampling generate background noise and prevent the reconstruction of the data in the gaps. Unconstrained LSM still presents the problem of the aliasing artifacts and the gaps, but succeeds in restoring the amplitudes of the dataset and the anomaly on top of the salt. Constrained LSM yields a cleaner reconstruction with better continuity of the seismic reflectors, with the side effect of the constraint function in the blocks of traces.

Figures D18-D20 show the medium common-offset gather at h = 4000 ft for the three processes. Conventional migration shows the severe effects of the aliasing artifacts due to the irregular sampling, which makes many seismic reflections indiscernible and easy to be confused with multiples. Unconstrained LSM partially attenuates some multiples in the salt and body improves the visibility of some weak reflectors, although some background noise is introduced and some detail at the target area is lost. Constrained LSM greatly reduces the migration artifacts and the section becomes interpretable, with the primary reflections easier to differentiate from the multiples. Similar to the undecimated case, the interpretation of the target reflectors is easier than in the final stack sections.

Figure D21 show the common reflection point gather at x = 30000 ft for the three processes. The main difference with the undecimated case is the increase of aliasing noise in the background, making more difficult the interpretation of the reflectors with both conventional migration and unconstrained LSM. The latter shows the same shifting of amplitudes from far offset to medium offset. Using constrained LSM the noise is attenuated and the reflectors can be identified, but at the cost of introducing spurious flat events.

Figures D22-D24 show the final migration stack. Conventional migration shows background noise but the aliasing artifacts are greatly attenuated. Unconstrained LSM attenuates the background noise and better distributes the seismic amplitudes. Constrained LSM obtains similar results in the amplitudes, but noise derived from the spurious flat events is introduced.

Finally, Figure D25 shows the decrease of the residue, the gradient, the model difference and the data difference as a function of the iteration number for all the data blocks.

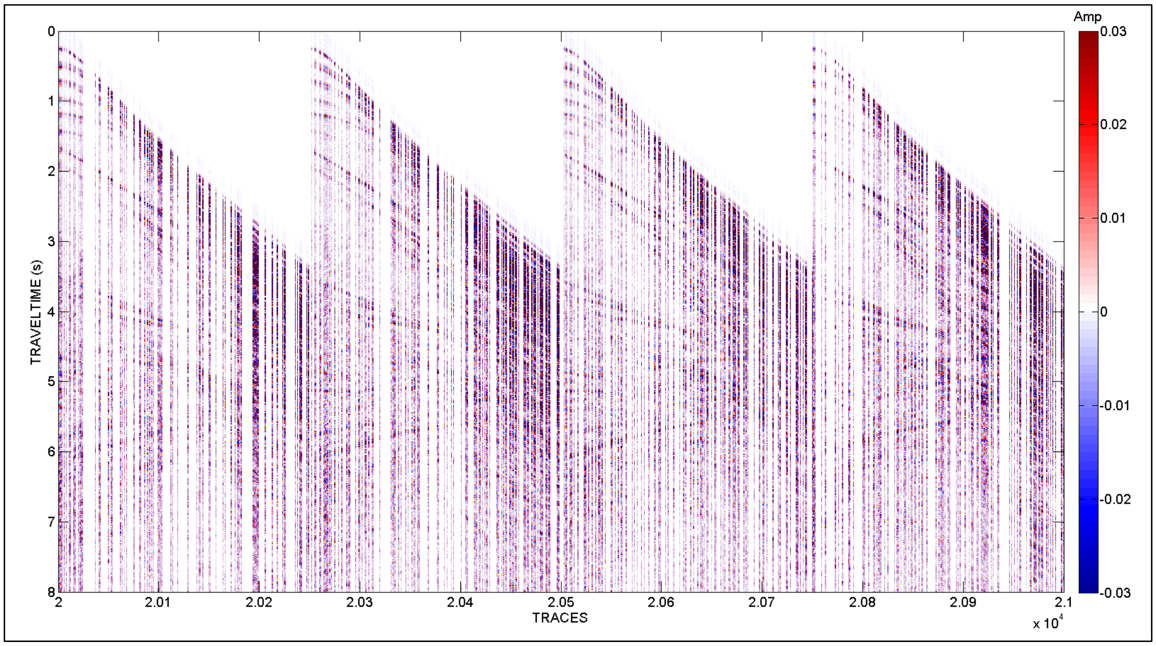

Figure D14. Representative common shot gathers from the decimated Hess salt model corresponding to Figure D2.

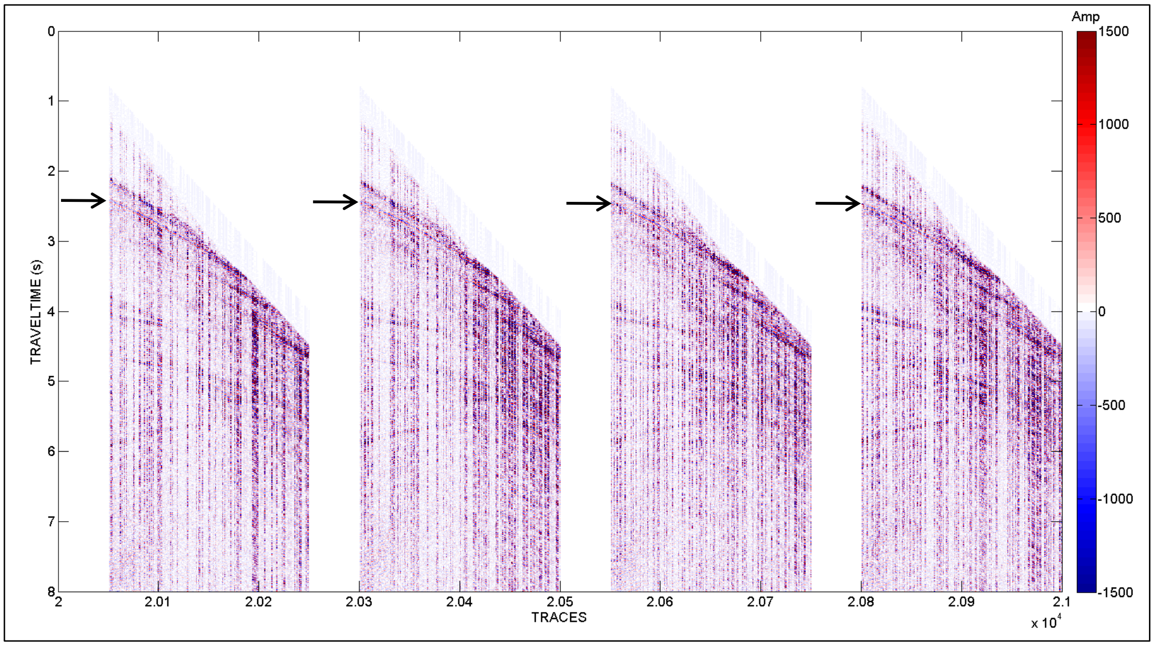

Figure D15. Predicted (modeled) common shot gathers, **d**, from the conventionally migrated vector, **m**. Note the anomalous reflector indicated by the black arrow, as in the undecimated case.

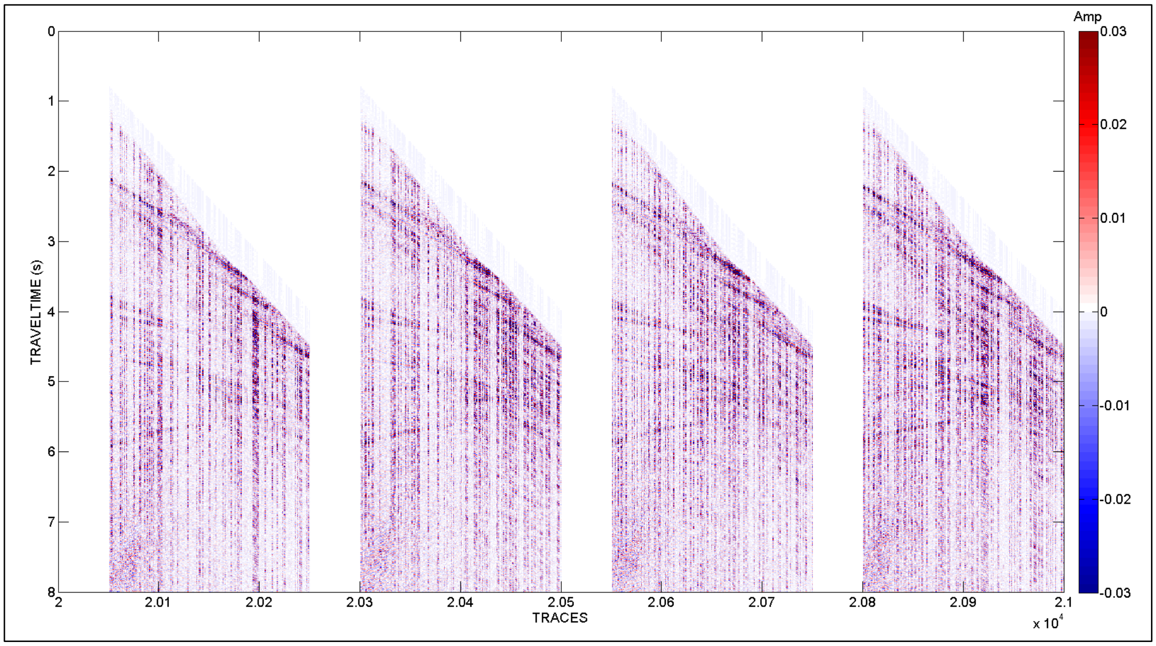

Figure D16. Hess VTI dataset, decimated: Predicted data after unconstrained LSM. The anomalous reflector was attenuated and the frequencies redistributed, but the gaps persist.

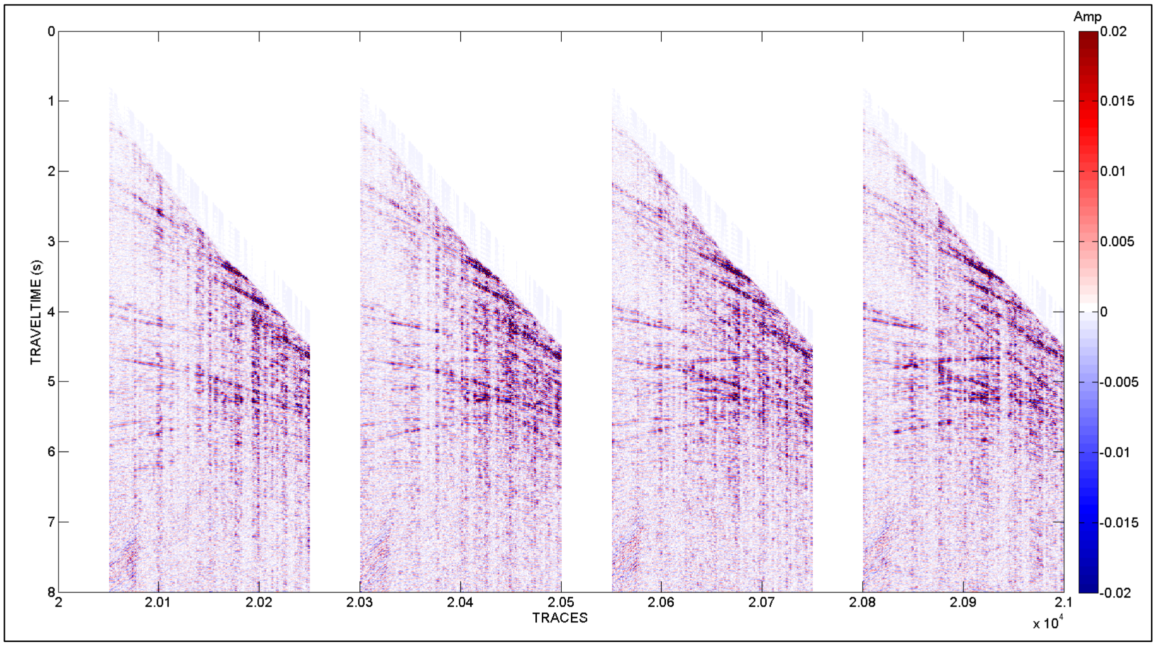

Figure D17. Hess VTI dataset, decimated: Predicted data after constrained LSM. The gaps have been almost completely filled. Note the artifacts created by the edge effects of the constraint function in the blocks of traces.

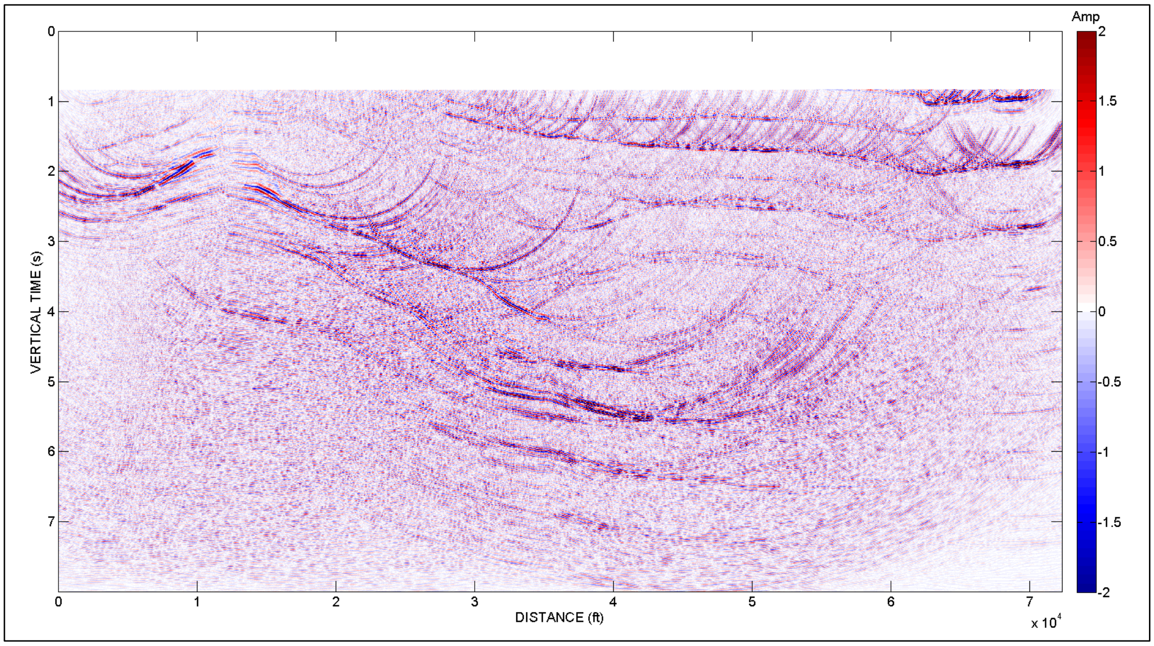

Figure D18. Common offset gather, **m**, at *h* = 4000 ft computed from the decimated dataset for the Hess salt model using conventional migration. Compare to Figure D6.

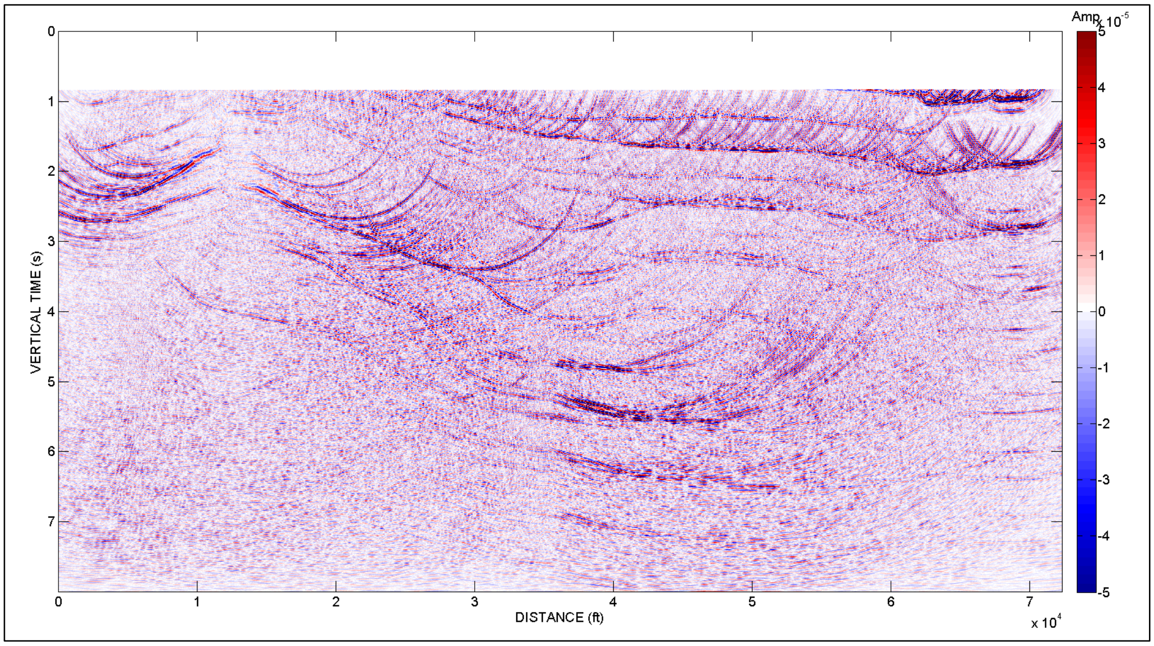

Figure D19. Common offset gather, **m**, at *h* = 4000 ft computed from the decimated dataset for the Hess salt model using unconstrained LSM. Compare to Figure D7.

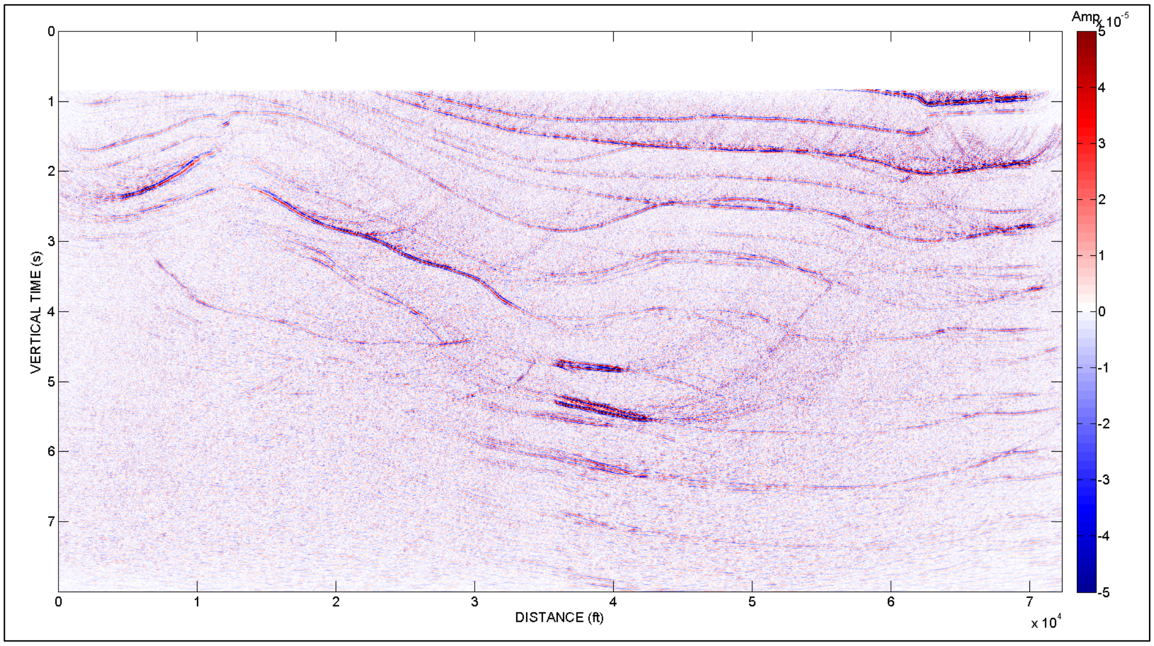

Figure D20. Common offset gather, **m**, at *h* = 4000 ft computed from the decimated dataset for the Hess salt model using unconstrained LSM. Compare to Figure D8. Note how the target zone reflectors can be interpreted even better than in the full stack sections because of the higher frequency content, normally lost during the stacking process.

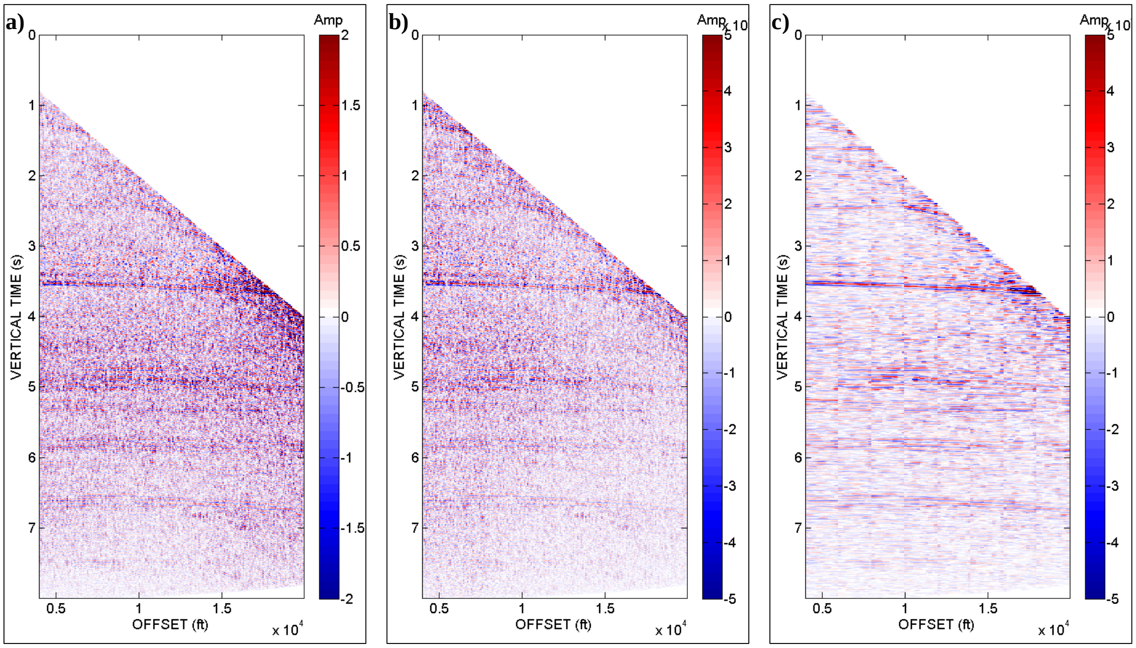

Figure D21. Common reflection point gathers, **m**, at *x* = 30000 ft computed from the decimated dataset using (a) Conventional migration, (b) Unconstrained LSM, and (c) Constrained LSM.

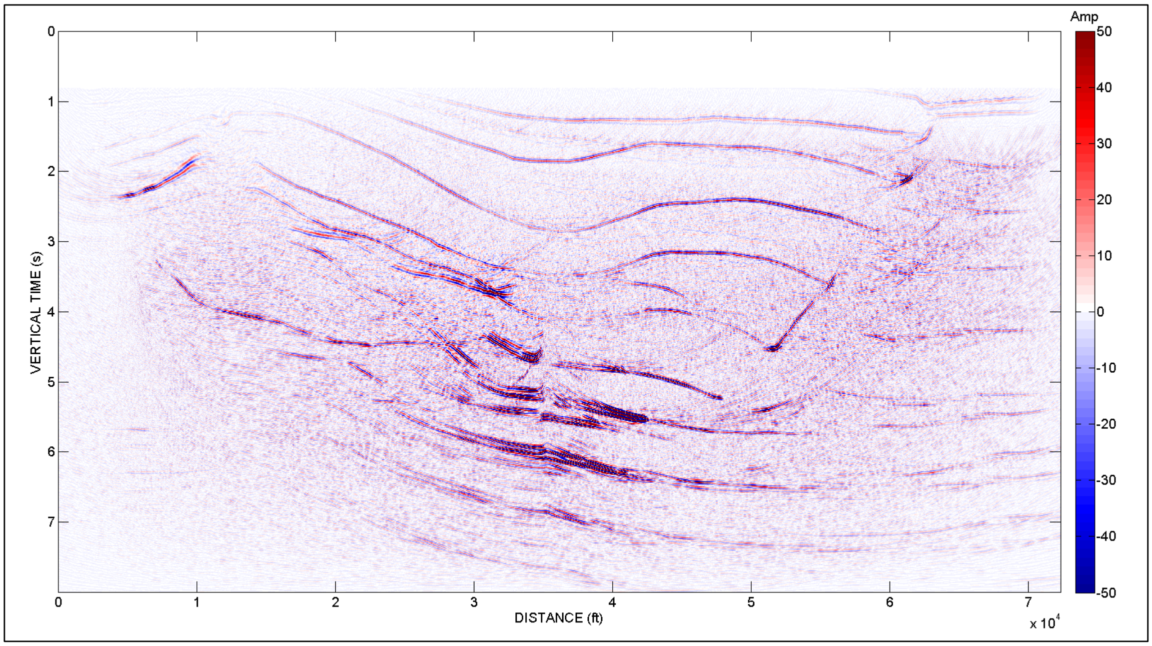

Figure D22. Stacked image of **m** over all offsets for the Hess salt model computed from the decimated dataset using conventional migration.

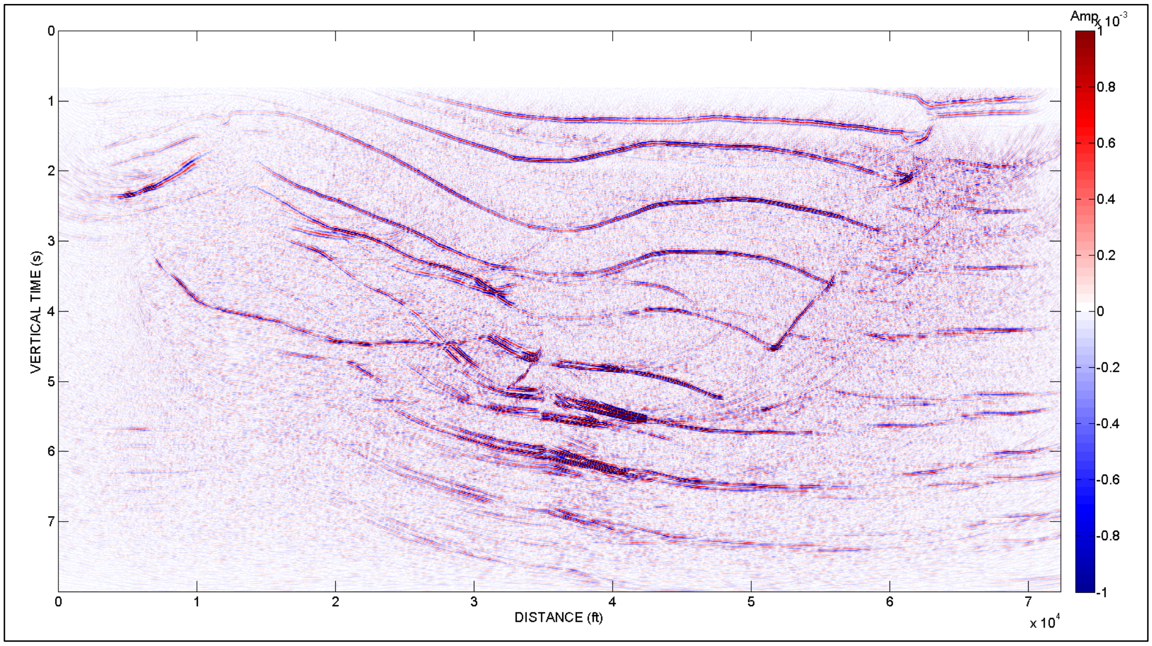

Figure D23. Stacked image of **m** over all offsets for the Hess salt model computed from the decimated dataset using unconstrained LSM.

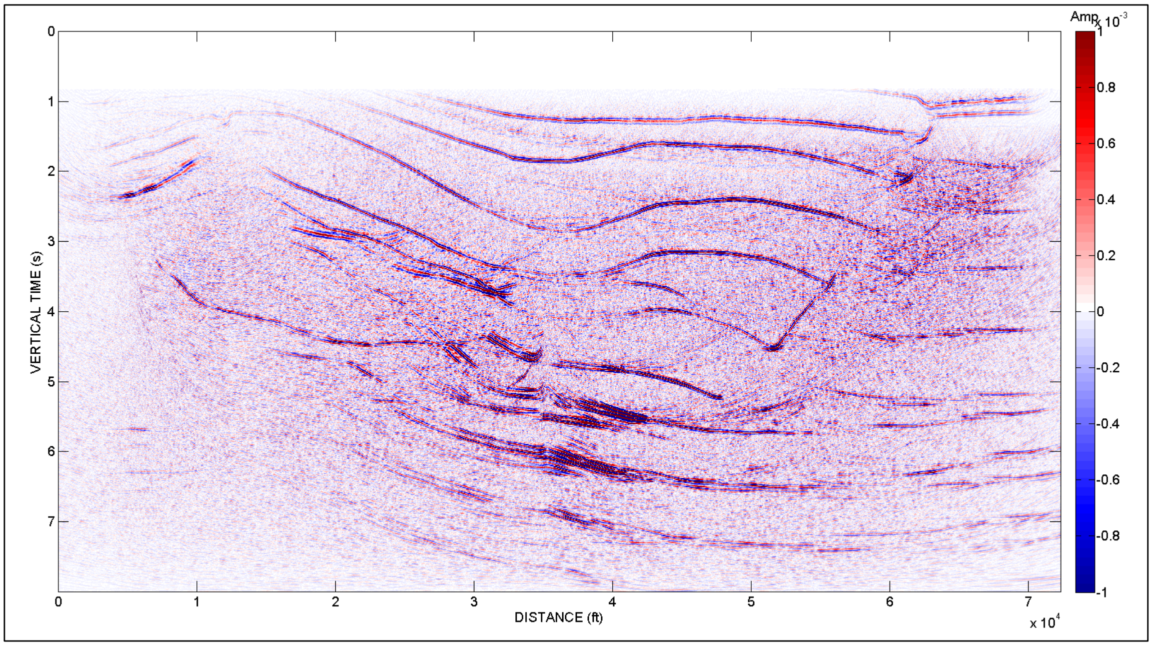

Figure D24. Stacked image of **m** over all offsets for the Hess salt model computed from the decimated dataset using constrained LSM.

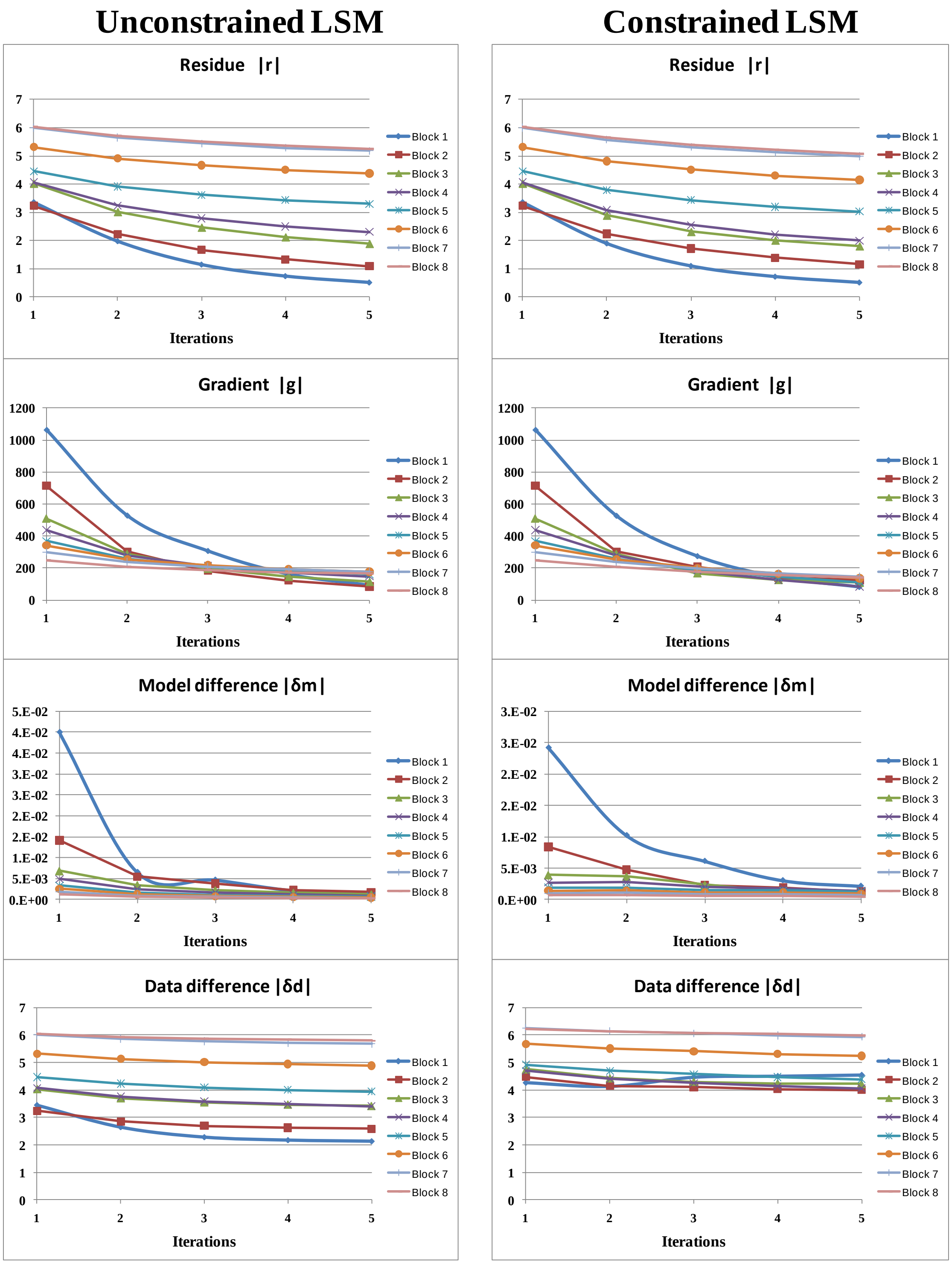

Figure D25. Behavior of the residual, the gradient, the model difference and the data difference with unconstrained and constrained LSM computed from the decimated dataset of the Hess salt model. The plots are similar to the undecimated case, with the same anomalous behavior of the first block.

DISCUSSION OF RESULTS

The results obtained from in the numeral examples using the two-layer model, the anisotropic Marmousi model and the Hess salt model show the benefits and drawbacks of unconstrained and constrained LSM. According to the numerical results, LSM definitely better predicts the input data than conventional migration, eliminating some background noise and other artifacts. In the undecimated cases, unconstrained and constrained LSM yield comparable predictions of data. In the decimated case the continuity is better reconstructed when using constrained LSM. The edge effects in the Hess model are due to an uncentered median filter used as constraint function computed in blocks of common-offset traces. This and other limitations were fixed in the more advance 3D version of CLSM.

In the two-layer model conventional migration shows migration smiles below the real reflector. These artifacts are suppressed by unconstrained LSM. In the undecimated case, constrained LSM attenuated most of the aliased noise. In the decimated case, constrained LSM succeeded in reconstructing the horizontal reflector, whereas conventional migration and unconstrained LSM showed it segmented as semicircles superposition. The Hess salt model shows noticeable re-distribution of seismic amplitudes and partial attenuation of some multiples. In the Marmousi model only marginal changes (other than overall amplitude scaling) are observed comparing conventional migration and unconstrained LSM.

The common reflection point gathers became cleaner with constrained LSM, showing subtle flat events otherwise obscured by the aliasing artifacts. This makes the gathers more suitable for AVO analysis. However, the median filter created false connectivity of events other than seismic reflectors, which I denoted as spurious flat events. They contaminate the final stack sections with low to medium frequency noise. It is worth to mention that the Marmousi model does not exhibit spurious flat events, even in the decimated case. In contrast, the two-layer model and the Hess salt model present important aliasing issues, even in the undecimated case, which gives rise to constructive interference patterns that can become spurious flat events when a median filter is applied.

The final stack sections exhibited particular characteristics in every model. In the two-layer model, both the undecimated and decimated stack sections show the overall same image for conventional migration and unconstrained LSM, with aliasing noise better attenuated in the latter. The "smiles" in conventional migration were not fully suppressed by stacking. In the LSM these smiles were attenuated when imaging the migrated gathers. The constrained LSM stack sections show the noise to be associated with spurious flat events. Finally, in the Hess salt model the stacked sections exhibited differences mainly related to the changes in the amplitudes during LSM, in the background noise, and the presence of spurious flat events in constrained LSM. The amplitude re-distribution observed in the common reflection point gathers after unconstrained LSM, might be responsible for the partial attenuation of some multiples and background noise in the stack sections, more notably in the decimated case.

One important issue was the lack of convergence when trying to migrate the Hess salt model including the near offset traces. The computation in blocks of traces allowed me to detect the problem, which was solved excluding those traces at expense of the lack of imaging of the shallowest reflectors. This could constitute a problem with numerical compatibilities between the Kirchhoff algorithm and the finite differences algorithm used to generate the data.

APPENDIX E: Software overview

The software that I wrote for the three-dimensional examples of CLSM is conformed of seven Fortran95/2003 main programs (three of them, dip3d, sof4d and stack previously developed by AASPI members) and three auxiliary programs working in a bash script. The first part of such scripts receives the information of the input parameters through a C++ GUI. The second part contains the migrations options, including the loop over the iterations for the conjugate gradient method, which is conditioned by the choice of conventional migration vs. least-squares migration.

Figures E1 to E5 show the fields that correspond to the input parameters in the GUI's panels in the lower part of the GUI.

The upper part of the GUI (Figures E1 to E5) allows the specification of the input data files and the output options. The first and second fields are mandatory, and correspond to the common-shot gathers and the RMS velocity field. The third and fourth fields are optional, and allow the input of the Thomson anisotropic parameters. If η (eta) is available, this is the only parameter required in the third field. Otherwise, ε (epsilon) and δ (delta) are required in the third and fourth fields respectively. The project name and the suffix define the name of the output migrated gathers.

The *Input parameters* panel (Figure E1) requires information about:

a) The minimum and the maximum temporal frequency to be migrated. The corresponding filter is implemented during the application of the time derivative and its adjoint in the migration and demigration programs, respectively.

b) The offset parameters: the bin size (offset increment) as well as the minimum and the maximum offsets.

c) The minimum fold. Areas with folds smaller than this value will not be migrated.

d) Migration aperture. The value is provided in degrees corresponds to the maximum values of structural dip expected in the area, and allows the calculation of the aperture according to the method described by Murty and Shankar (2006), which calculates the aperture value according to depth.

e) Mute slope, in slowness units (s/m or s/ft), to reject the stretch zone.

The *Velocity/migration* panel (Figure E2) requires information about:

a) Velocity parameters. The smoothing parameters are provided only if the velocity field has not been previously smoothed. The velocity fraction allows the scaling of the velocity field, and can be employed to make tests with different velocity percentages.

b) Migration parameters. The number of blocks breaks the problem down to sizes that can fit units of available RAM, without significant change in running time. The time interpolation factor interpolates the time samples of the data traces in the factor specified, to more accurately locate the time position in the trace corresponding to the calculated traveltime during migration. It is commonly set to 4.

The *Output parameters* panel (Figure E3) requires information about:

a) The preconditioning function parameters (Equations A.19-A.22). These parameters set the initial time of the weight function, the slope of the mute applied to the data arrays (not to be confused with the mute applied to the migrated gathers), the length of the tapering region of the mute, and a gain factor to compensate for spreading losses in the data.

b) The desired dimensions of the output volume.

The *CSLM parameters* panel (Figure E4) requires information about:

a) Least-squares migration options. Setting *On* the *Use LSQM?* button enables all the options. One has to specify the number of iterations.

b) Constraint function parameters. If previous option is *On*, one can choose to apply the constraint function setting the *Use const funct?* button *On*. This enables the parameters for the dip3d and the sof4d programs. One can choose between the application of the mean, median or principal component filter.

Finally, the *Extended* panel (Figure E5) allows to set the MPI parameters. Internally, the migration and demigration programs always utilize OpenMP whether the MPI box is selected or not.

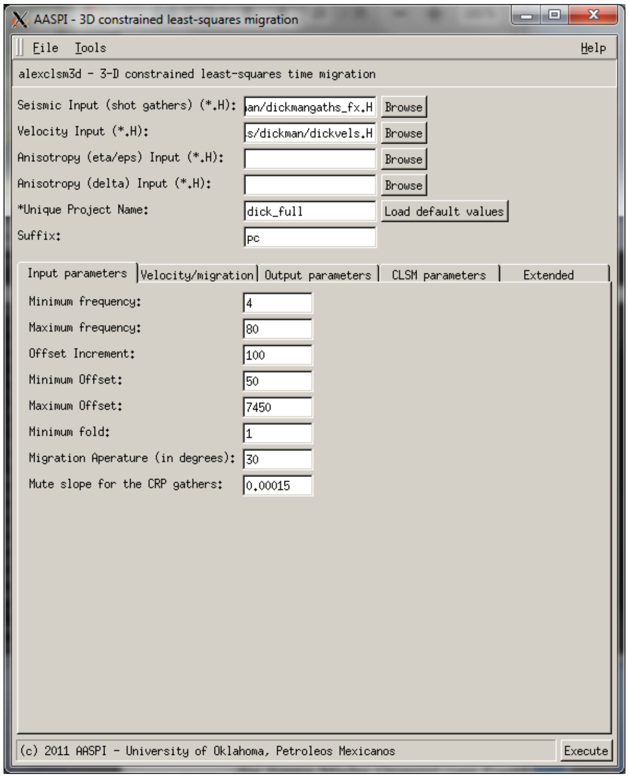

alexclsm3d - 3-D constrained least-squares time migration

Seismic Input (shot gathers) (*.H): an/dickmangaths_fx.H
Velocity Input (*.H): s/dickman/dickvels.H
Anisotropy (eta/eps) Input (*.H):
Anisotropy (delta) Input (*.H):
*Unique Project Name: dick_full
Suffix: pc

Minimum frequency: 4
Maximum frequency: 80
Offset Increment: 100
Minimum Offset: 50
Maximum Offset: 7450
Minimum fold: 1
Migration Aperature (in degrees): 30
Mute slope for the CRP gathers: 0.00015

(c) 2011 AASPI - University of Oklahoma, Petroleos Mexicanos

Figure E1. CLSM GUI: First panel.

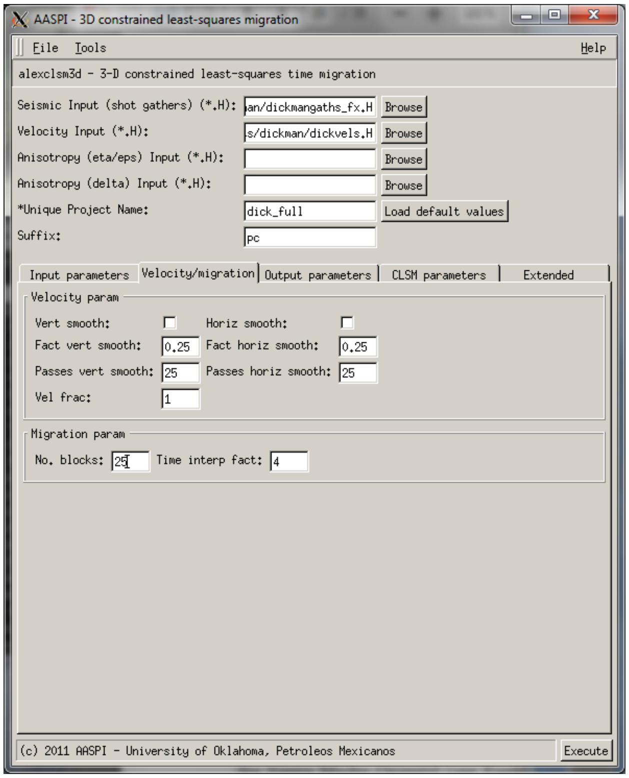

alexclsm3d - 3-D constrained least-squares time migration

Seismic Input (shot gathers) (*.H): an/dickmangaths_fx.H
Velocity Input (*.H): s/dickman/dickvels.H
Anisotropy (eta/eps) Input (*.H):
Anisotropy (delta) Input (*.H):
*Unique Project Name: dick_full
Suffix: pc

Vert smooth: ☐ Horiz smooth: ☐
Fact vert smooth: 0.25 Fact horiz smooth: 0.25
Passes vert smooth: 25 Passes horiz smooth: 25
Vel frac: 1

No. blocks: 25 Time interp fact: 4

(c) 2011 AASPI - University of Oklahoma, Petroleos Mexicanos

Figure E2. CLSM GUI: Second panel.

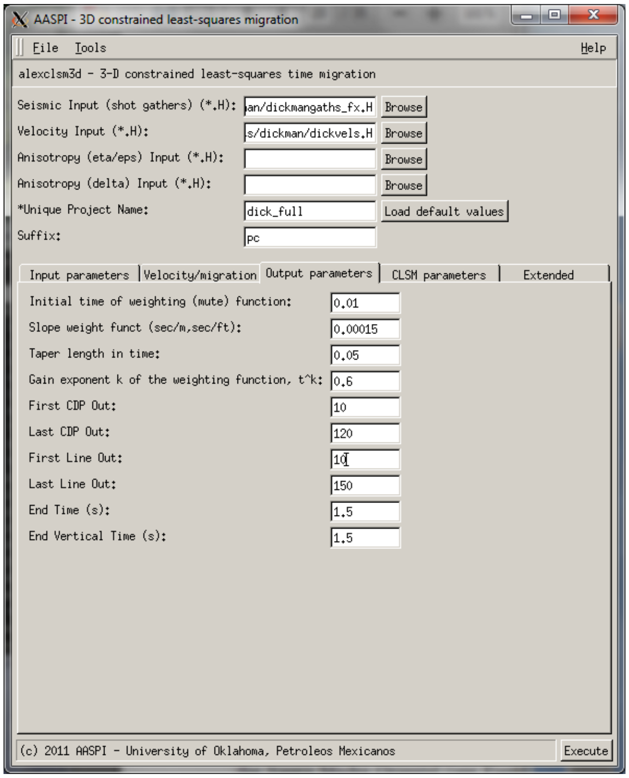

alexclsm3d - 3-D constrained least-squares time migration

Seismic Input (shot gathers) (*.H): an/dickmangaths_fx.H
Velocity Input (*.H): s/dickman/dickvels.H
Anisotropy (eta/eps) Input (*.H):
Anisotropy (delta) Input (*.H):
*Unique Project Name: dick_full
Suffix: pc

Initial time of weighting (mute) function: 0.01
Slope weight funct (sec/m,sec/ft): 0.00015
Taper length in time: 0.05
Gain exponent k of the weighting function, t^k: 0.6
First CDP Out: 10
Last CDP Out: 120
First Line Out: 10
Last Line Out: 150
End Time (s): 1.5
End Vertical Time (s): 1.5

(c) 2011 AASPI - University of Oklahoma, Petroleos Mexicanos

Figure E3. CLSM GUI: Third panel.

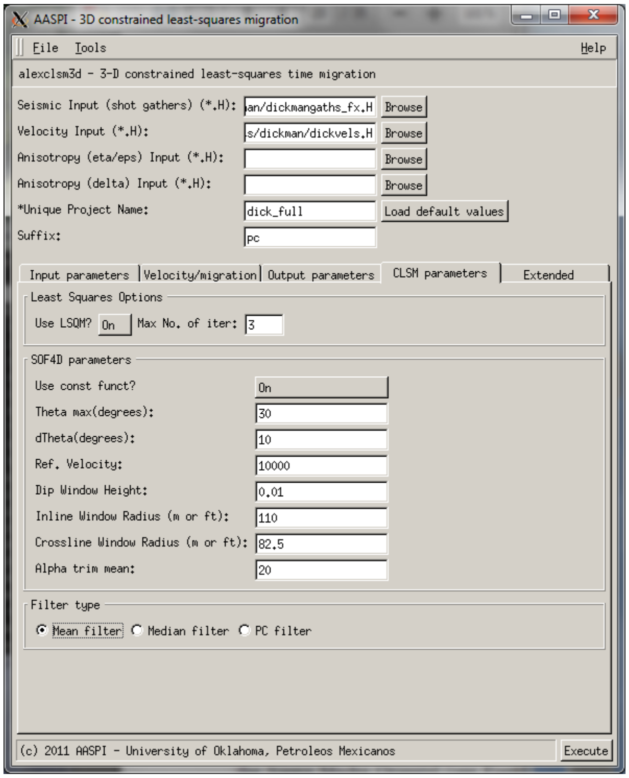

alexclsm3d - 3-D constrained least-squares time migration

Seismic Input (shot gathers) (*.H): an/dickmangaths_fx.H
Velocity Input (*.H): s/dickman/dickvels.H
Anisotropy (eta/eps) Input (*.H):
Anisotropy (delta) Input (*.H):
*Unique Project Name: dick_full
Suffix: pc

Least Squares Options
Use LSQM? On
Max No. of iter: 3

SOF4D parameters
Use const funct? On
Theta max(degrees): 30
dTheta(degrees): 10
Ref. Velocity: 10000
Dip Window Height: 0.01
Inline Window Radius (m or ft): 110
Crossline Window Radius (m or ft): 82.5
Alpha trim mean: 20

Filter type
● Mean filter ○ Median filter ○ PC filter

(c) 2011 AASPI - University of Oklahoma, Petroleos Mexicanos

Figure E4. CLSM GUI: Fourth panel.

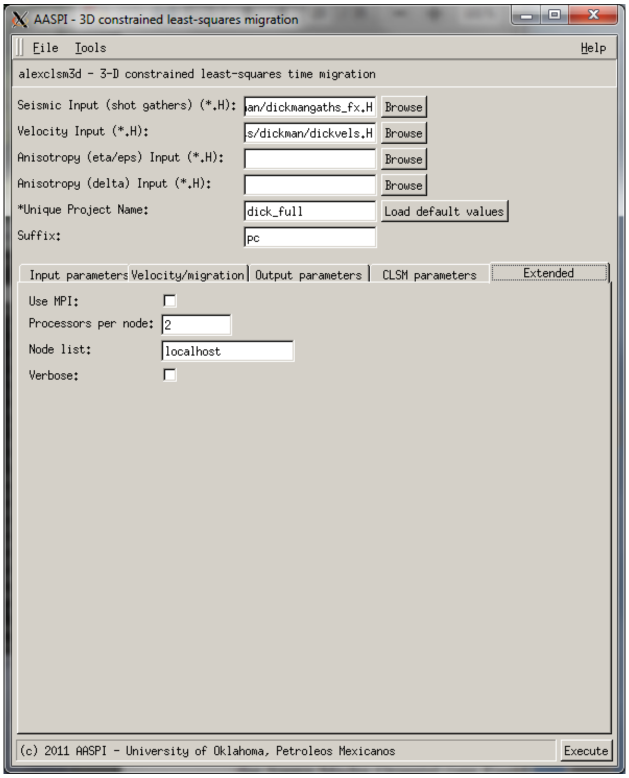

alexclsm3d - 3-D constrained least-squares time migration

Seismic Input (shot gathers) (*.H): an/dickmangaths_fx.H

Velocity Input (*.H): s/dickman/dickvels.H

Anisotropy (eta/eps) Input (*.H):

Anisotropy (delta) Input (*.H):

*Unique Project Name: dick_full

Suffix: pc

Use MPI: ☐

Processors per node: 2

Node list: localhost

Verbose: ☐

(c) 2011 AASPI - University of Oklahoma, Petroleos Mexicanos

Figure E5. CLSM GUI: Fifth panel.

REFERENCES

Alkalifah, T., 1997, An anisotropic Marmousi model: Stanford Exploration Project, **95**, 265-283.

Aoki, N., and G. Schuster, 2009, Fast least-squares migration with a deblurring filter: Geophysics, **74**, WCA83-WCA93.

Bleistein, N., J. Cohen, and J. Stockwell, 2001, Mathematics of multidimensional seismic imaging, migration and inversion: Springer.

Biondi, B., 2006, 3D seismic imaging: Society of Exploration Geophysicists.

Claerbout, J., 2009, Basic earth imaging (version 3.2): Available in the URL: http://sepwww.stanford.edu/sep/prof.

Chopra, S., and K. Marfurt, 2007, Seismic attributes for prospect identification and reservoir characterization: SEG/EAGE Geophysical Developments, **11**.

Chemingui, N., and Biondi, B., 2002, Seismic data reconstruction by inversion to common offset: Geophysics, **67**, 1575-1585.

Davogustto-Cataldo, O., 2011, Removing footprint from legacy seismic data volumes: M.Sc. Thesis, University of Oklahoma.

Duquet, B., K. Marfurt, and J. Dellinger, 2000, Kirchhoff modeling, inversion for reflectivity, and subsurface illumination: Geophysics, **65**, 1195-1209.

Fomel, S., J. Berryman, R. Clapp, and M. Prucha, 2002, Iterative resolution estimation in least-squares Kirchhoff migration: Geophysical Prospecting, **50**, 577-588.

Hestenes, M., 1973, Iterative methods for solving linear equations: Journal of Optimization Theory and Applications, **11**, 323-334.

Hu, J., G. Schuster, and P. Valasek, 2001, Poststack migration deconvolution: Geophysics, **66**, 939-953.

Jäger, C., 2001, Kirchhoff migration and demigration - Theory, implementation and application: Ph. D. diss., Universität Karlsruhe.

Jovanovic, K., 2004, P and SV polarization filtering of a multicomponent vector VSP: M.S. thesis, Univ. of Houston.

Kühl, H., and M. Sacchi, 2001, Least-squares wave-equation migration: CSEG Recorder, **26**, 41-48.

------, 2003, Least-squares wave-equation migration for AVP/AVA inversion: Geophysics, **68**, 262-273.

Landa, E., A. Klokov, and R. Baina, 2011, Point and edge diffractions in three dimensions: 73rd EAGE Conference and Exhibition, Vienna, Austria, May 2011.

Moser, T., 2011, Edge and tip diffraction imaging in three dimensions: 73rd EAGE Conference and Exhibition, Vienna, Austria, May 2011.

Murty, J., and T. Shankar, 2006, Prestack migration aperture - An overview: Geohorizons, July 2006, 8-13.

Nemeth, T., 1996, Imaging and filtering by least-squares migration: Ph. D. diss., Univ. of Utah.

Nemeth, T., C. Wu, and G. Schuster, 1999, Least-squares migration of incomplete reflection data: Geophysics, **64**, 208-221.

Nissen, S., T. Carr, K. Marfurt, and E. Sullivan, 2009, Using 3-D seismic volumetric curvature attributes to identify fracture trends in a depleted Mississippian carbonate reservoir: Implications for assessing candidates for CO_2 sequestration: AAPG Studies in Geology, **59**, 297-319.

Pérez, G., 1997, The quality of the surface-consistence assumption in residual statics estimation: M.Sc. Thesis, Colorado School of Mines.

Ren, H., R. Wu, and H. Wang, 2011, Wave equation least square imaging using a local angular Hessian for amplitude correction: Geophysical Prospecting, **59**, 651-661.

Ronen, S., and C. Liner, 2000, Least-squares DMO and migration: Geophysics, **65**, 1364-1371.

Schuster, G., 1997, Acquisition footprint removal by least squares migration: **1997** Annual UTAM Report, 73-99.

Tarantola, A., 2005, Inverse problem theory and methods for model parameter estimation: Society of Industrial and Applied Mathematics.

Wang, J., H. Kuehl, and M. Sacchi, 2005, High-resolution wave-equation AVA imaging: Algorithm and tests with a data set from the Western Canadian Sedimentary Basin: Geophysics, **70**, s91-s99.

Wang, J., and M. Sacchi, 2009, Structure constrained least-squares migration: SEG 2009 International Exposition and Annual Meeting.

Yu, J., G. Schuster, J. Hu, and B. Estill, 2006, 3-D prestack migration deconvolution: Geophysics, **71**, S53-S62.

Zhang, Y., M. Karazincir, C. Notfors, J. Sun, and B. Hung, 2002, Amplitude preserving v(z) prestack Kirchhoff migration, demigration and modeling: 64th EAGE Annual Conference, 27-30.